Doctoral Thesis reviewed

by Ritsumeikan University

Statistical Analysis of Shape and Texture in 3D Medical Images for Computer-Aided Diagnosis

３次元医用画像における形状とテキスチャの統計解析及び計算機支援診断への応用

March, 2015

2015 年 3 月

Doctoral Program In Integrated Science and Engineering
Graduate School of Science and Engineering
Ritsumeikan University

立命館大学大学院理工学研究科

総合理工学専攻博士課程後期課程

DENG JUNPING

デン　ジュンピン

Supervisor: Professor Yen-Wei Chen

指導教員：陳 延偉 教授

ABSTRACT

In recent years, medical imaging, including computed tomography (CT), magnetic resonance imaging (MRI), and ultrasound imaging, has made remarkable progress. It is possible to use high-resolution 3D medical images for diagnosis. Computer-aided diagnosis (CAD) has become one of the major research subjects in the field of medical image analysis. The basic idea of CAD is to extract useful features (such as shape and texture) from medical images and then use machine learning methods to generate an independent diagnosis. One of the key issues in CAD is how to extract (represent) the shape and texture features for machine learning. In conventional CAD, principal component analysis (PCA) is usually used to represent the features using statistical shape and appearance models. However, PCA is a global analysis method, and it does not always determine local changes. Furthermore, PCA requires that the 3D image be first unfolded into a 1D vector prior to analysis. The spatial structure will be lost, and this increases the computational cost. In this study, I propose a novel method for the statistical analysis of shape and texture in computer-aided diagnosis. The main contributions of this thesis are as follows:

1. An efficient method for the statistical analysis of texture, called linear tensor coding, is proposed; it is based on multilinear algebra for 3D medical volumes. In our previous work, in order to compactly represent medical volumes, we proposed a generalized N-dimensional principal component analysis (GND-PCA), which was based on multilinear algebra and directly modeled multidimensional medical

volumes (tensors). It enabled the statistical texture model to construct medical volumes based only on a few samples, and its performance for medical volume representation was much better than that of conventional PCA. However, the extracted GND-PCA models were highly correlated, and thus it was redundant to use the core tensor as a feature to represent the medical volume. In addition, it is difficult to choose the basis for discriminating between classifications when applying this to CAD. To solve these problems, a linear tensor coding (LTC) algorithm was proposed for direct modeling of 3D medical volumes. Compared to GND-PCA, LTC is able to achieve a more compact and meaningful tensor basis. With LTC, medical volumes can be represented by a linear combination of basis tensors that are mutually independent and feasible for specific classification applications. The proposed method was evaluated using a liver database and considering two aspects: medical image reconstruction and diagnosis. Compared to GND-PCA, when using the same basis, LTC obtains better results, and when choosing a distinctive basis, LTC obtains a much better diagnosis.

2. A robust point-based registration method is proposed. This method preprocesses with the local analysis of shape in order to remove any local deformations or noise. Generalized Procrustes analysis (GPA) is a fairly straightforward approach to point-based registration. The algorithm's low complexity allows for easy implementation. However, the final registration performance is affected by noise or local deformation. However, it is well known that within a given category, the shape information shares a similar global structure; thus, the ensemble should be of low rank. However, noise or local deformations may lead to changes in only a small region, which may be relatively sparse compared with the total shape information. Therefore, in this study, I first applied sparse and low-rank matrix decomposition (SLRMD) to separate the input shape information $\mathbf{D}$ into the noise or local deformation part (sparse matrix $\mathbf{E}$) and the global structure (low-rank matrix $\mathbf{A}$). Then the low-rank matrix $\mathbf{A}$ (without noise or local deformation) was issued for GPA-based registration. The registration

performance of the proposed strategy was evaluated using liver volumes. Experimental results showed that the proposed strategy could achieve promising registration performances, compared with the conventional GPA method.

3. Finally, an accurate CAD for cirrhotic livers was developed based on the local analysis of shape. Our method is based on SLRMD, since the matrix of the liver shapes can be decomposed into two parts: a low-rank matrix, which can be considered similar to that of a normal liver, and a sparse error term, which represents the local deformation. We also propose to use the norm of the sparse error term as a simple measure for classification into normal or abnormal. Compared with the previous global morphological analysis strategy based on the statistical shape model (SSM), our proposed method improves the accuracy of both normal and abnormal classifications. Note that the conventional SLRMD is a batch method. If additional data are obtained, the calculation must be repeated using all of the data. This is time-consuming because of the large dimensionality of the matrices. Thus, I also propose an incremental SLRMD based on incremental singular value decomposition (ISVD) for on-line medical image diagnosis. The objective of the incremental SLRMD is to recover the results that were calculated by conventional SLRMD (with an alternating greedy algorithm for L0-norm regularization). Note that the computation time of the incremental SLRMD is less than that of the conventional SLRMD. The methods of diagnosis based on SLRMD and incremental SLRMD were evaluated using a cirrhosis database with 30 each of normal and abnormal data points. The diagnosis results were better than those of the state-of-the-art SSM-based methods, and the incremental SLRMD achieved the objective.

Contents

List of Figures

List of Tables

Chapter 1

Introduction

In recent years, medical imaging, including computed tomography (CT), magnetic resonance imaging (MRI), and ultrasound imaging, has made remarkable progress. It is possible to use high-resolution 3D medical images for diagnosis. Computer-aided diagnosis (CAD) [1-4] has become one of the major research subjects in the field of medical image analysis. The basic idea of CAD is to first extract useful features (shape and texture) from medical images, and then use machine learning methods to generate an independent opinion that can be used to assist in making the final diagnosis. Efficiently and compactly representing the shape and texture features, which is also key to the performance of the CAD system, is a great challenge due to the multiple dimensions of medical images. CAD can be generalized as consisting of the several procedures that are shown in Figure 1.1: image input (different image types), image segmentation, image registration, feature extraction and representation, and classification/diagnosis. In the following subsections, I will briefly introduce each of these procedures.

1.1 General Computer-Aided Diagnosis System

1.1.1 Medical Image

In modern medicine, medical imaging has undergone major advancements, and it now has many useful clinical applications. Over the years, different sorts of medical imaging have been developed, each with their own advantages and disadvantages.

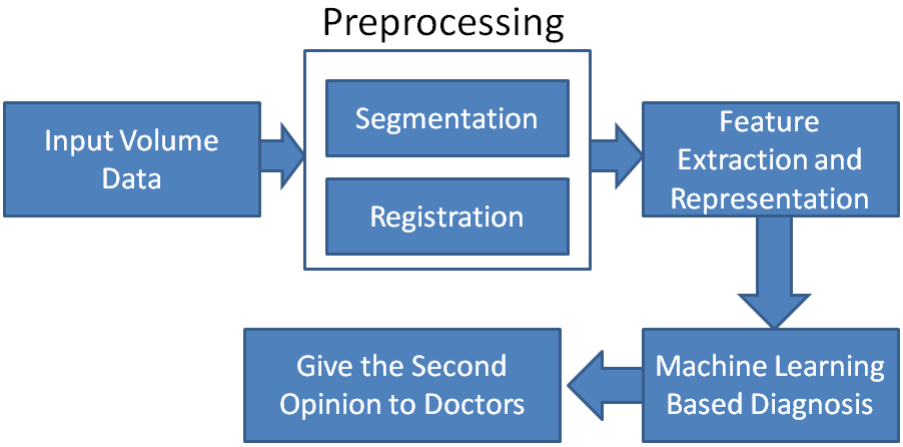

Figure 1.1: The flowchart of CAD system.

Radiography (X-ray imaging) was accidentally discovered by Roentgen in 1895 and was the first kind of medical imaging technique. Solid tissues, such as bone, can be shown easily in a radiograph, because X-rays can pass more easily through materials with low density than through those with high density. Radiographs only produce two-dimensional (2D) images, and thus they cannot give the detailed 3D anatomical structure of a human body. Each point contains the information integrated along the path of an X-ray, so radiographs show the characteristics of transparency.

Computer tomography (CT) is another kind of medical imaging technique, and it uses X-rays to produce tomographic images (virtual "slices ") of specific areas of the scanned object. Digital geometry processing is used to generate a 3D image of the inside of an object from a large series of 2D radiographic images taken around a single axis of rotation. CT reflects the anatomy of the human body. Like radiography, in CT, the bones produce high intensities, and the soft tissues produce low intensities. In this thesis, I mainly used CT images stored in the digital imaging and communications in medicine (DICOM) image format. This file format was created as a way to distribute and view medical images using a standardized file format.

Magnetic resonance imaging (MRI), or nuclear magnetic resonance (NMR) imaging [5], is another

primary diagnostic tool for generating structural images of the human body. NMR is the fundamental theoretical basis of MRI; it is a physical phenomenon of the nucleus of an atom. MRI is similar to CT in that it is a method for collecting 2D images (slices) in order to generate a 3D view; that is, MRI can be regarded as a tomographic imaging technique. Although CT and MRI are sensitive to different properties in tissues, MRI can provide high-quality images with excellent contrast detail of soft tissue and anatomic structures such as the gray and white matter in the brain. The most common kinds are T1-weighted, T2-weighted, and proton density¨Cweighted (PD-weighted) MRIs. As an area of future work, I will investigate the processing of MRI images.

Positron emission tomography (PET) employs the main features of the tracer techniques that were developed to study the underlying mechanisms of physiological and biochemical processes in living organisms [6]. In these methods, radioactively labeled substances are injected intravenously and can be traced through the body using external detectors. In the case of PET, the tracer is labeled with an isotope that emits a positron. Such isotopes are available for a number of biologically relevant atoms, namely oxygen, carbon, nitrogen, and fluorine. Labeling with a radioactive nuclide allows the synthesis of specific tracers, which are used to determine, for example, cerebral blood flow or glucose consumption in the human brain. Hence, PET is representative of a functional image modality, and the primary issue in the development of PET was to quantify the 3D distribution of the radioactive tracer with subsequent interpretation in the framework of a physiological model. PET images are of lower quality than CT and MR images.

There are also many other kinds of medical image types, such as ultrasound imaging [7], single photon emission computed tomography (SPECT) [8], and so on. In here, I will not introduce them anymore.

1.1.2 Preprocessing

1.1.2.1 Medical Image Segmentation

In image segmentation, an image is divided into its constituent parts or objects, such as a set of pixels that are similar according to some homogeneity criteria such as color, intensity, or texture [9]. Many researchers have reviewed segmentation methods and classified them in different ways [10][11]. To summarize this, the most common methods of medical image segmentation include graph cuts, region growing, clustering, and geometric active contours. In the first three of these, the segmentation is based on intensity; in the last one, it is based on shape.

Graph cuts [12] is an interactive segmentation technique and has been applied to organ segmentation from medical CT volumes [13]. The basic idea is to use graph cuts to separate the object of interest from the background. Here, the segmentation problem is formulated on a discrete graph. The graph $\mathbf{G} = \{\mathbf{V}, \mathbf{E}\}$ is composed of vertices V that represent the image pixels, as well as edges E that connect the vertices. There are two special vertices: an "object terminal" (source) and a "background terminal" (sink). The source is connected by edges to all of the vertices identified as object seeds, and the sink is connected to all of the background seeds.

In the region-growing [14][15] approach to segmentation, neighboring pixels are examined and if no edges are detected, they are added to the current region class. The simplest illustration of this approach is pixel aggregation, which starts with a set of seed points and grows regions from these seeds. This approach is repeated for each boundary pixel in the region. If adjacent regions are found, a region-merging algorithm is implemented to dissolve weak edges; strong edges are left intact.

Clustering (unsupervised methods) can be defined as the process of organizing objects into groups whose members are similar in some ways. Clustering involves a search within a given image for frequently occurring pixel values that are separated by areas of pixel values that occur less frequently.

These pixel clusters form natural classes that show up as peaks in the histogram. These peaks are then separated by minima. There are three commonly used clustering algorithms: the k-means algorithm [16], the fuzzy c-means algorithm [17], and the expectation-maximization algorithm [18].

The geometric active contours approach employs ideas from Euclidean curve shortening, which defines the gradient in which the Euclidean perimeter is shrinking the most quickly. New active contour models may be derived by multiplying the Euclidean arc length by a conformal factor tailored to the features that one wants to capture, and then writing down the resulting gradient evolution equations. The latter becomes a curve-shortening equation with respect to the new conformally Euclidean metric. These models may be implemented using level sets. They have been called geodesic snakes [19] and conformal active contours [20]. Statistical models combining both local and global features have been formulated by Lankton et al. [21].

1.1.2.2 Medical Image Registration

Medical image registration is a process for finding a spatial transformation that aligns the corresponding features in two medical images. Consider a scenario in which a patient is imaged with MRI and CT over the course of a few hours as a workup for neurosurgery. The registration process will establish which point on one image corresponds to a particular point on the other. By "correspond," we mean that these points represent a measurement localized to the same small element of tissue. The computational process of registration creates an appropriate transformation between the coordinate systems of the two medical images.

There are different ways to classify medical image registration methods. In this thesis, they will be divided into rigid or nonrigid registrations, based on the underlying transformation that is adopted; that is, if a rigid transformation is used, it will be called a rigid registration; otherwise it will be called a nonrigid registration. In the 2D case, a rigid transformation has only three parameters: one rotation

angle and two translation vectors; a 3D rigid registration has six parameters: a rotation angle and a translation vector for each of the three axes. Rigid registration is used when the subject can be seen as a rigid object, e.g., the brain of a given patient. A nonrigid transformation has more degrees of freedom. An affine transformation results in a simple nonrigid registration. In the 3D case, it has twelve parameters to describe the transformation, rotation, scaling, and shearing on each pixel. Other more-complex nonrigid transformations include, for example, the thin-plate spline transformation [22], the B-spline transformation [23], the elastic transformation [24], and the fluid transformation [25]. Nonrigid registration is used when the subjects of the medical images have deformations, for example, when imaging abdominal organs or anatomic changes due to long-term processes.

Medical image registration can be formalized as an optimization problem of finding the parameters of a spatial transformation on two medical images that maximizes or minimizes a certain cost function. There are different ways to calculate the cost function, and so medical image registration methods can be divided into three categories: point-based, surface-based, and voxel-similarity-based registration [26].

Point-Based Registration Method

We denote a spatial transformation as $\mathbf{T}(\mathbf{x}\,|\mathbf{u})$, where is the coordinate of a point and $\mathbf{u}$ is the parameter of the transformation. A point-based method determines the parameters of the transformation from two sets of points, $\mathbf{X} = \{\mathbf{x}_1, \mathbf{x}_2, \ldots, \mathbf{x}_N\}$ and $\mathbf{Y} = \{\mathbf{y}_1, \mathbf{y}_2, \ldots, \mathbf{y}_N\}$; prior to registration, the corresponding points may be determined manually or automatically. These corresponding points can be classified into two categories. The first is called homologous landmarks to emphasize that they should both represent the same feature; these can be anatomical features or marks attached to the patients. The second uses the boundaries or surfaces of tissues or organs, which are usually more distinct than landmarks in medical images, since different types of tissues usually have contrasting

intensities in various imaging modalities. The parameter $\mathbf{u}$ can be calculated by resolving the Procrustes problem, which is an optimal least-squares fitting problem that minimizes the cost function of $G(\mathbf{u}) = \sum_{i=1}^{N} \|\mathbf{T}(\mathbf{x}_i\,|\mathbf{u}) - \mathbf{y}_i\|$. A matrix representation of the rotational part can be computed using the singular value decomposition (SVD) [27]. This approach is used not only for medical image registration [28], but also for construction of statistical shape models [27]. Another surface-based registration method is the iterative closest point (ICP) algorithm. It was proposed by Cuchet et al. [29], and it was not initially designed for medical imaging applications. ICP is an iterative method for determining the transformation between two sets of points. In each iteration, the transformation calculated in the previous iteration is used to determine the closest corresponding point, and then the transformation is refined by resolving the Procrustes problem. The process terminates when the change in the mean square error between the two point sets in two consecutive steps is below a predetermined threshold. It is probable that ICP is the most widely used surface-based registration method for medical imaging applications [30][31].

Voxel-Similarity Based Registration Methods

Voxel-similarity-based registration methods determine the appropriate transformation by directly considering the relations between the voxels (pixels) in the medical image; thus, no preprocessing is required. Since these methods allow the registration to be performed automatically, they have been popular in recent years.

Voxel-similarity-based registration methods can be viewed as an iterated optimization framework; this is shown in Figure 1.2. The image that is not changed during the registration process is called the "fixed image"; the other is called the "moving image." In each iteration, the transformation with the current parameters is applied to the moving image. Then, following interpolation, a cost function is used to evaluate the voxel similarity of the fixed image and the transformed moving image, and to

determine whether the two images are registered under the current transformation. If the images are not registered, an optimization method is used to adjust the parameters and iteration continues.

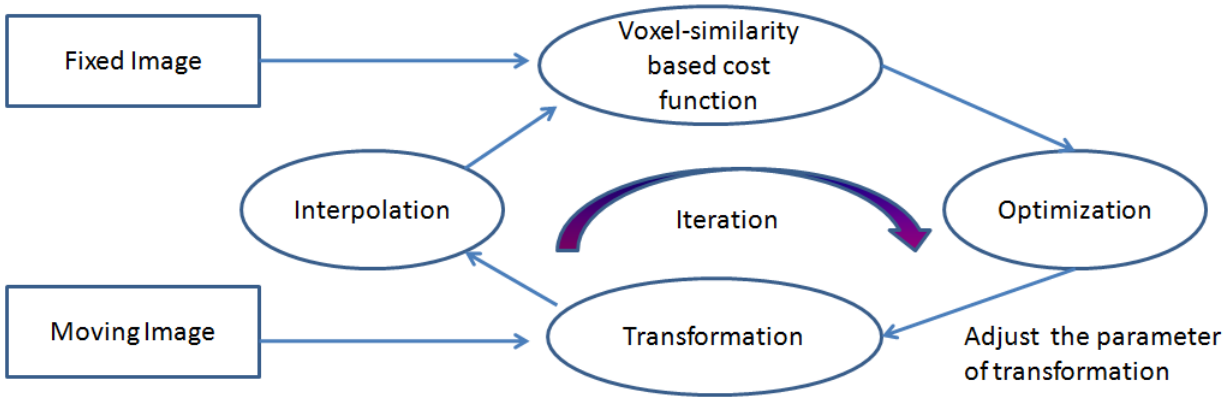

Figure 1.2: Optimization framework for voxel-similarity based registration.

1.1.3 Feature Extraction and Representation

Feature extraction and representation is a crucial step in the analysis of medical images. It is still a challenge to determine how to extract robust and compact features that reflect the intrinsic content of the images as completely as possible. These features can be divided into two categories: texture and shape.

Texture is a very useful characterization. It is generally believed that human visual systems greatly rely on textural information for recognition and interpretation. A large number of techniques have been proposed to extract texture features. Based on the domains from which they are extracted, feature extraction methods can be broadly classified as either spatial texture or spectral texture methods. In spatial texture methods, features are extracted by computing the pixel statistics or by finding the local pixel structures in the original image domain, whereas in spectral texture methods, the image is first transformed into the frequency domain, prior to calculating the features. Local binary patterns (LBP) [32][33] and the gray-level co-occurrence matrix (GLCM) [34][35] can be used for the extraction of spatial texture features from any shape without loss of information; they are, however, sensitive

to noise and distortions. Wavelets [36] and the Gabor filter [37] have been widely used to extract texture features, and these characterize the central frequency and orientation parameters of the image and then sample its entire frequency domain. In the analysis of medical images, including in this thesis, "texture" is used to refer to the intensity of the image. In this way, the medical image will not be processed by any algorithms. Most of the above methods have the same problem: the features have high dimensionality and contain much redundant information. Thus, it is important to find an efficient way to represent the features. Principal component analysis (PCA) is one of the most popular methods for representing features [38][39], and a detailed introduction to PCA will be given in Chapter 2.

Shape is known to be an important cue by which human beings identify and recognize objects. Thus, a set of surface points are often used for shape representation in medical image analysis. With a greater number of surface points, more details will be preserved, but the dimensionality of the feature will increase. Thus, the method used to represent the shape is important. The spherical harmonic (SPHARM) description is a powerful surface-modeling technique that can model arbitrarily shaped but simply connected 3D objects; it has been used in many applications of medical imaging [40][41]. Alternatively, the shape can be represented by a statistical shape model (SSM) [42], which is based on PCA. The SSM is statistically learned from a population of objects or organs, and it is an object- (or organ-) specified shape model. The shape is constrained in its eigen-subspace. Some studies have considered the construction of SSMs of anatomical organs, such as the brain [43] or heart [44]. In our previous work, we constructed an SSM of the liver and showed that the coefficients of the model could be used to classify livers as cirrhotic or normal [45].

1.1.4 Machine learning based diagnosis

Machine learning-based diagnoses can be considered to be a classification problem. A medical image can be classified as normal or abnormal based on its texture and shape features. In this thesis, I use three methods to classify the image: nearest-neighbor classification, support vector machines (SVM), and the adaptive boosting algorithm known as AdaBoost. These classification methods are introduced below.

Nearest-neighbor classification is a very simple method that is based on the nearest-neighbor approach [46]. This method searches the N-dimensional feature space for the object in the training set that is closest to the object being classified. Since the neighbor is nearby, it is likely to be similar to the object being classified, and so it is likely to be in the same class. Nearest-neighbor methods have the advantage of being easy to implement. They can also give quite good results if the features are chosen carefully. However, they also have some serious disadvantages. For example, they do not simplify the distribution of objects in the parameter space to a comprehensible set of parameters. Instead, the training set is retained in its entirety as a description of the object. The method is also rather slow if the training set has many examples.

An SVM [47] is a binary classifier that distinguishes between two classes of instances by finding the maximum separating hyperplane between them. For this reason, SVMs tend to generalize better than do nearest-neighbor methods. However, in their simple form as linear classifiers, SVMs can only discriminate between two classes. In order to allow for the classification of more than two classes, one of the following methods can be employed. It is possible to create a nonlinear SVM by increasing the dimensionality of the feature space and by using the so-called "kernel-trick." It is thus possible to find a separating hyperplane in a higher-dimensional space, even if such a hyperplane would not exist in a lower-dimensional space. Figure 1.3 illustrates a SVM based on two classes. The samples on the

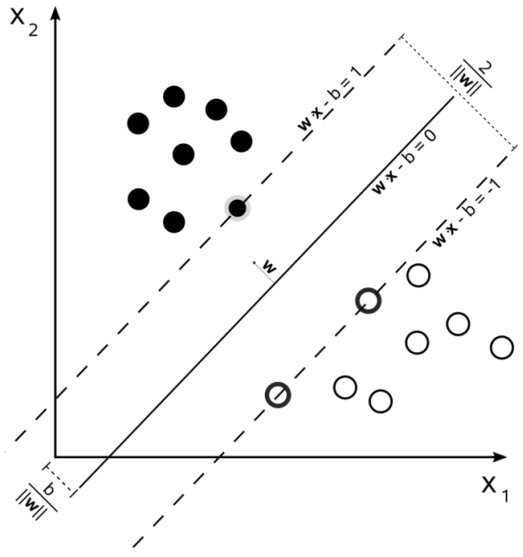

Figure 1.3: Maximum-margin hyperplane and margins for an SVM trained with samples from two classes. Samples on the margin are called the support vectors [53].

margin are called the "support vectors" [48].

The AdaBoost classifier, initially proposed by Freund et al. [49], is an ensemble classifier composed of many weak classifiers (such as linear classifiers), each of which discriminates only according to one dimension of the input vector. The result of the ensemble classifier can be expressed as:

$$F(\mathbf{x}) = sign\left\{\sum_{i=1}^{T} \alpha_i h_i(\mathbf{x})\right\} \tag{1.1}$$

where $\mathbf{x}$ represents input vector; $h_t(\mathbf{x})$, $t = 1, \ldots, T$ means that the number of classifiers is T; α_t, $t = 1, \ldots, T$ refers to weight of each weak classifier. Figure 1.4 shows Adaboost algorithm.

1.2 Scope and Contributions of the dissertation

In recent years, medical imaging, including CT, MRI, and ultrasound imaging, has made remarkable progress. It is now possible to use high-resolution 3D medical images for making diagnoses. CAD has become a major research area in the field of medical image analysis. The basic idea of CAD is to extract useful features (shape and texture features) from medical images and then use machine learning

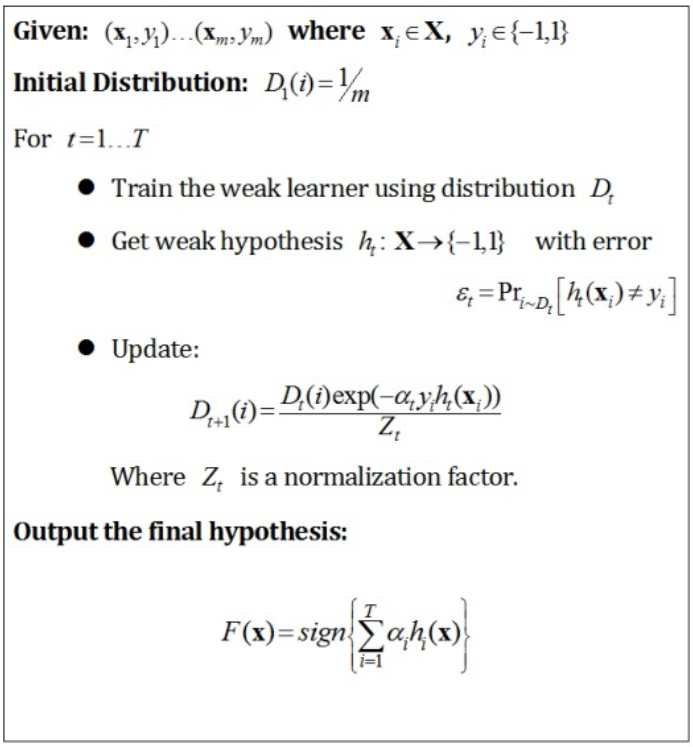

Figure 1.4: Illustration of Adaboost Algorithm.

methods to assist in the diagnosis. One of the key issues in CAD is how to extract or represent the shape and texture features for use in machine learning. In conventional CAD, PCA is usually used to obtain the shape and texture features; these are also known as statistical shape models and statistical appearance models. However, PCA is a global analysis method, and it is difficult to determine local changes. Furthermore, PCA requires that the 3D image should first be unfolded into a 1D vector. The spatial structure will thus be lost; it also suffers from high computational costs. In this study, I propose a novel statistical method for the analysis of shape and texture to be used for computer-aided diagnosis. My contributions are indicated in Figure 1.5, as follows: the green items represent my contributions, the blue items are those results previously established by others, and the purple items are those methods that I used for the corresponding applications.

To summarize, first, I propose a novel statistical method, linear tensor coding (LTC), which is based

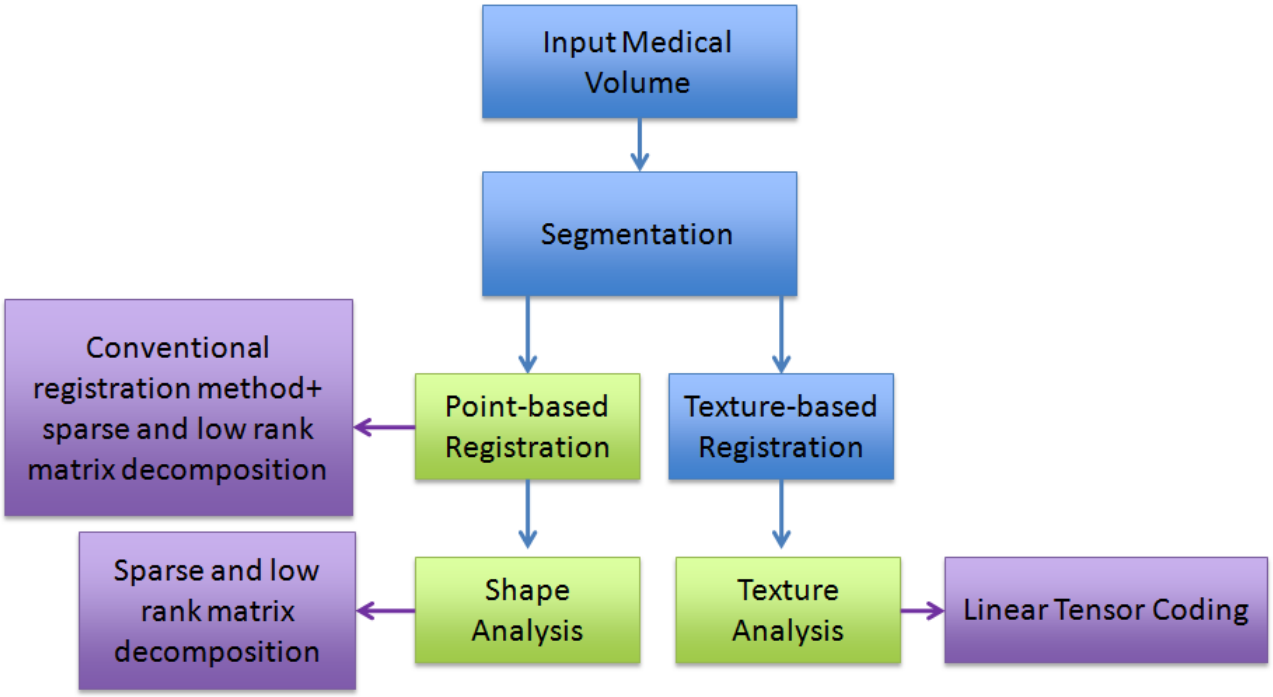

Figure 1.5: The contributions of the thesis.

on multilinear algebra and can be used for the analysis of 3D medical images; it can be considered to be an extension of conventional PCA. In the proposed method, the 3D image is treated as a third order tensor; this is done directly and without unfolding. As an improvement over the previously proposed generalized N-dimensional PCA (GND-PCA), the proposed method represents a 3D image by a linear combination of tensor-formed bases. Thus, it is possible to select the specific bases that are associated with a disease. In my experiments, I compare the LTC and GND-PCA using both reconstructed results and classification results. The LTC performed better at both reconstruction and classification than did the GND-PCA.

Second, a robust shape-based registration method is proposed. Sparse and low-rank matrix decomposition (SLRMD) was applied to separate the input shape information $\mathbf{D}$ into the noise or local deformation part (sparse matrix $\mathbf{E}$) and the global similar structure (low-rank matrix $\mathbf{A}$). The low-rank matrix $\mathbf{A}$ can be used to calculate an improved rotation matrix, which is more accurate due to a

reduction in the noise and local deformations. The improved rotation matrix is then used to improve the registration process.

Third, I proposed a quantitative method for analyzing local shape changes in order to obtain accurate and practical computer-aided diagnosis of cirrhosis. This method was also based on sparse and low-rank matrix decomposition. In this work, the matrix of the liver shapes was decomposed into two parts: a low-rank matrix, which can be considered similar to that of a normal liver, and a sparse error term that represents the local deformation. I used the norm of the sparse error term as a simple measure for classification as normal or abnormal. The experimental results of the proposed method were better than those of the state-of-the-art SSM-based methods.

Finally, I propose an incremental sparse and low-rank matrix decomposition method based on incremental SVD. This method can solve the problem of needing to recalculate in a batch method. The proposed method was derived from the alternating greedy algorithm for L0-norm regularization. The computation time using the proposed method is less than that with the batch method. As an area of future work, I will investigate the parameters used in this algorithm.

1.3 Dissertation Overview

In Chapter 2, I present a review of PCA, which contains the basic theoretical underpinnings of the proposed advanced statistical analysis strategies, and most of the approaches presented here are derived from PCA. Conventional PCA-based statistical analysis of shape and texture will also be discussed. In Chapters 3 and 4, respectively, I will introduce my work on the local statistical analysis of shape and the multilinear statistical analysis of texture.

Multilinear statistical analysis of texture based on LTC is proposed in Chapter 3. Some basic concepts of tensors (multilinear algebra) are introduced, and I briefly review the GND-PCA algorithm,

in which the extracted core information (tensor) is highly redundant and of high dimensionality. I then introduce the proposed LTC in detail; note that it can be considered to be an extension of GND-PCA. Finally, I present experimental results from GND-PCA and LTC.

In Chapter 4, I concentrate on the local statistical analysis of shape based on SLRMD, which is able to identify and separate the local shape deformations. After introducing the theory of SLRMD, I described an optimization method for solving SLRMD. In the next section, I present three applications of SLRMD: (a) a robust shape-based registration method that uses the local shape analysis as a preprocessing screen to remove local deformations and noise; (b) an accurate CAD for cirrhotic livers, which is based on the local shape analysis instead of PCA; and (c) an incremental SLRMD that can be used for on-line medical image diagnosis.

Finally in Chapter 5, I present my conclusions and discuss future avenues of research.

Bibliography

[1] G.S. Lodwick, C.L. Haun, W.E. Smith et al., Computer diagnosis of primary bone tumor, *Radiology*, 80:273-275, 1963.

[2] P.H. Meyers, C.M. Nice, H.C. Becker et al., Automated computer analysis of radiographic images, *Radiology*, 83:1029-1033, 1964.

[3] K. Doi, M.L. Giger, H. MacMahon et al., Computer-aided diagnosis: Development of automated schemes for quantitative analysis of radiographic images, *Semin Ultrasound CT MRI*, 13:140-152, 1992.

[4] K. Doi, H. MacMahon, M.L. Giger et al., Computer Aided Diagnosis in Medical Imaging. Amsterdam, *Elsevier*, 3-560, 1999.

[5] J.M. Tyszka, S.E. Fraser, R.E. Jacobs, Magnetic resonance microscopy: recent advances and applications[J],*Current opinion in biotechnology*, 16(1):93-99, 2005.

[6] M.E. Raichle, Positron-Emission Tomography, *Brain Metastasis, Springer Netherlands*, 246-253, 1980.

[7] A. Azuara-Blanco, G.L. Spaeth, S.V. Araujo et al., Ultrasound biomicroscopy in infantile glaucoma[J],*Ophthalmology*, 104(7):1116-1119, 1997.

[8] J.R.Halama, R.E.Henkin, Single photon emission computed tomography (SPECT)[M], *Freeman and Johnson's clinical radionuclide imaging*, 3, 1986.

[9] J.C. Russ, R.P. Woods, The image processing handbook[J], *Journal of Computer Assisted Tomography*, 19(6):979-981, 1995.

[10] http://www-classes.usc.edu/engr/ee-s/569/qa2/Histogram%20Equalization.htm

[11] G.K. Seerha, R. Kaur, Review on Recent Image Segmentation Techniques[J], 2013.

[12] Y. Boykov, M.P. Jolly, Interactive organ segmentation using graph cuts[C], *Medical Image Computing and Computer-Assisted Intervention¨CMICCAI 2000*, Springer Berlin Heidelberg, 276-286, 2000.

[13] L. Massoptier, S. Casciaro, Fully Automatic Liver Segmentation through Graph-Cut Technique, *Proceedings of the 29th Annual International Conference of the IEEE EMBS Cite Internationale*, 23-26, August, 2007.

[14] D.L. Pham, C. Xu, J.L. Prince, Current methods in medical image segmentation 1[J], *Annual review of biomedical engineering*, 2(1):315-337, 2000.

[15] A. Ardeshir-Goshtasby,2-D and 3-D Image Registration for Medical, Remote Sensing, and Industrial Applications, *Wiley Press*, 2005.

[16] R. Pohle, K.D. Toennies, Segmentation of medical images using adaptive region growing[C], *Medical Imaging 2001. International Society for Optics and Photonics*, 1337-1346, 2001.

[17] N. Petrick, H.P.Chan, B. Sahiner et al., Combined adaptive enhancement and region-growing segmentation of breast masses on digitized mammograms[J], *Medical Physics*, 26(8):1642-1654, 1999.

[18] H.P. Ng, S.H. Ong, K.W.C. Foong et al., Medical image segmentation using K-means clustering and improved watershed algorithm[C], *Image Analysis and Interpretation, 2006 IEEE Southwest Symposium on*, 61-65, 2006.

[19] V. Caselles, R. Kimmel, G. Sapiro, Geodesic active contours[J], *International journal of computer vision*, 22(1): 61-79, 1997.

[20] S. Kichenassamy, A. Kumar, P. Olver, et al., Conformal curvature flows: from phase transitions to active vision[J],*Archive for Rational Mechanics and Analysis*, 134(3): 275-301, 1996.

[21] S. Lankton, A. Tannenbaum, Localizing region-based active contours[J], *Image Processing, IEEE Transactions on*, 17(11): 2029-2039, 2008.

[22] F.L. Bookstein, Thin-plate splines and the atlas problem for biomedical images[C], *Information Processing in Medical Imaging*, Springer Berlin Heidelberg, 326-342, 1991.

[23] D. Rueckert, L.I. Sonoda, C. Hayes, et al., Nonrigid registration using free-form deformations: application to breast MR images[J], *Medical Imaging, IEEE Transactions on*, 18(8): 712-721, 1999.

[24] R. Bajcsy, S. Kovacic, Multiresolution elastic matching[J], *Computer vision, graphics, and image processing*, 46(1): 1-21, 1989.

[25] G.E. Christensen, R.D. Rabbitt, M.I. Miller, Deformable templates using large deformation kinematics[J],*Image Processing, IEEE Transactions on*, 5(10): 1435-1447, 1996.

[26] D.L.G. Hill, P.G. Batchelor, M. Holden, et al., Medical image registration[J], *Physics in medicine and biology* , 46(3): R1, 2001,.

[27] I.L. Dryden, K.V. Mardia, Statistical shape analysis[M], *New York: John Wiley & Sons*, 1998.

[28] A.C. Evans, C. Beil, S. Marrett, et al., Anatomical-functional correlation using an adjustable MRI-based region of interest atlas with positron emission tomography[J],*Journal of Cerebral Blood Flow & Metabolism*, 8(4): 513-530, 1988.

[29] P.J. Besl, N.D. McKay, Method for registration of 3-D shapes[C],*Robotics-DL tentative. International Society for Optics and Photonics*, 586-606, 1992.

[30] E. Cuchet, J. Knoplioch, D. Dormont, et al., Registration in neurosurgery and neuroradiotherapy applications[J], *Computer aided surgery*, 1(4): 198-207, 1995.

[31] J. Declerck, J. Feldmar, M.L. Goris, et al., Automatic registration and alignment on a template of cardiac stress and rest reoriented SPECT images[J],*Medical Imaging, IEEE Transactions on*, 16(6): 727-737, 1997.

[32] T. Ojala, M. Pietikainen, D. Harwood, A comparative study of texture measures with classification based on featured distributions[J], *Pattern recognition*, 29(1):51-59, 1996.

[33] L. Nanni, A. Lumini, S. Brahnam, Local binary patterns variants as texture descriptors for medical image analysis[J], *Artificial intelligence in medicine*, 49(2): 117-125, 2010.

[34] N. Zulpe, V. Pawar, GLCM Textural Features for Brain Tumor Classification , *IJCSI International Journal of Computer Science Issues*, 9(3):354-359, 2012.

[35] B. Ramamurthy, K.R. Chandran, Content based medical image retrieval with texture content using gray level co-occurrence matrix and k-means clustering algorithms, *Journal of Computer Science*, 8: 1070-1076, 2012.

[36] K. Gopi, D.T.R. Shri, Medical Image Compression Using Wavelets[J], *IOSR Journal of VLSI and Signal Processing (IOSR-JVSP)*, 2(4): 01-06, 2013.

[37] T. Glatard, J. Montagnat, I.E. Magnin, Texture based medical image indexing and retrieval: application to cardiac imaging[C], *Proceedings of the 6th ACM SIGMM international workshop on Multimedia information retrieval*, ACM, 135-142, 2004.

[38] G. Bucci, S. Cagnoni, R. De Dominicis, Integrating content-based retrieval in a medical image reference database[J], *Computerized Medical Imaging and Graphics*, 20(4): 231-241, 1996.

[39] H. Muller, N. Michoux, D. Bandon, et al., A review of content-based image retrieval systems in medical applications¡ªclinical benefits and future directions[J], *International journal of medical informatics* , 73(1): 1-23, 2004.

[40] G. Burel, H. Henoco, Determination of the orientation of 3D objects using spherical harmonics[J], *Graphical Models and Image Processing*, 57(5): 400-408, 1995.

[41] A. Matheny, D.B. Goldgof, The use of three-and four-dimensional surface harmonics for rigid and nonrigid shape recovery and representation[J], *Pattern Analysis and Machine Intelligence, IEEE Transactions on*, 17(10): 967-981, 1995.

[42] T.F. Cootes, C.J. Taylor, D.H. Cooper, et al., Active shape models-their training and application,*Computer Vision and Image Understanding*, 61(1): 38¨C59, 1995.

[43] P.M. Thompson, R.P. Woods, M.S. Mega, et al., Mathematical and computational challenges in creating deformable and probabilistic atlases of the human brain, *Human Brain Mapping*, 9: 81¨C92, 2000.

[44] J.M. Peyrat, M. Sermesant, X. Pennec, et al., A computational framework for the statistical analysis of cardiac diffusion tensors: application to a small database of canine hearts, *IEEE Transactions on Medical Imaging*, 26(11): 1500¨C1514, 2007.

[45] Y.W. Chen, M. Uetani, S. Kohara, et al., Application of statistical shape model of the liver in classification of cirrhosis, *International Journal of Digital Content Technology and Its Applications*, 7(9): 477¨C484, 2013.

[46] M. Ankerst, G. Kastenmuller, H.P. Kriegel et al., Nearest neighbor classification in 3D protein databases, *ISMB*, 99:34-43, 1999.

[47] C. Cortes, V. Vapnik, Support-vector networks[J], *Machine learning*, 20(3):273-297, 1995.

[48] http://en.wikipedia.org/wiki/Support_vector_machine

[49] Y. Freund, R.E. Schapire, Experiments with a new boosting algorithm[C], *ICML*, 96:148-156, 1996.

Chapter 2

Conventional Principle Component Analysis Based Statistical Analysis of Shape and Texture

2.1 Principle Component Analysis (PCA)

As I described in Chapter 1, Principal component analysis (PCA), abbreviated PCA which is also known as the singular value decomposition [1], is usually used for representation and dimension reduction of texture and shape features. PCA is useful for solving problems such as object recognition [2][3], tracking [4]][5], and detection [6][7].

It is generally accepted that PCA was first described by Karl Pearson in 1901 [8].PCA can be defined as the linear projection that minimizes the average projection cost, defined as the mean squared distance between the data points and their projections. Equivalently it can also be defined as the orthogonal projection of the data onto a lower dimensional linear space, known as the principal subspace, such that the variance of the projected data is maximized [9]. Figure 2.1 shows an illustration of PCA. The yellow ones represent the samples, and the horizontal and vertical directions are the original ones. The purpose of PCA is to find the principle component 1(PC1) and principle component 2(PC2).In the next, I will briefly review PCA method.

Consider a data set of observations $\mathbf{x}_n$ where $n = 1, \ldots, N$, and $\mathbf{x}_n$ is a Euclidean variable with

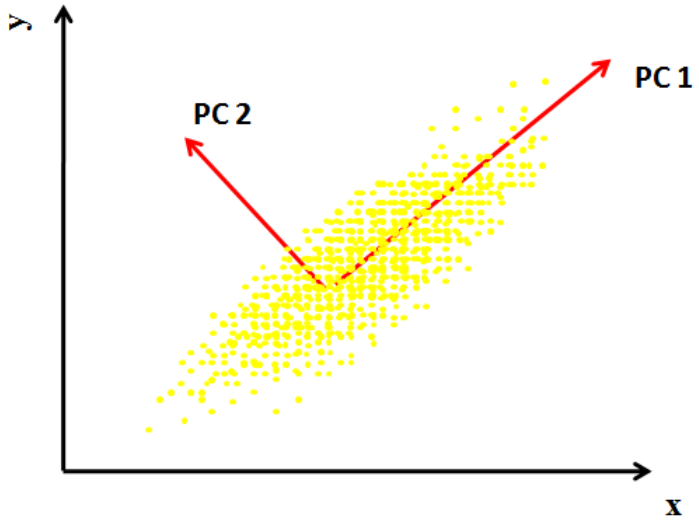

Figure 2.1: The illustration of PCA

dimensionality P. The goal is to project the data onto a space having dimensionality $M<P$ while maximizing the variance of the projected data. The objective function of PCA can be written as:

$$\min_{\mathbf{U}} \|\mathbf{D} - \mathbf{UB}\|_2, s.t.\ rank(\mathbf{U}) < l \tag{2.1}$$

$\mathbf{U}$ is the eigenspace, $\mathbf{B}$ is the coefficient matrix, and $\mathbf{E}$ represents the error part and l is the number of principal components, it is less than or equal to the number of original variables.

To begin with, consider the projection onto a one-dimensional space ($M = 1$). Define the direction of this space using a D-dimensional vector $\mathbf{u}_1$, which for convenience (and without loss of generality) commonly choose a unit vector so that $\mathbf{u}_1^{\mathrm{T}}\mathbf{u}_1 = 1$. Each data point $\mathbf{x}_n$ is then projected onto a scalar value $\mathbf{u}_1^{\mathrm{T}}\mathbf{x}_n$. The mean of the projected data is $\mathbf{u}_1^{\mathrm{T}}\,\bar{\mathbf{x}}$where $\bar{\mathbf{x}}$ is the sample set mean given by:

$$\bar{\mathbf{x}} = \frac{1}{N}\sum_{n=1}^{N}\mathbf{x}_n \tag{2.2}$$

and the variance of the projected data is given by:

$$\frac{1}{N}\sum_{n=1}^{N}\left\{\mathbf{u}_1^{\mathrm{T}}\mathbf{x}_n - \mathbf{u}_1^{\mathrm{T}}\,\bar{\mathbf{x}}\right\}^2 = \mathbf{u}_1^{\mathrm{T}}\mathbf{S}\mathbf{u}_1 \tag{2.3}$$

where $\mathbf{S}$ is the data covariance matrix defined by:

$$\mathbf{S} = \frac{1}{N}\sum_{n=1}^{N}(\mathbf{x}_n - \bar{\mathbf{x}})(\mathbf{x}_n - \bar{\mathbf{x}})^{\mathrm{T}} \tag{2.4}$$

Now maximize the projected variance $\mathbf{u}_1^{\mathrm{T}}\mathbf{S}\mathbf{u}_1$ with respect to $\mathbf{u}_1$ .The appropriate constraint comes from the normalization condition $\mathbf{u}_1^{\mathrm{T}}\mathbf{u}_1 = 1$. To enforce this constraint, Lagrange multiplier λ_1 is applied and then make an unconstrained maximization of:

$$\mathbf{u}_1^{\mathrm{T}}\mathbf{S}\mathbf{u}_1 + \lambda_1(1 - \mathbf{u}_1^{\mathrm{T}}\mathbf{u}_1) \tag{2.5}$$

By setting the derivative with respect to $\mathbf{u}_1$ equal to zero, this quantity will have a stationary point when

$$\mathbf{S}\mathbf{u}_1 = \lambda_1\mathbf{u}_1 \tag{2.6}$$

which says that $\mathbf{u}_1$ must be an eigenvector of $\mathbf{S}$. So the variance will be a maximum when setting $\mathbf{u}_1$ equal to the eigenvector having the largest eigenvalue λ_1 . This eigenvector is known as the first principal component.

It can define additional principal components in an incremental fashion by choosing each new direction to be that which maximizes the projected variance among at all possible directions orthogonal to those already considered. If in the general case of an M-dimensional projection space, the optimal linear projection for which the variance of the projected data is maximized is now defined by the M eigenvectors $\mathbf{u}_1 \cdots \mathbf{u}_M$ of the data covariance matrix $\mathbf{S}$ corresponding to the M largest eigenvalues $\lambda_1 \ldots \lambda_M$.

2.2 Statistical Analysis of Shape

The statistical shape model (SSM) is one of the most important applications of principle component analysis (PCA). In 1991, Cootes and Cooper [20] proposed a parametric statistical shape model that

was based on PCA. Following this, Cootes et al. proposed a point distribution model [21] that is generated from examples of shapes, where each shape is represented by a set of labeled points $\mathbf{x} = (x_1, x_2, \ldots, x_N, y_1, y_2, \ldots, y_N, z_1, z_2, \ldots, z_N)$,; here N represents the number of surface points. One of the most well-known methods for surface point extraction is the marching cube [22]; see Figure 2.2 for an example of the marching cube method.

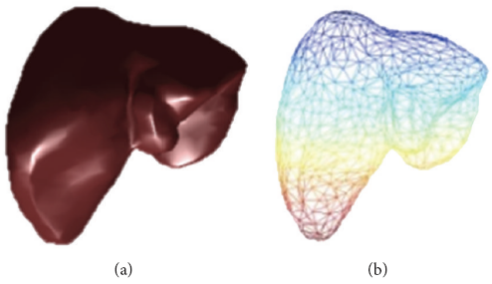

Figure 2.2: Marching cube method: (a) volume data and (b) triangulated mesh surface data.

The resulting shape model can then be used to generate a new shape, as follows:

$$\mathbf{x} = \bar{\mathbf{x}} + \mathbf{U}\mathbf{b} \tag{2.7}$$

where $\bar{\mathbf{x}}$ represents the mean shape, $\mathbf{U}$ is the matrix of eigenspace vectors, and $\mathbf{b}$ contains the shape parameters. Figure 2.3 shows a schematic diagram of the SSM. Here, L is the number of samples, N is the number of surface points, and $\mathbf{x}_i^j$ is the column vector that represents the coordinate for the j^{th} surface point of the i^{th} sample. The shape can be changed by modifying the parameters $\mathbf{b}$, as shown in Figure 2.4; the standard deviation (SD) is also indicated.

The shape can be changed by modifying the parameters $\mathbf{b}$, as shown in Figure 2.3; the standard deviation (SD) is also indicated.

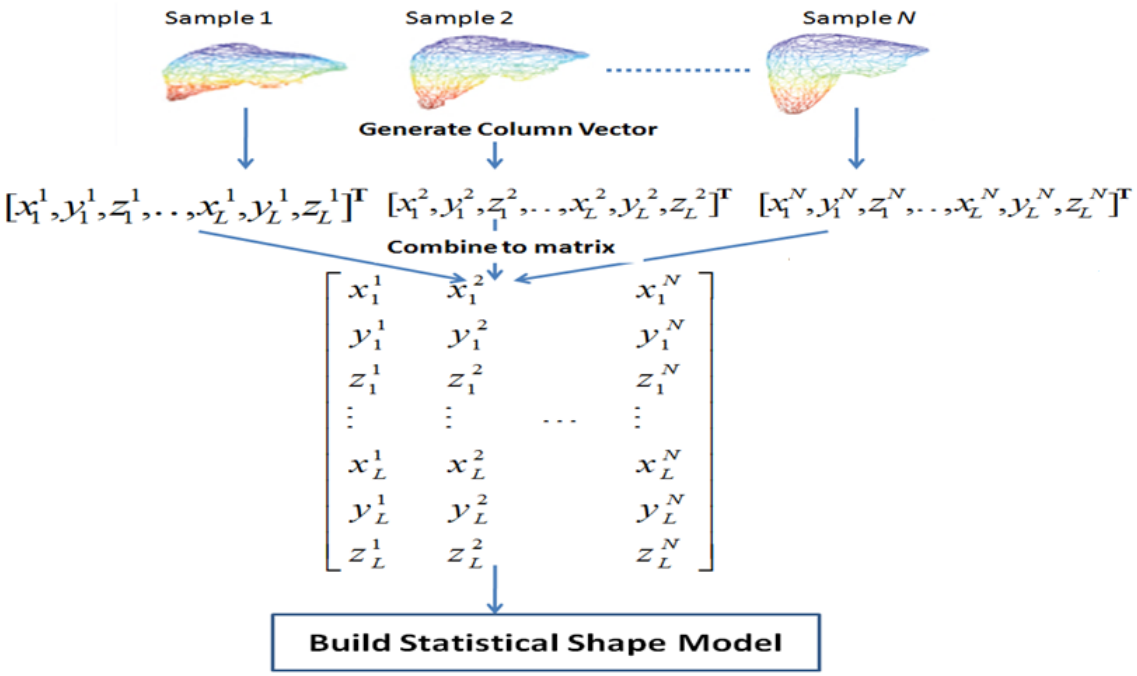

Figure 2.3: The schematic diagram of SSM.

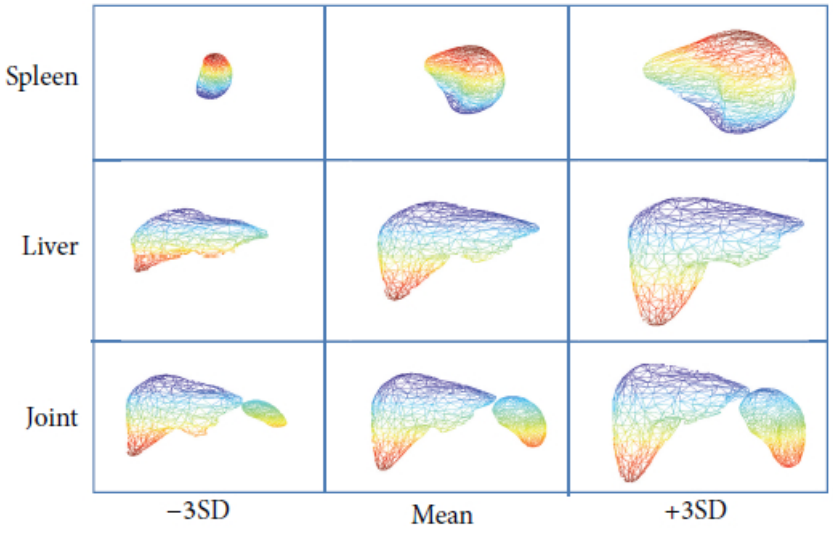

Figure 2.4: The shape variations with changing the parameters [23].

2.3 Statistical Analysis of Texture

For detection of images or various local objectives, shape information is not sufficient. The authors in reference[24] proposed the active shape model (ASM), which uses SSM to locate a human face. Since

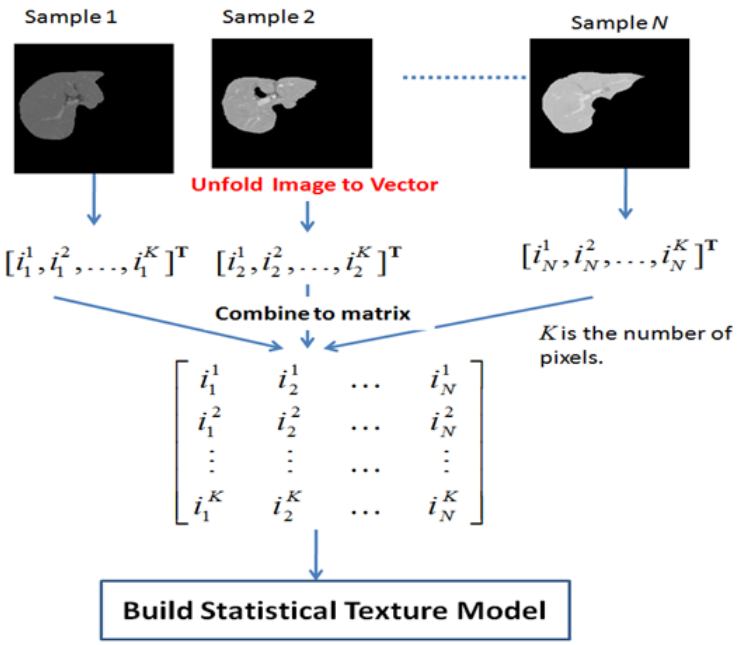

Figure 2.5: The schematic diagram of statistical texture model.

the ASM suffers from a lack of the information about intensity values, the active appearance model (AAM) was proposed [25]. Here, "appearance" means the intensity or texture of an image. In recent years, the model-based methods have been widely used in 3D medical imaging applications [26][27]. Statistical shape analysis and statistical texture analysis differ primarily in the elements contained in the input vector $\mathbf{x}$. For statistical shape analysis, the elements of the input vector are the coordinates of the surface points, as mentioned above. For statistical texture analysis, the volume image (3D) must first be unfolded into a 1D vector, which is then used as $\mathbf{x}$. Figure 2.5 shows a schematic diagram of the statistical texture model. Here, i_p^q represents the q^{th} point of the p^{th} sample, and M is the number of pixels (voxels). When the parameters $\mathbf{b}$ are modified, the texture is changed. However, due to the unfolding of the volume image (3D) into a 1D vector, the dimensionality of the data is high, and the spatial structure will be lost.

Bibliography

[1] G. Golub, W. Kahan, Calculating the singular values and pseudo-inverse of a matrix[J], *Journal of the Society for Industrial & Applied Mathematics, Series B: Numerical Analysis*, 2(2):205-224, 1965.

[2] T. Ahonen, A. Hadid, M. Pietikainen, Face description with local binary patterns: Application to face recognition[J], *Pattern Analysis and Machine Intelligence, IEEE Transactions on*, 28(12):2037-2041, 2006.

[3] B.A. Draper, K. Baek, M.S. Bartlett et al., Recognizing faces with PCA and ICA[J], *Computer vision and image understanding* , 91(1):115-137, 2003.

[4] C. Beleznai, B. Fruhstuck, H. Bischof, Multiple object tracking using local PCA[C], *18th International Conference on Pattern Recognition*, 3:79-82, 2006.

[5] A. Yilmaz, O. Javed, M. Shah, Object tracking: A survey[J], *Acm computing surveys (CSUR)*, 38(4):13, 2006.

[6] H. Ringberg, A. Soule, J. Rexford et al., Sensitivity of PCA for traffic anomaly detection[C], *ACM SIGMETRICS Performance Evaluation Review*, 35(1):109-120, 2007.

[7] D. Brauckhoff, K. Salamatian, M. May, Applying PCA for traffic anomaly detection: Problems and solutions[C],*INFOCOM 2009* , 2866-2870, 2009.

[8] K.LIII. Pearson, On lines and planes of closest fit to systems of points in space[J], *The London, Edinburgh, and Dublin Philosophical Magazine and Journal of Science*, 2(11):559-572, 1901.

[9] H. Hotelling, Analysis of a complex of statistical variables into principal components[J], *Journal of educational psychology*, 24(6):417, 1933.

[10] M. Artac, M. Jogan, A. Leonardis, Incremental PCA for on-line visual learning and recognition[C], *International Conference on Pattern Recognition*, 3:781-784, 2002.

[11] F. De la Torre, M.J. Black, Robust principal component analysis for computer vision[C], *International Conference on Computer Vision*, 1:362-369, 2001.

[12] B. Scholkopf, A. Smola, K.R. Muller, Kernel principal component analysis[M],*Artificial Neural Networks — ICANN'97. Springer Berlin Heidelberg*, 583-588, 1997.

[13] H. Wang, X.J. Wu, Weighted PCA space and its application in face recognition[C], *International Conference on. Machine Learning and Cybernetics*, 7:4522-4527, 2005.

[14] M. Turk, A. Pentland, Eigenfaces for Recognition, *Journal of Cognitive Neuroscience*, 3(1):71-86, 1991.

[15] J. Yang, D. Zhang, A.F. Frangi et al., Two-Dimensional PCA: A New Approach to Appearance-based Face Representation and Recognition, *IEEE Trans.on PAMI*, 26(1):131-137, 2004.

[16] H. Kong, X. Li, L. Wang et al., Generalized 2D Principal Component Analysis for Face Image Representation and Recognition, *Neural Networks*, 18:585-594, 2005.

[17] H.C. Yu, M. Bennamoun, 1D-PCA,2D-PCA to nD-PCA, *The 18th International Conference on Pattern Recognition(ICPR'06)*, 4:181-184, 2006.

[18] L.D. Lathauwer, B.D. Moor, J. Vandewalle, A Multilinear Singular Value Decomposition, *SIAM Journal of Matrix Analysis and Application*, 21(4):1253-1278, 2001

[19] R. Xu, Y.W. Chen, Appearance Models for Medical Volumes with Few Samples by Generalized 3D-PCA, *Lecture Notes in Computer Science, Springer, LNCS 4984*, 821-830, 2008.

[20] T.F. Cootes, D.H. Cooper, C.J. Taylor et al., Trainable method of parametric shape description[J], *Image and Vision Computing*, 10(5):289-294, 1992.

[21] T.F. Cootes, C.J. Taylor, D.H. Cooper et al., Training models of shape from sets of examples[M], *BMVC92. Springer London*, 9-18, 1992.

[22] W.E. Lorensen, H.E. Cline, Marching cubes: a high resolution 3D surface construction algorithm, *Computer Graphics*, 21(4):163-169, 1987.

[23] Y.W. Chen, J. Luo, C. Dong, et al., Computer-aided diagnosis and quantification of cirrhotic livers based on morphological analysis and machine learning[J], *Computational and mathematical methods in medicine*, 2013.

[24] T.F. Cootes, G.J. Edwards, C.J. Taylor, Active appearance models[M], *Computer Vision*!'^{a}*ECCV'98. Springer Berlin Heidelberg*, 484-498, 1998.

[25] T.F. Cootes, G.J. Edwards, C.J. Taylor, Active appearance models[J], *IEEE Transactions on pattern analysis and machine intelligence*, 23(6):681-685, 2001.

[26] H.C. van Assen, M.G. Danilouchkine, F. Behloul et al., Cardiac LV segmentation using a 3D active shape model driven by fuzzy inference[M], *Medical Image Computing and Computer-Assisted Intervention-MICCAI 2003. Springer Berlin Heidelberg*, 533-540, 2003.

[27] M.R. Kaus, J. Berg, J. Weese et al., Automated segmentation of the left ventricle in cardiac MRI[J], *Medical Image Analysis*, 8(3): 245-254, 2004.

Chapter 3

Statistical Analysis of Texture based on Linear Tensor Coding

3.1 Introduction

In the recent years, the research of digital atlases is a popular and important topic in the medical volume processing [1][2]. Many problems in medical volumes interpretation involve the need of a modeling to understand the volumes with which it is presented, thus well representation of medical volumes is very important part of computer-aided diagnosis (CAD). The difficulty for statistical texture appearance model is high dimension of the data. In conventional PCA based method, the medical volume (3D image) should be first unfolded to a 1D vector. The spatial structure will be lost. And it also suffers large-computation and over-fitting problems because the very large dimension of the data. In reference[10], Xu and Chen have proposed generalized N-dimensional principal component analysis (GND-PCA) for the modeling of a series of medical volumes, which is based on multi-linear algebra. In GND-PCA, the medical volume is treated as a third-order tensor and it do not need to be unfolded to a 1D vector. It was able to achieve good performance on construction of statistical appearance models for medical volumes with few samples. The medical volume (the 3D medical image) was treated as a 3rd-order tensor, and the optimal subspace on each mode was calculated simultaneously by minimizing of the square error between the original volumes based on the subspace

with an iteration algorithm. While, this method has some disadvantages, such as each basis of the GND-PCA not being independent and thus making the core tensor of the final result redundant. Also it is difficult to choose the distinctive basis for classification.

To solve the these problems, in previous work, Qiao et al. proposed a linear tensor coding (LTC) algorithm, which can achieve more compact and meaningful tensor basis than GND-PCA [13, 14]. In this work, I applied it to statistical texture modeling of medical volumes. With LTC, medical volumes can be represented by a linear combination of basis, which are mutually independent. Furthermore it is possible to choose the distinctive basis for classification.

My proposed method was evaluated by a liver database which contained 10 normal data and 10 abnormal data with intensity changed through two aspects: medical image reconstruction and liver diagnosis. For reconstruction, with the same basis, LTC can get larger reconstruction rate than GND-PCA. Additionally, in the diagnosis part, I firstly chose the distinctive basis based on the correlation between category labels and the coefficients of LTC basis and then I use the selected basis for diagnosis. The diagnosis accuracy can be significantly improved by the use of selected distinctive basis.

3.2 Related Work

3.2.1 Tensor and Multilinear Algebra Foundations

3.2.1.1 Definitions and Preliminaries

Scalers are denoted by italic-shape letters, i.e. $(a, b, ...)$ or $(A, B, ...)$. Bold lower case letters, i.e. $(\mathbf{a}, \mathbf{b}, ...)$, are used to represent vectors. Matrices are denoted by bold upper case letters, i.e. $(\mathbf{A}, \mathbf{B}, ...)$; and higher-order tensors (more than third order tensor) are denoted by calligraphic upper case letters, i.e. $(\mathcal{A}, \mathcal{B}, ...)$.

A tensor is a multidimensional array. The order of a tensor in the number of dimensions, as known as ways or modes. An N-th order tensor $\mathcal{A}$ is defined as a multi-array with N indices, where

$\mathcal{A} \in \mathbb{R}^{I_1 \times I_2 \times \ldots \times I_N}$ and $\mathbb{R}$ is the real manifold. Elements of the tensor $\mathcal{A}$ are denoted as $a_{i_1 \ldots i_n \ldots i_N}$, where $1 \leqslant i_n \leqslant I_n$. The space of the N-th order tensor is comprised by the N mode subspaces. From the perspective of $\mathcal{A}$, scalars, vectors and matrices can be seen as zeroth-order, first order and second order tensors, respectively.

The ith entry of a vector $\mathbf{a}$ is denoted by a_i, element (i, j) of a matrix $\mathbf{A}$ is denoted by a_{ij}, and element (i, j, k) of a 3rd-order tensor $\mathcal{X}$ is denoted by x_{ijk}. Indices typically range from 1 to their capital version, e.g., $i = 1, ..., I$. The nth element in a sequence is denoted by a superscript in parentheses, e.g., $\mathbf{A}^n$ denotes the nth matrix in a sequence.

Subarrays are formed when a subset of the indices is fixed. For matrices, these are the rows and columns. A colon is used to indicate all elements of a mode. Thus, the jth column of $\mathbf{A}$ is denoted by $\mathbf{a}_{:j}$, and the ith row of $\mathbf{A}$ is denoted by $\mathbf{a}_{i:}$.

Fibers are the higher-order analogue of matrix rows and columns. A fiber is defined by fixed every index but one. A matrix column is a mode-1 fiber and a matrix row is a mode-2 fiber. 3rd-order tensors have column, row, and tube fibers, denoted as $\mathbf{x}_{:jk}$, $\mathbf{x}_{i:k}$, and $\mathbf{x}_{ij:}$, respectively. Fibers of a 3rd-order tensors are shown in Figure 3.1.

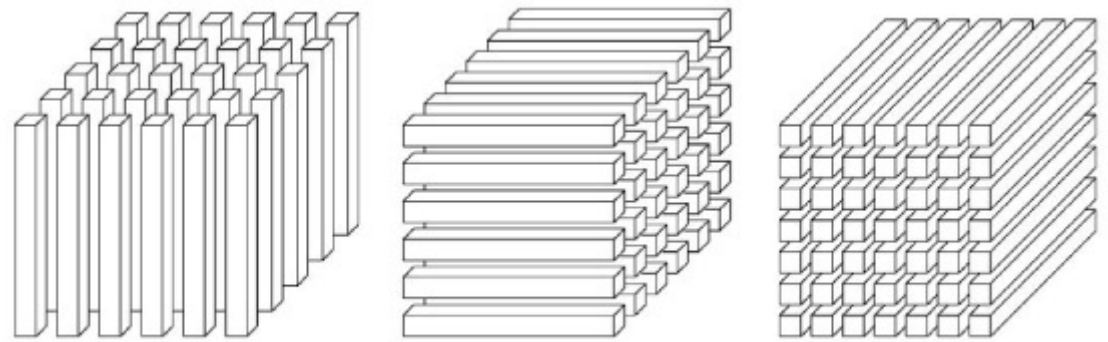

Figure 3.1: Fibers of a 3rd-order tensor.

Slices are two-dimensional sections of a tensor, defined by fixing all but two indices. Fig. 3.2 shows

the horizontal, lateral, and frontal slides of a 3rd-order tensor $\mathcal{X}$, denoted by $\mathbf{X}_{i::}$, $\mathbf{X}_{:j:}$, and $\mathbf{X}_{::k}$, respectively.

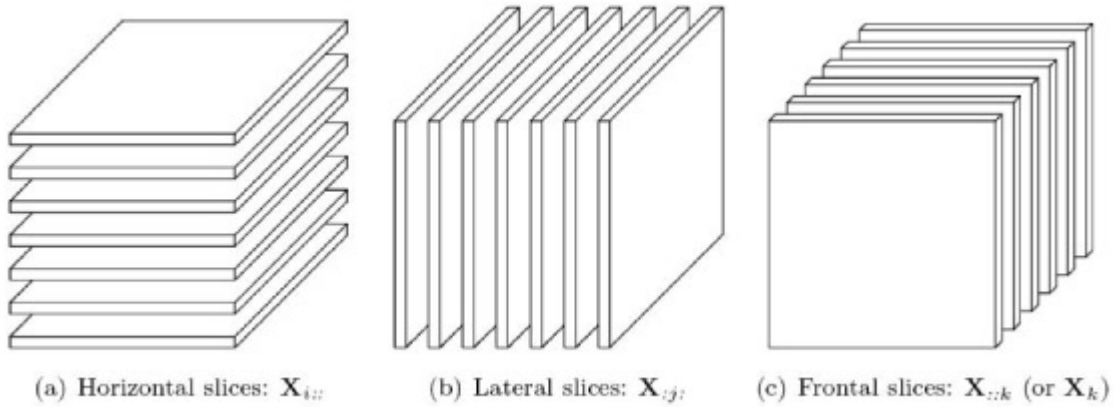

Figure 3.2: Slices of a 3rd-order tensor.

The norm of a tensor $\mathcal{X} \in \mathbb{R}^{I_1 \times I_2 \times \ldots \times I_N}$ is the square root of the sum of the squares of all its elements, i.e.,

$$\| \mathcal{X} \| = \sqrt{\sum_{i_1=1}^{I_1} \sum_{i_2=1}^{I_2} \cdots \sum_{i_N=1}^{I_N} x_{i_1 i_2 \cdots i_N}^2}. \tag{3.1}$$

This is analogous to the matrix Frobenius norm, which is denoted $\| \mathbf{A} \|$ for a matrix $\mathbf{A}$.

The inner product of two same-sized tensors $\mathcal{X}, \mathcal{Y} \in \mathbb{R}^{I_1 \times I_2 \times \ldots \times I_N}$ is the sum of the products of their entries, i.e.,

$$< \mathcal{X}, \mathcal{Y} > = \sum_{i_1=1}^{I_1} \sum_{i_2=1}^{I_2} \cdots \sum_{i_N=1}^{I_N} x_{i_1 i_2 \cdots i_N} y_{i_1 i_2 \cdots i_N}. \tag{3.2}$$

It follows immediately that $< \mathcal{X}, \mathcal{X} > = \| \mathcal{X} \|^2$.

A Nth-order tensor $\mathcal{X} \in \mathbb{R}^{I_1 \times I_2 \times \ldots \times I_N}$ is rank one if it can be written as the outer product of N vectors, i.e.,

$$\mathcal{X} = \mathbf{a}^{(1)} \otimes \mathbf{a}^{(2)} \otimes \cdots \otimes \mathbf{a}^{(N)}. \tag{3.3}$$

The symbol"$\circ$" represents the vector outer product. This means that each element of the tensor is the product of the corresponding vector elements: $x_{i_1 i_2 \cdots i_N} = a_{i_1}^{(1)} a_{i_2}^{(2)} \cdots a_{i_N}^{(N)}$, for all $1 \leq i_n \leq I_N$.

Fig. 3.3 illustrates $\mathcal{X} = \mathbf{a} \otimes \mathbf{b} \otimes \mathbf{c}$, a third-order rank-one tensor.

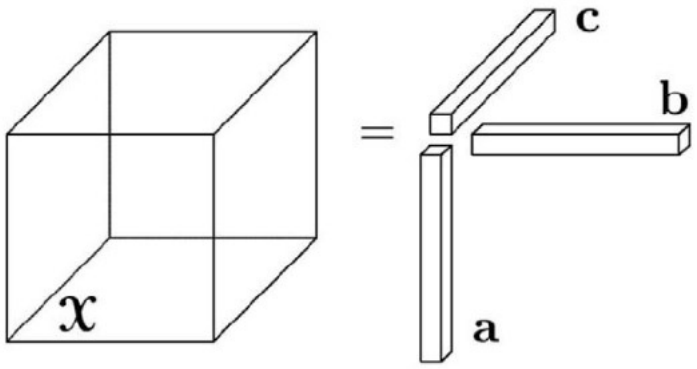

Figure 3.3: Rank-one 3rd-order tensor, $\mathcal{X} = \mathbf{a} \otimes \mathbf{b} \otimes \mathbf{c}$.

Matricization, also known as unfolding or flattening, is the process of reordering the elements of an Nth-order array into a matrix. For example. a $2 \times 3 \times 4$ tensor can be arranged as a 6×4 matrix or a 3×8 matrix, and so on. The mode-n matricization of a tensor $\mathcal{X} \in \mathbb{R}^{I_1 \times I_2 \times \ldots \times I_N}$ is denoted by and arranges the mode-n fibers to be the columns of the resulting matrix. Tensor elements $(i_1, i_2, \cdots, i_N)$ maps to matrix element(i_n, j), where

$$j = 1 + \sum_{k=1, k \neq n}^{N} (i_k - 1) J_k, with\ J_k = \prod_{m=1, m \neq n}^{k-1} I_m. \tag{3.4}$$

Fig. 3.4 illustrates a example of matricization for a 3rd-order tensor.

3.2.1.2 Operations of Tensor

Tensor can be multiplied together, though obviously the notation and symbols for this are much more complex than for matrices. Here I consider only the tensor n-mode product, i.e., multiplying a tensor by a matrix (or a vector) in mode n.

The n-mode (matrix) product of a tensor $\mathcal{X} \in \mathbb{R}^{I_1 \times I_2 \times \ldots \times I_N}$ with a matrix $\mathbf{U} \in \mathbb{R}^{J \times I_n}$ is denoted by $\mathcal{X} \times_n \mathbf{U}$ and is of size $I_1 \times I_2 \times ... \times I_{n-1} \times J \times I_{n+1} ... \times I_N$. Elementwise, I have

$$(\mathcal{X} \times_n \mathbf{U})_{i_1 \cdots i_{n-1} j i_{n+1} \cdots i_N} = \sum_{i_n=1}^{I_N} x_{i_1 i_2 \cdots i_N} u_{j i_n}.$$

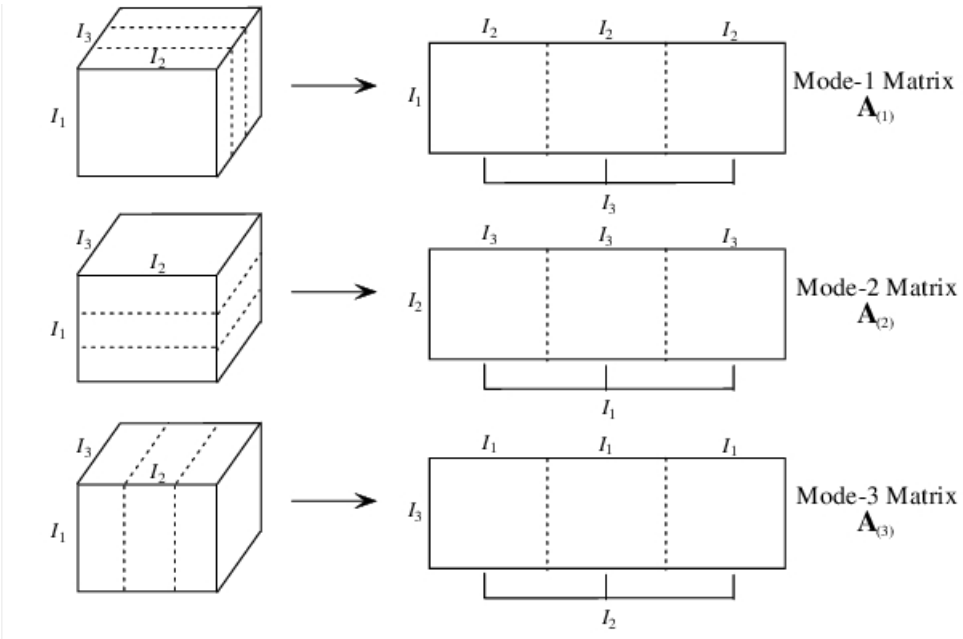

Figure 3.4: Matricization of a 3rd-order tensor.

Each mode-n fiber is multiplied by the matrix $\mathbf{U}$. The idea can also be expressed in terms of unfolder tensors:

$$\mathcal{Y} = \mathcal{X} \times_n \mathbf{U} \Leftrightarrow Y_n = \mathbf{U}X_n.$$

A few facts regarding n-mode matrix products are in order. For distinct modes in a series of multiplications, the order of the multiplication is irrelevant, i.e.,

$$\mathcal{X} \times_m A \times_n B = \mathcal{X} \times_n B \times_m A, m \neq n.$$

If the modes are the same, then

$$\mathcal{X} \times_n A \times_n B = \mathcal{X} \times_n (BA), m = n.$$

The n-mode (vector) product of a tensor $\mathcal{X} \in \mathbb{R}^{I_1 \times I_2 \times \ldots \times I_N}$ with a vector $\mathbf{v} \in \mathbb{R}^{I_n}$ is denoted by $\mathcal{X} \times_n \mathbf{v}$. The result is of order $N-1$, i.e., the size is $I_1 \times I_2 \times \ldots \times I_{n-1} \times I_{n+1} \ldots \times I_N$. Elementwise,

$$(\mathcal{X} \times_n \mathbf{v})_{i_1 \cdots i_{n-1} i_{n+1} \cdots i_N} = \sum_{i_n=1}^{I_N} x_{i_1 i_2 \cdots i_N} v_{i_n}.$$

The idea is to compute the inner product of each mode-n fiber with the vector.

3.2.2 GND-PCA

GND-PCA was proposed by Xu and Chen et al. for statistical appearance modeling of medical volumes with few samples[10]. The medical volume is treated as a 3rd-order tensor, and the optimal subspace on each mode is calculated simultaneously by minimizing of the square error between the original volumes and reconstructed ones. In the following part of this section, I will briefly review the algorithm of GND-PCA.

Given a series of the $N-th$ order tensors with zero-mean[1] $\mathcal{A}_i \in \mathbb{R}^{I_1 \times I_2 \times \cdots \times I_N}, i = 1, 2, ..., M$, $\sum_{i=1}^{M} \mathcal{A}_i = 0$, I hope to find another series of lower rank-$(J_1, J_2, ..., J_N)$ tensors $\hat{\mathcal{A}}_i$ which can most accurately approximate the original tensors, where $J_n < I_n$. The new series of tensors can be decomposed by the same N matrices $\mathbf{U}^{(n)} \in \mathbb{R}^{I_n \times J_n}$ with orthogonal columns according to tucker model which can be shown by Eq. 3.5.

$$\hat{\mathcal{A}}_i = \mathcal{B}_i \times_1 \mathbf{U}^{(1)} \times_2 \mathbf{U}^{(2)} \times ... \times_n \mathbf{U}^{(n)} \times ... \times_N \mathbf{U}^{(N)} \tag{3.5}$$

where $\mathcal{B}_i \in \mathbb{R}^{J_1 \times J_2 \times ... \times J_n \times ... \times J_N}$ are the core tensors.

$$S = \sum_{i=1}^{M} \| \mathcal{A}_i - \hat{\mathcal{A}}_i \|^2 = \sum_{i=1}^{M} \| \mathcal{A}_i - \mathcal{B}_i \times_1 \mathbf{U}^{(1)} \times_2 \mathbf{U}^{(2)} \times ... \times_N \mathbf{U}^{(N)} \|^2 \tag{3.6}$$

The orthogonal matrices $\mathbf{U}^{(n)}$ can be determined by minimizing the cost function shown by Eq. 3.6. The cost function is defined as a mean square error between the original tensor and the reconstructed tensor.

In Eq. 3.6, only the tensors $\mathcal{A}_i$ are known. However, supposing the N matrices $\mathbf{U}^{(n)}$ are known,

[1] if the tensors do not have zero-mean, I can subtract the mean-value from each tensor to obtain a new series of tensors $\mathcal{A}'_i$ which have zero-mean, i.e. $\mathcal{A}'_i = \mathcal{A}_i - \frac{1}{M} \sum_{i=1}^{M} \mathcal{A}_i$

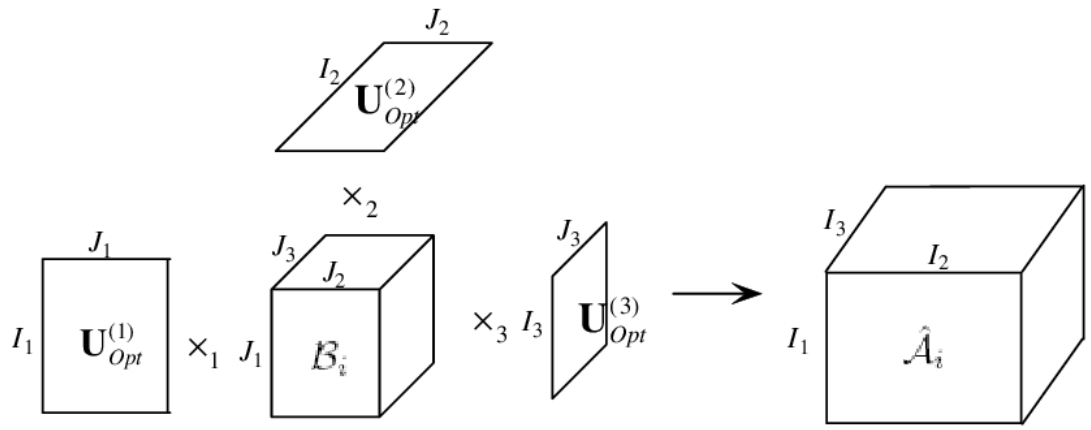

Figure 3.5: Illustration of reconstructing a third order tensor by the three orthogonal bases of mode subspaces $\mathbf{U}^{(1)}_{opt}, \mathbf{U}^{(2)}_{opt}, \mathbf{U}^{(3)}_{opt}$ and the projections $\mathcal{B}_i$.

the answer of $\mathcal{B}_i$ to minimize Eq. 3.6 is merely the result of the traditional linear least-square problem.

Theorem 3.2.1 can be obtained.

Theorem 3.2.1. *Given fixed N matrices $\mathbf{U}^{(n)}$, the tensors $\mathcal{B}_i$ that minimize the cost function, Eq. 3.6, are given by $\mathcal{B}_i = \mathcal{A}_i \times_1 \mathbf{U}^{(1)^T} \times_2 \mathbf{U}^{(2)^T} \times ... \times_N \mathbf{U}^{(N)^T}$*

The proof of Theorem 3.2.1 is simple, so it is omitted. With the help of Theorem 3.2.1, Theorem 3.2.2 can be obtained.

Theorem 3.2.2. *If the tensors $\mathcal{B}_i$ are chosen as $\mathcal{B}_i = \mathcal{A}_i \times_1 \mathbf{U}^{(1)^T} \times_2 \mathbf{U}^{(2)^T} \times ... \times_N \mathbf{U}^{(N)^T}$, minimization of the cost function Eq. 3.6 is equal to maximization of the following cost function S', where*

$$S' = \sum_{i=1}^{M} \parallel \mathcal{A}_i \times_1 \mathbf{U}^{(1)^T} \times_2 \mathbf{U}^{(2)^T} \times ... \times_N \mathbf{U}^{(N)^T} \parallel^2.$$

Proof. The cost function can be expanded, shown as $S = \sum_{i=1}^{M} \parallel \mathcal{A}_i - \hat{\mathcal{A}}_i \parallel^2 = \sum_{i=1}^{M} (\parallel \mathcal{A}_i \parallel^2 -2\langle \mathcal{A}_i, \hat{\mathcal{A}}_i \rangle + \parallel \hat{\mathcal{A}}_i \parallel^2)$. According to the definition of inner product of tensor, I can write the inner product $\langle \mathcal{A}_i, \hat{\mathcal{A}}_i \rangle$ as $\langle \mathcal{A}_i, \hat{\mathcal{A}}_i \rangle = \langle \mathcal{A}_i, \mathcal{B}_i \times_1 \mathbf{U}^{(1)} \times_2 \mathbf{U}^{(2)} \times ... \times_N \mathbf{U}^{(N)} \rangle = \langle \mathcal{A}_i \times_1 \mathbf{U}^{(1)^T} \times_2 \mathbf{U}^{(2)^T} \times ... \times_N \mathbf{U}^{(N)^T}, \mathcal{B}_i \rangle = \langle \mathcal{B}_i, \mathcal{B}_i \rangle = \parallel \mathcal{B}_i \parallel^2$. Since the matrices $\mathbf{U}^{(n)}$ have orthogonal columns, they will not affect the Frobenius norm. Therefore, I get $\parallel \hat{\mathcal{A}}_i \parallel = \parallel \mathcal{B}_i \parallel$. Substituting $\langle \mathcal{A}_i, \hat{\mathcal{A}}_i \rangle = \parallel \mathcal{B}_i \parallel^2$ and $\parallel \hat{\mathcal{A}}_i \parallel = \parallel \mathcal{B}_i \parallel$ into the cost function, I can get $S = \sum_{i=1}^{M} (\parallel \mathcal{A}_i \parallel^2 - \parallel \mathcal{B}_i \parallel^2) = \sum_{i=1}^{M} (\parallel \mathcal{A}_i \parallel^2 - \parallel \mathcal{A}_i \times_1 \mathbf{U}^{(1)^T} \times_2 \mathbf{U}^{(2)^T} \times ... \times_N \mathbf{U}^{(N)^T} \parallel^2) = \sum_{i=1}^{M} \parallel \mathcal{A}_i \parallel^2 - S'$. The first term, $\sum_{i=1}^{M} \parallel \mathcal{A}_i \parallel^2$, has a fixed value, so minimization of cost function is equal to maximization of the last term S'. The theorem is proved. □ □

There is no close-form solution to simultaneously resolve the matrices $\mathbf{U}^{(n)}$ for the cost function S'; however the explicit solution for one matrix can be obtained if the other matrices are fixed. This is expressed by Lemma 3.2.3.

Lemma 3.2.3. *Given the fixed matrices, $\mathbf{U}^{(1)}, \mathbf{U}^{(2)}, ..., \mathbf{U}^{(n-1)}, \mathbf{U}^{(n+1)}, \mathbf{U}^{(N)}$, if the columns of the matrix $\mathbf{U}^{(n)}$ are selected as the first J_n leading eigenvectors of the matrix $\sum_{i=1}^{M} (\mathbf{C}_{i(n)} \cdot \mathbf{C}_{i(n)}^T)$, $\mathbf{C}_{i(n)}$ is the mode-n matrix of the tensor $\mathcal{C}_i = \mathcal{A}_i \times_1 \mathbf{U}^{(1)^T} \times_2 \mathbf{U}^{(2)^T} \times ... \times_{n-1} \mathbf{U}^{(n-1)^T} \times_{n+1} \mathbf{U}^{(n+1)^T} \times ... \times_N \mathbf{U}^{(N)^T}$, the cost function S' can be maximized.*

Proof. I can first represent S' by $S' = \sum_{i=1}^{M} \parallel \mathcal{A}_i \times_1 \mathbf{U}^{(1)^T} \times_2 \mathbf{U}^{(2)^T} \times ... \times_N \mathbf{U}^{(N)^T} \parallel^2 = \sum_{i=1}^{M} \parallel (\mathcal{A}_i \times_1 \mathbf{U}^{(1)^T} \times_2 \mathbf{U}^{(2)^T} \times ... \times_{n-1} \mathbf{U}^{(n-1)^T} \times_{n+1} \mathbf{U}^{(n+1)^T} \times ... \times_N \mathbf{U}^{(N)^T}) \times_n \mathbf{U}^{(n)^T} \parallel^2 = \sum_{i=1}^{M} \parallel \mathcal{C}_i \times_n \mathbf{U}^{(n)^T} \parallel^2 = \sum_{i=1}^{M} \parallel \mathbf{U}^{(n)^T} \cdot \mathbf{C}_{i(n)} \parallel^2 = \sum_{i=1}^{M} tr(\mathbf{U}^{(n)^T} \cdot \mathbf{C}_{i(n)} \cdot \mathbf{C}_{i(n)}^T \cdot \mathbf{U}^{(n)}) = tr(\mathbf{U}^{(n)^T} \cdot \sum_{i=1}^{M} (\mathbf{C}_{i(n)} \cdot \mathbf{C}_{i(n)}^T) \cdot \mathbf{U}^{(n)})$. Therefore, maximization of the cost function S' is the same as maximization of $tr(\mathbf{U}^{(n)^T} \cdot \sum_{i=1}^{M} (\mathbf{C}_{i(n)} \cdot \mathbf{C}_{i(n)}^T) \cdot \mathbf{U}^{(n)})$. This is a well-resolved problem. The solution is to select columns of the matrix $\mathbf{U}^{(n)}$ as the first J_n leading eigenvectors of the matrix $\sum_{i=1}^{M} (\mathbf{C}_{i(n)} \cdot \mathbf{C}_{i(n)}^T)$. □ □

According to Lemma 3.2.3 I can use an iteration algorithm to get the N optimal matrices, $\mathbf{U}_{opt}^{(1)}$, $\mathbf{U}_{opt}^{(2)}, ..., \mathbf{U}_{opt}^{(N)}$, which are able to maximize the cost function S'. This algorithm is summarized as Algorithm 1.

Using the calculated matrices $\mathbf{U}_{opt}^{(n)}, n = 1, 2, ..., N$, each of the volume $\mathcal{A}_i$ can be approximated by $\hat{\mathcal{A}}_i$ with least errors, where $\hat{\mathcal{A}}_i = \mathcal{B}_i \times_1 \mathbf{U}_{opt}^{(1)} \times_2 \mathbf{U}_{opt}^{(2)} \times ... \times_N \mathbf{U}_{opt}^{(N)}$ and $\mathcal{B}_i = \mathcal{A}_i \times_1 \mathbf{U}_{opt}^{(1)^T} \times_2 \mathbf{U}_{opt}^{(2)^T} \times ... \times_N \mathbf{U}_{opt}^{(N)^T}$. The approximation can be illustrated by Fig. 3.5 for the 3-dimensional case. In GND-PCA, the matrices $\mathbf{U}_{opt}^{(n)}, n = 1, 2, ..., N$ construct the bases on the N mode-subspaces; and the core tensor $\mathcal{B}_i$ are the projections on these mode-subspaces.

3.3 Linear Tensor Coding

Alhough GND-PCA can achieve good performance on construction of statistical appearance models for medical volumes with few samples, there are some disadvantages. Each basis of GND-PCA is not independent, so the core tensor of the final result is still redundant. And it is difficult to understand the meaning of each basis. Thus for given a series of the N-order tensors with zero-means $\mathcal{A}_i \in$

Algorithm 1 The algorithm of GND-PCA. $\mathbf{U}_{opt}^{(1)}, \mathbf{U}_{opt}^{(2)}, ..., \mathbf{U}_{opt}^{(N)}$

IN: a series of $N-th$ order tensors, $\mathcal{A}_i \in \mathbb{R}^{I_1 \times\ I_2 \times ... \times I_N}, i = 1, 2, ..., M$.
OUT: N Matrices $\mathbf{U}_{opt}^{(n)} \in \mathbb{R}^{I_n \times J_n}$ $(J_n < I_n, n = 1, 2, ..., N)$ with orthogonal column vectors.

1. Initial values: $k = 0$ and $\mathbf{U}_0^{(n)}$ whose columns are determined as the first J_n leading eigenvectors of the matrices $\sum_{i=1}^{M} (\mathbf{A}_{i(n)} \cdot \mathbf{A}_{i(n)}^T)$.

2. Iterate for k until convergence

   - Maximize $S' = \sum_{i=1}^{M} \| \mathcal{C}_i \times_1 \mathbf{U}^{(1)^T} \|^2$, $\mathcal{C}_i = \mathcal{A}_i \times_2 \mathbf{U}_k^{(2)^T} \times ... \times_N \mathbf{U}_k^{(N)^T}$
     Solution: $\mathbf{U}^{(1)}$ whose columns are determined as the first J_1 leading eigenvectors of $\sum_{i=1}^{M} (\mathbf{C}_{i(1)} \cdot \mathbf{C}_{i(1)}^T)$
     Set $\mathbf{U}_{k+1}^{(1)} = \mathbf{U}^{(1)}$.

   - Maximize $S' = \sum_{i=1}^{M} \| \mathcal{C}_i \times_2 \mathbf{U}^{(2)^T} \|^2$, $\mathcal{C}_i = \mathcal{A}_i \times_1 \mathbf{U}_{k+1}^{(1)^T} \times_3 \mathbf{U}_k^{(3)^T} \times ... \times_N \mathbf{U}_k^{(N)^T}$
     Solution: $\mathbf{U}^{(2)}$ whose columns are determined as the first J_2 leading eigenvectors of $\sum_{i=1}^{M} (\mathbf{C}_{i(2)} \cdot \mathbf{C}_{i(2)}^T)$
     Set $\mathbf{U}_{k+1}^{(2)} = \mathbf{U}^{(2)}$.
     ...

   - Maximize $S' = \sum_{i=1}^{M} \| \mathcal{C}_i \times_n \mathbf{U}^{(n)^T} \|^2$, $\mathcal{C}_i = \mathcal{A}_i \times_1 \mathbf{U}_{k+1}^{(1)^T} \times ... \times_{n-1} \mathbf{U}_{k+1}^{(n-1)^T} \times_{n+1} \mathbf{U}_k^{(n+1)^T} \times ... \times_N \mathbf{U}_k^{(N)^T}$
     Solution: $\mathbf{U}^{(n)}$ whose columns are determined as the first J_n leading eigenvectors of $\sum_{i=1}^{M} (\mathbf{C}_{i(n)} \cdot \mathbf{C}_{i(n)}^T)$
     Set $\mathbf{U}_{k+1}^{(n)} = \mathbf{U}^{(n)}$.
     ...

   - Maximize $S' = \sum_{i=1}^{M} \| \mathcal{C}_i \times_N \mathbf{U}^{(N)^T} \|^2$, $\mathcal{C}_i = \mathcal{A}_i \times_1 \mathbf{U}_{k+1}^{(1)^T} \times ... \times_{N-1} \mathbf{U}_{k+1}^{(N-1)^T}$
     Solution: $\mathbf{U}^{(N)}$ whose columns are determined as the first J_N leading eigenvectors of $\sum_{i=1}^{M} (\mathbf{C}_{i(N)} \cdot \mathbf{C}_{i(N)}^T)$
     Set $\mathbf{U}_{k+1}^{(N)} = \mathbf{U}^{(N)}$.

   $k = k + 1$

3. Set $\mathbf{U}_{opt}^{(1)} = \mathbf{U}_k^{(1)}$, $\mathbf{U}_{opt}^{(2)} = \mathbf{U}_k^{(2)}$, ..., $\mathbf{U}_{opt}^{(N)} = \mathbf{U}_k^{(N)}$.

$\mathbb{R}^{I_1 \times I_2 \times \ldots \times I_N}, i = 1, 2, \ldots, M$, I want to find another series basis which have mutual independence and greater discrimination to represent the original tensors. Each tensor $\mathcal{A}_i$ is represented by basis: $\mathcal{A}_i = \sum_{j=1} c_{i,j} \cdot \mathcal{B}_j$. Here the tensors $\mathcal{B}_j$ is basis which has the same size as the input tensor, and the scalar $c_{i,j}$ is the coefficient of the tensor $\mathcal{A}_i$. Figure 3.6 illustrates the representation of one original tensor using a series of basis.

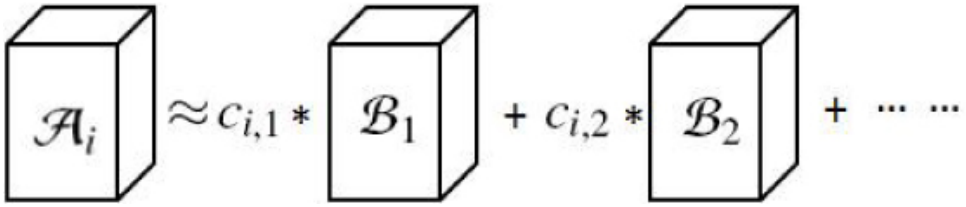

Figure 3.6: Example of representing the third order tensor using a series of basis.

In matematics, the problem to get the compact representation can be formulated as the optimization equation:

$$(\mathcal{B}_1, \mathcal{B}_2, ...) = \arg\min \sum_{i=1}^{M} \|\mathcal{A}_i - \sum_{j=1} c_{i,j} * \mathcal{B}_j\|. \tag{3.7}$$

Since the objective function is multi-quadratic, there is no closed-form solution for this optimization. In addition, the number of basis is unfixed, hence the optimization procedure is sensitive to initial estimation and easy to converge to local minima. To address such problems, I develop an algorithm: linear tensor coding algorithm (LTC). There are two important components in my algorithms: one is a local convergence to find optimized basis $\mathcal{B}_j$ and the other is a global convergence to find the number of bases.

In the local parts, GND-PCA method [9,11] is applied for calculation of each bases. The purpose of GND-PCA is to find a series of optimal mode-submatrices $\mathbf{U}^{(i)}, 1 \leq i \leq N$ by minimizing the cost function Eq. 3.8. $\mathcal{C}_i$ is the core tensors. The cost function is defined as a mean square error between

the original tensor and the reconstructed tensor.

$$S = \sum_{i=1}^{M} \parallel \mathcal{A}_i - \mathcal{C}_i \times_1 \mathbf{U}^{(1)} \times_2 \mathbf{U}^{(2)} \times_3 \mathbf{U}^{(3)} \times ... \times_N \mathbf{U}^{(N)} \parallel^2 \tag{3.8}$$

Theorem 3.3.1. *Given fixed N matrices $\mathbf{U}^{(n)}$, the tensors $\mathcal{C}_i$ that minimize the cost function, Eq. 3.6, are given by*

$$\mathcal{C}_i = \mathcal{A}_i \times_1 \mathbf{U}^{(1)^T} \times_2 \mathbf{U}^{(2)^T} \times ... \times_N \mathbf{U}^{(N)^T}. \tag{3.9}$$

The proof of Theorem 3.3.1 is simple, so it is omitted. With the help of Theorem 3.3.1, Theorem 3.3.2 can be obtained.

Theorem 3.3.2. *If the tensors $\mathcal{C}_i$ are chosen as $\mathcal{C}_i = \mathcal{A}_i \times_1 \mathbf{U}^{(1)^T} \times_2 \mathbf{U}^{(2)^T} \times ... \times_N \mathbf{U}^{(N)^T}$, minimization of the cost function Eq. 3.8 is equal to maximization of the following cost function S', where*

$$S' = \sum_{i=1}^{M} \parallel \mathcal{A}_i \times_1 \mathbf{U}^{(1)^T} \times_2 \mathbf{U}^{(2)^T} \times ... \times_N \mathbf{U}^{(N)^T} \parallel^2. \tag{3.10}$$

There is no close-form solution to simultaneously resolve the matrices $\mathbf{U}^{(n)}$ for the cost function S'; however the explicit solution can be obtained by using an iterative algorithm.

The first row vector $\mathbf{u}_1^{(i)}$ of each $\mathbf{U}^{(i)}$ is the eigenvector with the largest eigenvalue in the corresponding mode. I choose $\mathbf{u}_1^{(i)}, 1 \leq i \leq N$ as a set of initial estimations and the first tensor-formed base is calculated by Eq. 3.12.

$$\mathcal{B}_1 = \mathbf{u}_1^{(1)} \otimes \mathbf{u}_1^{(2)} \otimes ... \otimes \mathbf{u}_1^{(N)}. \tag{3.11}$$

$$I = max(\mathcal{B}_1) = max(\mathbf{u}_1^{(1)} \otimes \mathbf{u}_1^{(2)} \otimes \mathbf{u}_1^{(3)} \otimes ... \otimes \mathbf{u}_1^{(N)}). \tag{3.12}$$

For each training tensor, the parameters corresponding to the first base are calculated by Eq. 3.13.

$$c_{i,1} = \mathcal{A}_i \times_1 \mathbf{u}_1^{(1)^T} \times_2 \mathbf{u}_1^{(2)^T} \times ... \times_N \mathbf{u}_1^{(N)^T}. \tag{3.13}$$

After obtaining the first base, the residual parts of each training tensor was calculated: $\bar{\mathcal{A}}_i = \mathcal{A}_i - c_{i,1} * \mathcal{B}_1$. The residual parts are used to instead of $\mathcal{A}_i$. The local convergence was used to get

the bases one by one. The process to find a series of bases is like a greedy approach to approximate the original tensors.

A global convergence was worked to find a number of bases. The global process could be ended when the sum of norms of the residual tensors is below some threshold. Recalling Eq. 3.7, a threshold r was assigned. The process ends after find J basis when the sum of norms of the residual tensors is below r , as shown in Eq. 3.14. Then each tensor data is represented with a group of coefficients with the benefit of the obtained basis.

$$norm(\sum_{i=1}^{M} \|\mathcal{A}_i - \sum_{j=1}^{J} c_{i,j} * \mathcal{B}_j\|) \leq r. \tag{3.14}$$

Algorithm 2 shows iteration algorithm of LTC.

3.4 Experimental Results

The proposed method was evaluated by using a liver database. In this database, there are 10 normal healthy ones and 10 abnormal ones which with the tumor in it. Because intensity of tumor is different from that of liver, thus in the work, I used statistical texture analysis for diagnosis. The size of each sample is $256 \times 256 \times 79$. The flow chart of my experiment is shown in Figure.3.7. In this figure, the normalized volume is the data which after the preprocessing.

In order to remove shape variations, I applied a non-rigid transformation based on mathematical forms for morphing all the datasets to similar shape. Any nonrigid registration technique can be described by three components: a transformation which relates the target and source images, a similarity measure which measures the similarity between target and source image, and an optimization which determines the optimal transformation parameters as a function of the similarity. Additionally, I did not need to assume the physical parameters, which are difficult to guess in practice.Hence, I adopted the mathematical nonrigid transformation in my research. For the detailed process, please refer to

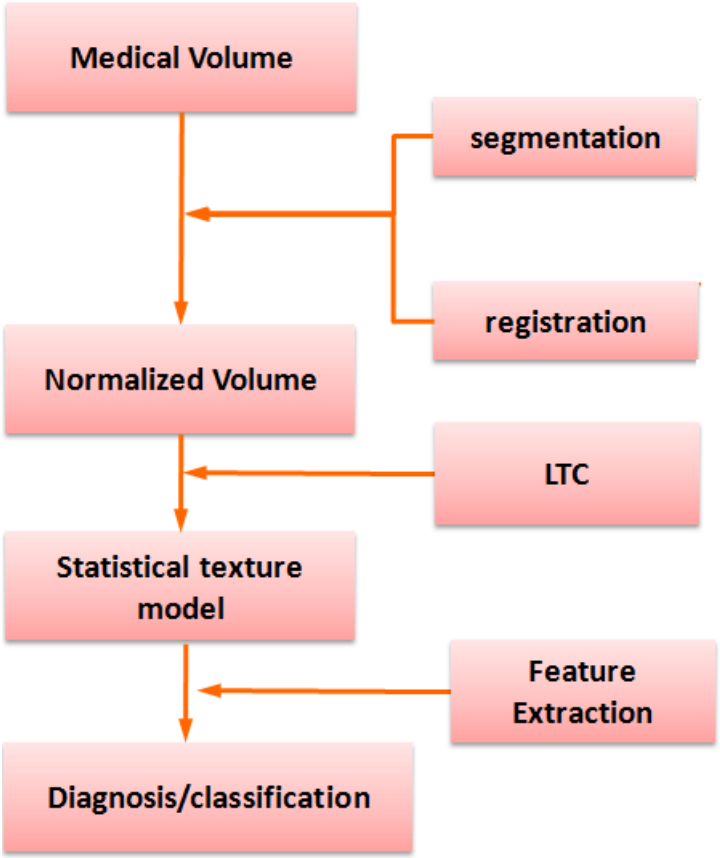

Figure 3.7: The flow chart of my experiment.

[11].

Figure 3.8 shows some original data and morphed data respectively. The first column is original data and the second column is morphed data. The first row is one samples of the normal ones, the second row is one sample of the abnormal ones. We can see that the shapes after registration are very similar, so it meant that the effect of shape can be reduced as much as possible.

Because I wanted to build a statistical texture model, each data can be represented by Eq.3.15:

$$\mathcal{A}_i = \mathcal{M} + \sum_{k=1}^{K} c_{i,k} * \mathcal{B}_k. \tag{3.15}$$

Here $\mathcal{M}$ is the mean texture and $c_{i,k}$ are the coefficients. Supposing the coefficients $c_{i,k}$ follow Gaussian distribution, I can estimate the mean m_k and derivation λ_k^2.

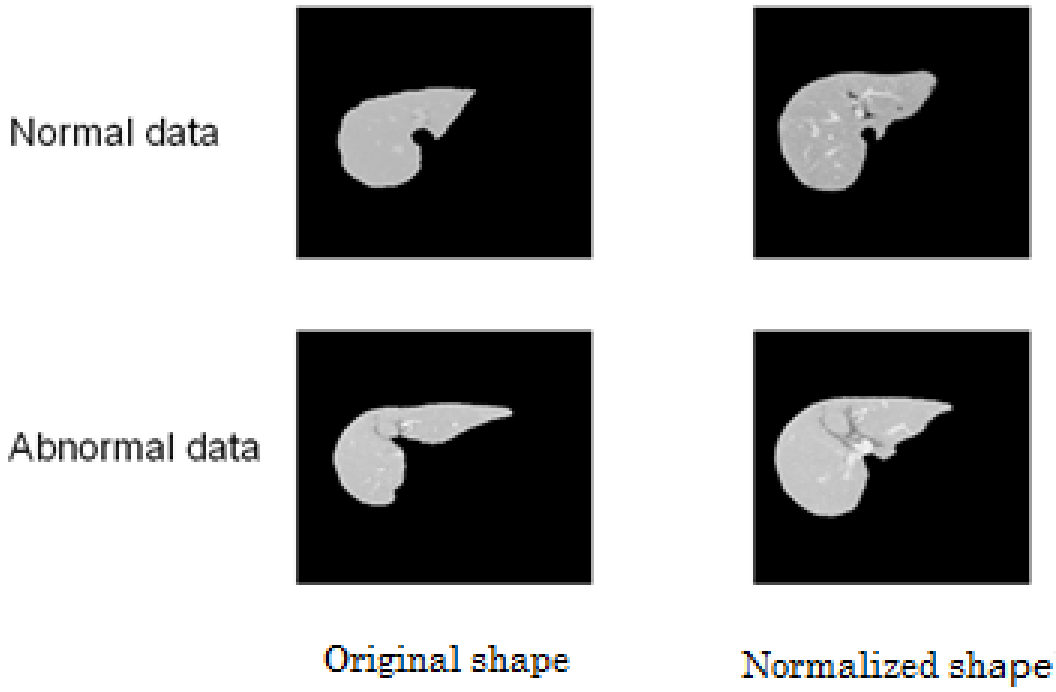

Figure 3.8: Original data and morphed data respectively. The first column is original data and the second column is morphed data.

By adjusting the parameter, I can construct a novel ensemble by Eq.3.16"

$$\widetilde{\mathcal{A}} = \mathcal{M} + \widetilde{c_k} * \mathcal{B}_k. \tag{3.16}$$

Here $\widetilde{c_k}$ is adjusted coefficient, $-2\lambda_k \leqslant \widetilde{c_k} \leqslant 2\lambda_k$. Figure 3.9 illustrates the slices of novel ensembles described by the first five bases, respectively. They demonstrate that: while changing the value of first coefficients from $-1.5\lambda_1$ to $1.5\lambda_1$, the intensity of left part has obviously changed, and the second basis mainly effect on the right corner of the slice. Furthermore, Figure 3.10 shows the fist twenty basis, it illustrates that different basis can effect on different parts. Thus I can change the local intensity of slice through change the coefficient of basis.

Figure 3.11 shows the values of coefficient when the number of basis is different for LTC. It illustrates that the first several values are obviously larger than the other ones. Because of this, the volume can be reconstructed by less basis than GND-PCA.

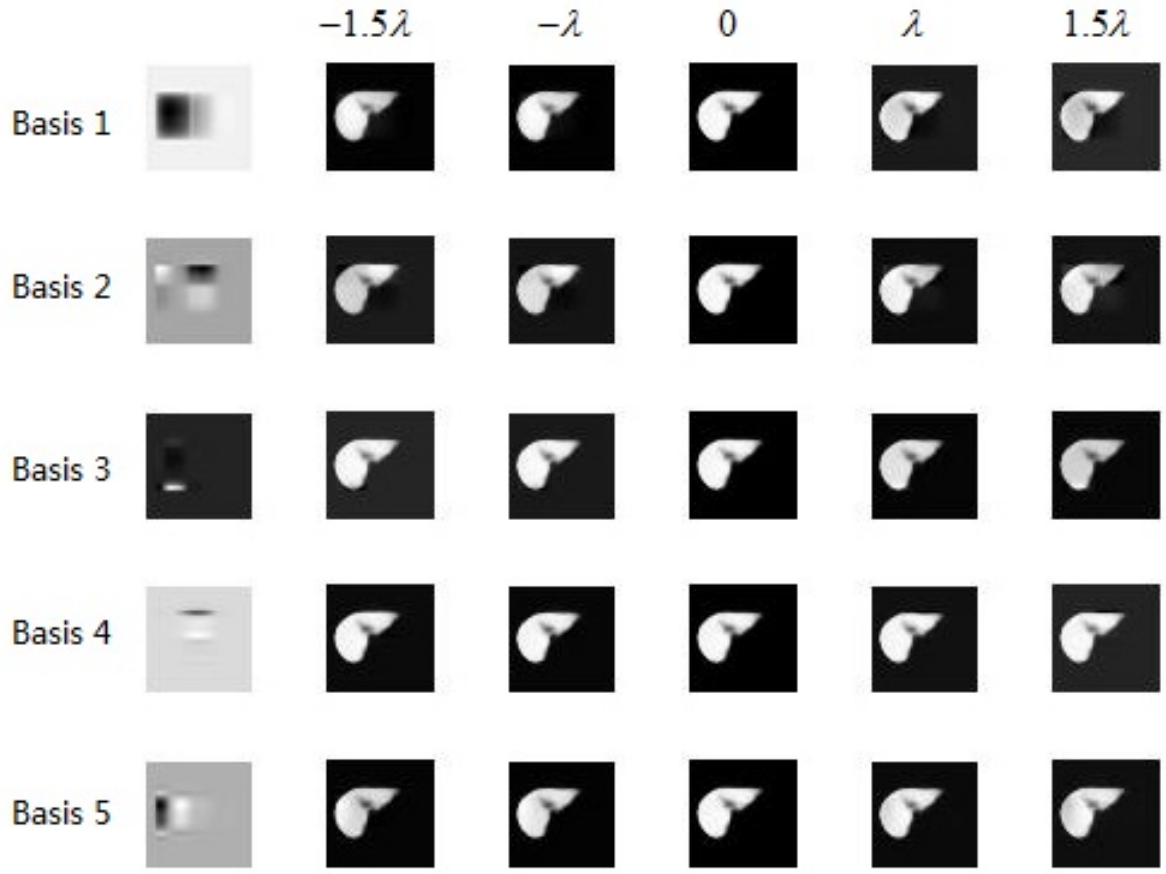

Figure 3.9: The slices of novel ensembles described by the first five bases, respectively. It changes the value of coefficients from $-1.5\lambda_1$ to $1.5\lambda_1$ of each basis.

I evaluated the model generalization by reconstructing a test volume, which is not included in the training samples. Thus leave-one out method (19 samples for training the basis, and the last one is used as test for reconstruction) was adopted. For each test volume, I firstly calculated the coefficients of each basis as Eq.3.17 and Eq.3.18:

$$\mathcal{A}' = \mathcal{A}_{test} - \mathcal{M} - \sum_{i=1}^{k-1} c_{test,i}\mathcal{B}_i \tag{3.17}$$

$$c_{i,k} = \mathcal{A}' \times_1 \mathbf{u}_k^{(1)^T} \times_2 \mathbf{u}_k^{(2)^T} \times \ldots \times_N \mathbf{u}_k^{(N)^T}. \tag{3.18}$$

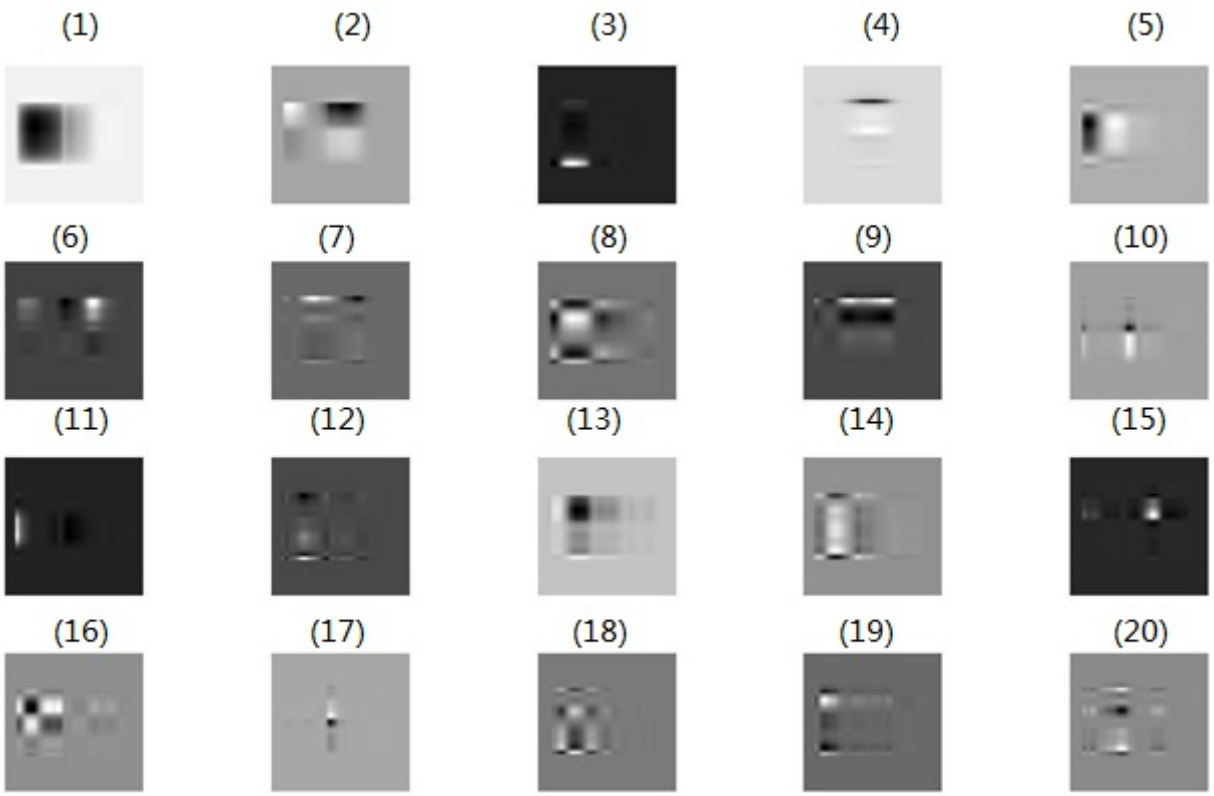

Figure 3.10: The first twenty basis. It illustrates that each basis can represent a local feature.

And then I chose the first k' basis for reconstruction:

$$\mathcal{A}_{reconstruction} = \mathcal{M} + \sum_{i=1}^{k'} c_{test,i}\mathcal{B}_i \tag{3.19}$$

Here $\mathcal{A}'$ represents the residual part,$\mathcal{A}$ is the test volume and $\mathcal{A}_{reconstruction}$ is the reconstruction result. The correlation between the reconstructed volume and the original volume is used as a measure of the reconstruction (generalization). The value of correlation is between 0 and 1. The more similar the two volumes are, the larger its value is. Figure 3.12 shows the graph of normalized correlation between original volume and reconstructed volume for different number of basis. The result in Figure 3.12 illustrates that the original volume can be better reconstructed by LTC when the number of basis is the same as GND-PCA.

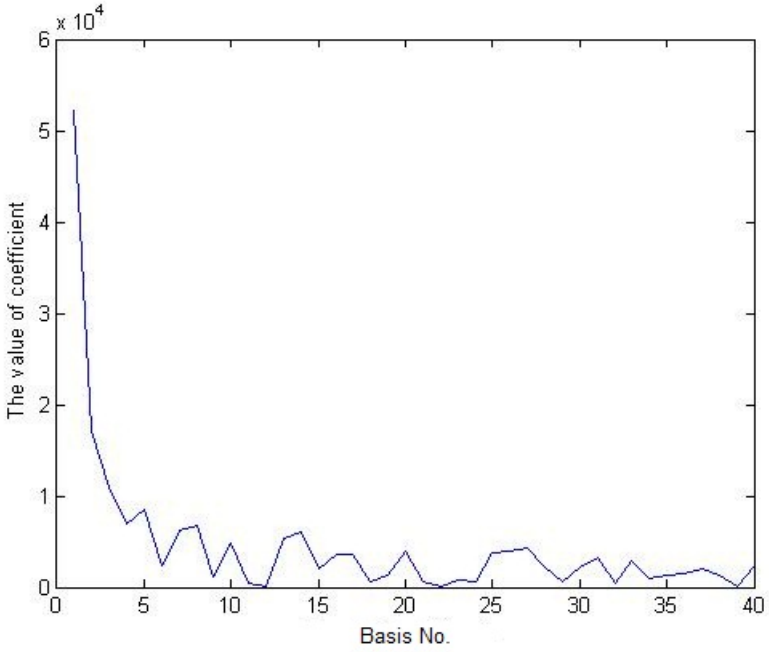

Figure 3.11: The coefficient of each basis for LTC.

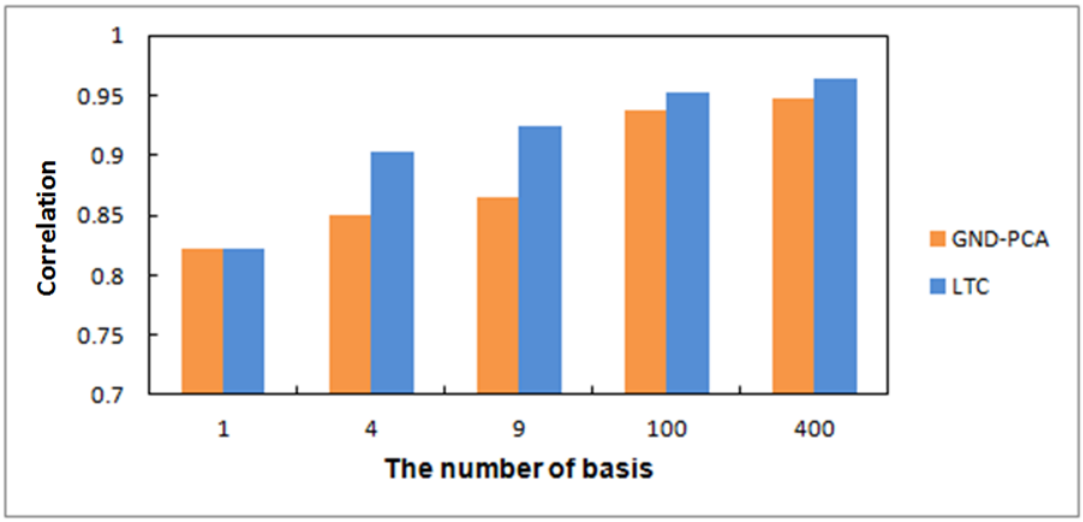

Figure 3.12: Reconstruction accuracy vs. number of basis.

For classification, the coefficients were used as the feature. SVM and KNN are utilized as classifiers respectively. For LTC, I trained 1200 basis, and for GND-PCA, the size of core-tensor is $20 \times 20 \times 3$. And I used Leave-one-out method to do the classification. Figure 3.13 shows the distribution of coefficients of the first four basis of LTC. The blue ones are the normal livers, and the red ones are

abnormal livers. The number in the bracket is the correlation coefficients which is calculated by Eq.3.20

$$Correlation_k = \frac{\sum_{i=1}^{n} c_{ik} l_i}{\sqrt{\sum_{i=1}^{n} {c_{ik}}^2 \sum_{i=1}^{n} {l_i}^2}} \tag{3.20}$$

Here, n is the number of samples, c_{ik} is the coefficient of one fixed basis of LTC and $l_i \in \{-1, 1\}, 1 \leq i \leq n$ is the label of the samples. In my experiments, -1 represents normal liver, and 1 represents abnormal liver. For each basis, I can get a correlation coefficient. From the correlation coefficients in Figure 3.13, it illustrates that it is difficult for classification if using these basis because the correlation coefficients are so small. Thus, I firstly chose the basis using the correlation coefficients. While GND-PCA cannot choose basis because the core tensor is directly used for classification. Figure 3.14 is the coefficients of the first four basis chosen through correlation coefficients.The blue ones are the normal livers, and the red ones are abnormal livers. The first number in the bracket is the position of basis in the original basis set and the second number in the bracket is the correlation coefficient of corresponding basis.

Table 3.1 is the classification accuracy using different classifiers. Before choosing basis, I used all the basis for classification. It could be seen that the classification accuracy of LTC and GND-PCA are both bad. Then I chose the first one hundred basis which has greater correlation coefficients for classification. The classification accuracy was obviously improved.

Table 3.1: The classification accuracy of GND-PCA and LTC.

	SVM	KNN
GND-PCA	7/20	10/20
LTC with all 1200 bases	7/20	9/20
LTC with 100 selected basis	19/20	19/20

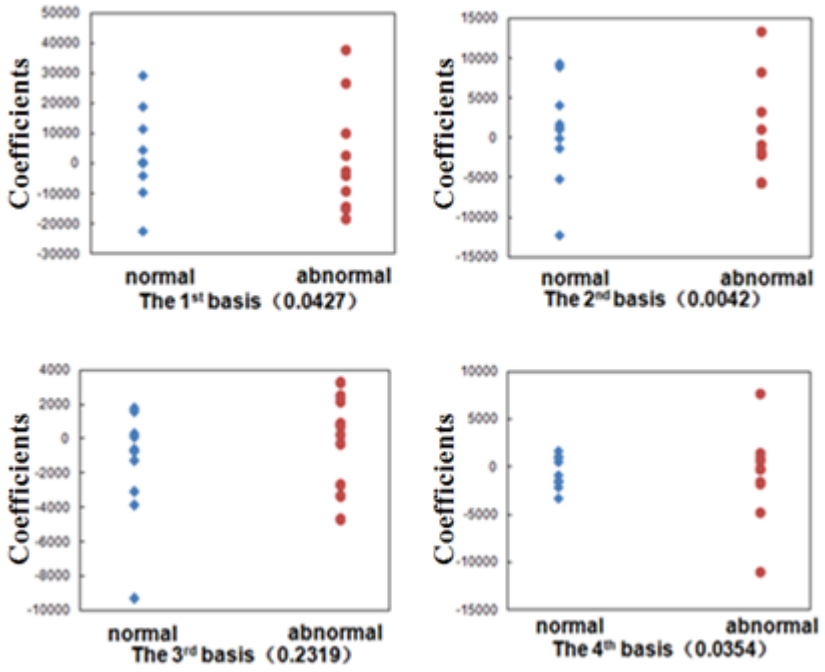

Figure 3.13: The distribution of coefficients of the first four basis. The blue one is represent the normal liver and the red one represent the abnormal liver.The number in the bracket is the correlation coefficients.

3.5 Conclusion

In this chapter, I proposed a statistical texture modeling method for medical volumes which was known as LTC. LTC is an extension of GND-PCA. 2. The medical volume such as the volume of the liver is treated as a third order tensor and it is represented by a linear combination of basis which has the same size as the tensor. Each basis are mutual independence and more discriminate than GND-PCA. In my experiments, I compared both reconstructed results and classification results of LTC and GND-PCA. As for reconstruction results, the performance of LTC is superior to that of GND-PCA. Additionally, in the classification part, I firstly chose the distinctive basis through the correlation between category labels and the coefficients of basis of LTC. And then I used the selected basis for classification. The classification accuracy was significantly improved by the use of selected distinctive basis. Future work will involve testing my method with more data sets for classification

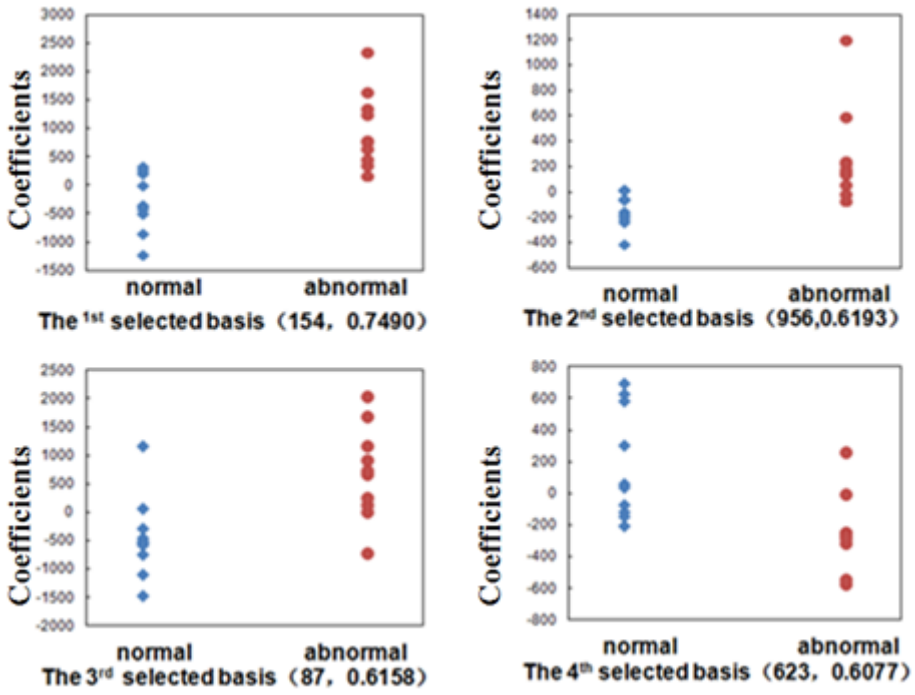

Figure 3.14: The distribution of coefficients of the first four basis chosen through correlation coefficients.The blue ones are the normal livers, and the red ones are abnormal livers. The first number in the bracket is the position of basis in the original basis set and the second number in the bracket is the correlation coefficient.

and using my method in practical applications.

Algorithm 2 Iteration algorithm of LTC.

IN: a series of N-th order tensors, $\mathcal{A}_i \in \mathbb{R}^{I_1 \times\ I_2 \times ... \times I_N}, i = 1, 2, ..., M$. Define N Matrices $\mathbf{U}_{opt}^{(n)} \in \mathbb{R}^{I_n \times J_n}$ $(J_n = 1, n = 1, 2, ..., N)$ with orthogonal column vectors.
OUT: S Rank-1 basis tensor $\mathcal{B}_s$,$s \leq S$ S depends on convergence.
Iterate for s until convergence

1. Initial values: $\mathcal{A}_i = \mathcal{A}_i - \mathcal{A}_i^{Rec_s}$, define $\mathcal{A}_i^{Rec_1} = 0$.

2. (a) Initial values: $k = 0$ and $\mathbf{U}_0^{(n)}$ whose columns are determined as the first J_n leading eigenvectors of the matrices $\sum_{i=1}^{M} (\mathbf{A}_{i(n)} \cdot \mathbf{A}_{i(n)}^T)$.

   (b) Iterate for k until convergence

   - Maximize $S' = \sum_{i=1}^{M} \| \mathcal{C}_i \times_1 \mathbf{U}^{(1)^T} \|^2$, $\mathcal{C}_i = \mathcal{A}_i \times_2 \mathbf{U}_k^{(2)^T} \times ... \times_N \mathbf{U}_k^{(N)^T}$
     Solution: $\mathbf{U}^{(1)}$ whose columns are determined as the first J_1 leading eigenvectors of $\sum_{i=1}^{M} (\mathbf{C}_{i(1)} \cdot \mathbf{C}_{i(1)}^T)$
     Set $\mathbf{U}_{k+1}^{(1)} = \mathbf{U}^{(1)}$.

   - Maximize $S' = \sum_{i=1}^{M} \| \mathcal{C}_i \times_2 \mathbf{U}^{(2)^T} \|^2$, $\mathcal{C}_i = \mathcal{A}_i \times_1 \mathbf{U}_{k+1}^{(1)^T} \times_3 \mathbf{U}_k^{(3)^T} \times ... \times_N \mathbf{U}_k^{(N)^T}$
     Solution: $\mathbf{U}^{(2)}$ whose columns are determined as the first J_2 leading eigenvectors of $\sum_{i=1}^{M} (\mathbf{C}_{i(2)} \cdot \mathbf{C}_{i(2)}^T)$
     Set $\mathbf{U}_{k+1}^{(2)} = \mathbf{U}^{(2)}$.
     ...

   - Maximize $S' = \sum_{i=1}^{M} \| \mathcal{C}_i \times_n \mathbf{U}^{(n)^T} \|^2$, $\mathcal{C}_i = \mathcal{A}_i \times_1 \mathbf{U}_{k+1}^{(1)^T} \times ... \times_{n-1} \mathbf{U}_{k+1}^{(n-1)^T} \times_{n+1} \mathbf{U}_k^{(n+1)^T} \times ... \times_N \mathbf{U}_k^{(N)^T}$
     Solution: $\mathbf{U}^{(n)}$ whose columns are determined as the first J_n leading eigenvectors of $\sum_{i=1}^{M} (\mathbf{C}_{i(n)} \cdot \mathbf{C}_{i(n)}^T)$
     Set $\mathbf{U}_{k+1}^{(n)} = \mathbf{U}^{(n)}$.
     ...

   - Maximize $S' = \sum_{i=1}^{M} \| \mathcal{C}_i \times_N \mathbf{U}^{(N)^T} \|^2$, $\mathcal{C}_i = \mathcal{A}_i \times_1 \mathbf{U}_{k+1}^{(1)^T} \times ... \times_{N-1} \mathbf{U}_{k+1}^{(N-1)^T}$
     Solution: $\mathbf{U}^{(N)}$ whose columns are determined as the first J_N leading eigenvectors of $\sum_{i=1}^{M} (\mathbf{C}_{i(N)} \cdot \mathbf{C}_{i(N)}^T)$
     Set $\mathbf{U}_{k+1}^{(N)} = \mathbf{U}^{(N)}$.

   $k = k + 1$

   (c) Set $\mathbf{U}_{opt}^{(1)} = \mathbf{U}_k^{(1)}$, $\mathbf{U}_{opt}^{(2)} = \mathbf{U}_k^{(2)}$, ..., $\mathbf{U}_{opt}^{(N)} = \mathbf{U}_k^{(N)}$.

3. Size of $\mathbf{U}_{opt}^{(i)}$ is $I_i \times 1$, each basis $\mathcal{B}_s = \mathbf{U}_{opt}^{(1)} \otimes \mathbf{U}_{opt}^{(2)} \otimes ... \otimes \mathbf{U}_{opt}^{(N)}$.

4. For each data, coefficient on this basis $c_{i,s} = \mathcal{A}_i \times_1 \mathbf{U}_k^{(1)^T} \times_2 \mathbf{U}_k^{(2)^T} \times ... \times_N \mathbf{U}_k^{(N)^T}$.

5. For each data $\mathcal{A}_i^{Rec_s} = c_{i,s} \cdot \mathcal{B}_s$.

Bibliography

[1] F.H. Netterem, Atlas of Human Anatomy, *WB Saunders*, 2006.

[2] K.H. Hohne, B. Pflesser, A. Pommert et al., A new representation of knowledge concerning human anatomy and function, *Nature Medicine*, 1(6):506-511, 2006.

[3] T.F. Cootes, C.J. Taylor, D.H. Cooper, J. Graham, Active shape models-their training and application, *Computer Vision and Image Understanding*, 61(1):38-59, 1995.

[4] H. Huang, F. Makedon, R. McColl, High dimensional statistical shape model for medical image analysis, *IEEE International Symposium on Biomedical Imaging:From Nano to Macro (ISBI ¡¯08)*, 1541-1544, May, 2008.

[5] H.C. Van Assen, M.G. Danilouchkine, F. Behloul et al., Cardiac LV segmentation using a 3D active shape model driven by fuzzy inference, *Proc. the 6th International Conference on Medical Image Computing and Computer-Assisted Intervention (MICCAI'03)*, 2878:533-540, 2003.

[6] M.R. Kaus, J. von Berg, J. Weese et al., Automated segmentation of the left ventricle in cardiac MRI, *Medical Image Analysis*, 8(3):245-254, 2004.

[7] T.F. Cootes, G.J. Edwards, C.J. Taylor, Active appearance models, *IEEE Transactions on Pattern Analysis and Machine Intelligence*, 23(3):681-685, 2001.

[8] S. Mitchell, B. Lelieveldt, R. van der Geest et al., Segmentation of cardiac mr images: An active appearance model approach, *SPIE Medical Imaging*, Feb, 2000.

[9] Y.W. Chen, M. Uetani, S. Kohara et. al., Application of statistical shape model of the liver in classification of cirrhosis, *International Journal of Digital Content Technology and its Applications*, 2013(in press).

[10] R. Xu, Y.W. Chen, Generalized N-dimensional principal component analysis (GND-PCA) and its application on construction of statistical appearance models for medical volumes with fewer samples, *Neurocomputing*, 72:2276-2287, June, 2009.

[11] X .Qiao and Y.W. Chen, A Statistical Texture Model of the Liver Based on Generalized N-Dimensional Principal Component Analysis (GND-PCA) and 3D Shape Normalization, *International Journal of Biomedical Imaging*, 2011.

[12] D.L. Lieven, D.M. Bart, V.Joseph, A multilinear singular value decomposition, *SIAM Journal of Matrix Analysis and Application*, 4(21):1253-1278, 2001.

[13] X. Qiao, T. Lgarashi, K. Nakao, Y.W. Chen, Linear Tensor Coding for Efficient Representation of Multi-dimensional Data, *MIRU 2010*, 2010.

[14] X. Qiao, X.T. Su, X.H. Han, Y.W. Chen, A New Linear Coding Algorithm for Efficient Multi-dimensional Data Representation without Data Expansion, *Proc. of 2012 International Conference on New Trends in Information Science, Service Science and Data Mining (ISSDM2012), Taiwan*, 475-478, 2012.

Chapter 4

Statistical Analysis of Shape Based on SLRMD

In the field of computational techniques for medical images, shape analysis is used to study the geometrical properties of the structures obtained using various imaging modalities. Shape analysis has recently become of increasing interest to the medical community due to its potential to precisely locate morphological changes between different populations of structures; for example, it can be used to differentiate the changes between healthy and pathological tissues.

Statistical analysis is one the most common ways for exploring robust shape features and for understanding shape information. For more accurate analyses, it is necessary to use a registration method for the shapes. Because surface points are used for SSM, points-based registration methods are used in this thesis. Compared with registration methods based on voxel similarity, assuming that there are a sufficiently large number of points, points-based registration methods can be used for more complex transformations than can be used with methods based on voxel similarity. Also, since the dimensionality of the surface points is lower than that of the image itself, this facilitates calculations. However, for various reasons, such as pathological changes or inaccurate segmentation, the accuracy of the registration may be reduced.

Meanwhile, SSMs based on PCA are widely used. Due to some limitations of PCA, however, this

method cannot be used for all applications. First, the PCA cost function does not include a term for the noise, and thus the basis or eigenspace calculated by PCA will be affected by noise. Furthermore, it is difficult to clearly explain the constructed SSMs in terms of which one manifests the global variations due to the differences between subjects and which one expresses the local deformations due to the progression of diseases.

In this chapter, a local shape analysis method is proposed; this method is based on sparse and low-rank matrix decomposition (SLRMD), which is able to identify and separate the local shape deformations. The following three objectives are thereby achieved: (a) a robust shape-based registration method is proposed that uses the local shape analysis to preprocess the image in order to remove any local deformations and noise; (b) an accurate computer-aided diagnosis (CAD) method for cirrhotic livers is developed that is based on the local shape analysis instead of on PCA; (c) an incremental SLRMD is proposed for on-line medical image diagnosis. SLRMD will be introduced in the next section.

4.1 Sparse and Low Rank Matrix Decomposition (SLRMD)

PCA is arguably the most widely used statistical tool for data analysis and dimensionality reduction today. However, in general, training data may contain undesirable artifacts due to occlusion, illumination, image noise. Thus Sparse and Low Rank Matrix Decomposition(SLRMD) was proposed that can be used to construct low-dimensional linear-subspace representations from this noisy data. The cost function of SLRMD can be wrote as:

$$\min_{\mathbf{A},\mathbf{E}} rank(\mathbf{A}) + \lambda \|\mathbf{E}\|_0,\ \mathbf{D} = \mathbf{A} + \mathbf{E} \tag{4.1}$$

Here $\lambda > 0$ is a parameter that determines the trade-off between the rank of the solution and the

sparsity of the error, $\mathbf{A}$ is a low rank matrix, and $\mathbf{E}$ is sparse matrix which represents the noise. In some paper, SLRMD was also named as Robust PCA(RPCA).

The optimization problem of Eq.4.1 is not directly tractable. A major difficulty is the non-convexity of the matrix rank and the L0-norm: in the worst case, minimization of these functions is extremely difficult (NP-hard and even difficult to approximate). Recently, Wright et al. [1] showed that the answer holds true with rather broad conditions, that is, as long as the error matrix $\mathbf{E}$ is sufficiently sparse (relative to the rank of $\mathbf{D}$). The low-rank matrix $\mathbf{A}$ can be recovered exactly from $\mathbf{D} = \mathbf{A} + \mathbf{E}$ by solving the following convex optimization problem:

$$\min_{\mathbf{A},\mathbf{E}} \|\mathbf{A}\|_* + \lambda\|\mathbf{E}\|_1, \quad subject\ to\ \mathbf{D} = \mathbf{A} + \mathbf{E} \tag{4.2}$$

Here $\|\mathbf{A}\|_*$ is nuclear norm which equals to $trace(\sqrt{\mathbf{A}^*\mathbf{A}})$, and A* is conjugate transpose of $\mathbf{A}$. To solve this constrained optimization problem, many algorithms have been proposed, including the accelerated proximal gradient method [2], the augmented Lagrange multiplier (ALM) method [3], and the alternating direction method (ADM) [4]. In this paper, we applied the ALM method, which will be briefly reviewed below.

The general ALM method was introduced for solving constrained optimization problems of the following kind:

$$\min f(\mathbf{x}), \quad subject\ to\ \ h_i(\mathbf{x}) = 0, \forall i \in I \tag{4.3}$$

Compared to the general Lagrange multiplier, the ALM adds a quadratic penalty term that is defined as:

$$L(\mathbf{x}, \beta, \mu) = f(\mathbf{x}) + \frac{\mu}{2}\sum_{i\in I} h_i(\mathbf{x})^2 + \langle \beta, h_i(\mathbf{x})\rangle \tag{4.4}$$

where $\boldsymbol{\beta}$ is the Lagrange multiplier and μ is a positive scalar. The variable β_i is updated according

to the following rule: $\beta_i \leftarrow \beta_i + \mu h_i(\mathbf{x})$. However, for sparse and low-rank matrix decomposition, the argument of the function is a matrix, so the ALM method becomes

$$\begin{aligned} &\mathbf{X} = (\mathbf{A}, \mathbf{E}), f(\mathbf{X}) = \|\mathbf{A}\|_* + \lambda\|\mathbf{E}\|_1, \\ &and \;\; \mathbf{H}(\mathbf{X}) = \mathbf{D} - \mathbf{A} - \mathbf{E} \end{aligned} \tag{4.5}$$

The augmented Lagrangian function is:

$$\begin{aligned} \mathbf{L}(\mathbf{A}, \mathbf{E}, \mathbf{B}, \mu) \doteq &\| \mathbf{A}\|_* + \lambda \| \mathbf{E}\|_1 + \tfrac{\mu}{2} \| \mathbf{D} - \mathbf{A} - \mathbf{E} \|_{\mathbf{F}}^{\mathbf{2}} \\ &+ \langle \mathbf{B}, \mathbf{D} - \mathbf{A} - \mathbf{E} \rangle \end{aligned} \tag{4.6}$$

where $\langle \mathbf{P}, \mathbf{Q} \rangle = tr(\mathbf{P}^{\mathbf{T}}\mathbf{Q})$, and $\mathbf{B}$ is the Lagrange multiplier. The ALM method for solving the sparse and low-rank decomposition is called the exact ALM (EALM) method, in reference [5]. The EALM method has been proven to have a pleasing Q-linear convergence speed. A slight improvement over the EALM leads to the inexact ALM (IALM) method, which was used in this thesis, the flowchart of the IALM is shown in Figure 4.1.

The function $J(\mathbf{D})$ in the initial part of Figure 4.1 is $J(\mathbf{D}) = \max(\|\mathbf{D}\|_{\mathbf{2}}, \lambda^{-\mathbf{1}}\|\mathbf{D}\|_\infty)$, and $\|\bullet\|_\infty$ is the maximum absolute of the matrix entries. The IALM method converges almost as quickly as does the EALM method, but the required number of singular value decompositions (SVDs) is significantly less. Meanwhile in this paper, we set hyper-parameter $\lambda = 1/\sqrt{N}$, where N is the dimension of sample. In reference[6], Cands et al proved this hyper-parameter is the best one for this problem. In the experimental part, this hyper-parameter was adopted for all experiments.

Figure 4.2 shows an example of SLRMD. The first column is the original images of which have occlusion. The second and third columns are low rank images and sparse error images, respectively. We can see that the occlusion can be removed and the images can be recovered. Due to this reason, in this work, I applied SLRMD for two applications in CAD systems which was shown in Figure 4.3.

Algorithm: Sparse and Low Rand Matrix Decomposition via IALM

Input: Observation matrix $\mathbf{D} \in \mathbf{R}^{m \times n}, \lambda$

1: $\mathbf{B}_0 = \mathbf{D}/J(\mathbf{D})$; $\mathbf{E}_0 = 0; \mu_0 > 0; \rho > 1; k = 0.$

2: **while** not converged **do**

3: $(\mathbf{U}, \mathbf{S}, \mathbf{V}) = svd(\mathbf{D} - \mathbf{E}_k + \mu_k^{-1}\mathbf{B}_k);$

4: $\mathbf{A}_{k+1} = \mathbf{U}\mathbf{S}_{\mu_k^{-1}}\left[\mathbf{D} - \mathbf{A}_{k+1} + \mu_k^{-1}\mathbf{B}_k\right].$

6: $\mathbf{E}_{k+1} = \mathbf{S}_{\lambda\mu_k^{-1}}\left[\mathbf{D} - \mathbf{A}_{k+1} + \mu_k^{-1}\mathbf{B}_k\right].$

7: $\mathbf{B}_{k+1} = \mathbf{B}_k + \mu_k\left[\mathbf{D} - \mathbf{A}_{k+1} - \mathbf{E}_{k+1}\right].$

8: $\mu_{k+1} = \rho\mu_k$

9: $k \leftarrow k + 1.$

10: **end while**

Output: $(\mathbf{A}_k, \mathbf{E}_k).$

Figure 4.1: Flowchart of the inexact augmented Lagrange multiplier method.

In the next, I will introduce them in detail.

(a) Original Images **D**

(b) Low Ranks Images **A**

(c) Sparse error Images **E**

Figure 4.2: An example of SRLMD.

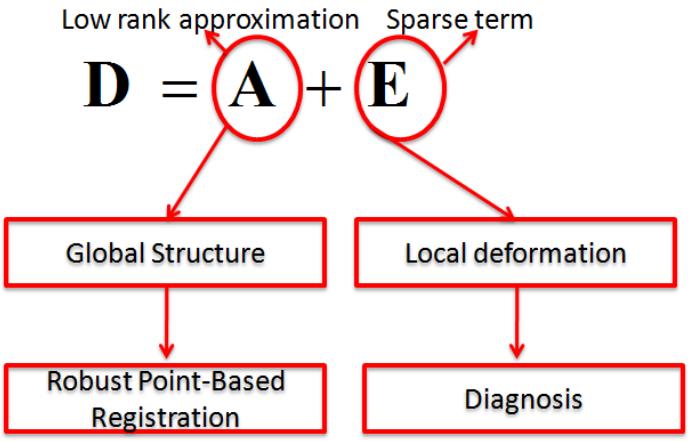

Figure 4.3: SLRMD for two applications in CAD systems.

4.2 Point-Based Registration based on SLRMD

To improve the registration accuracy of the GPA method, a new strategy that uses SLRMD is proposed, as was mentioned in the previous section. This strategy decomposes the input matrix into two matrices that can be represented as $\mathbf{D} = \mathbf{A} + \mathbf{E}$. Here $\mathbf{D}$ is the input matrix, each column of which gives the coordinates of one of the shapes in the set; $\mathbf{A}$ is a low-rank matrix, which means that the samples have similar parts; and $\mathbf{E}$ is a sparse matrix. In this work, I assumed that the noise or local deformations could be considered sparse relative to the entire shape. After excluding the noise and local deformations, the shape information should represent the structures that are globally similar. Thus, to increase the accuracy of the registration, the low-rank matrix $\mathbf{A}$ can be used to obtain the transformed parameters, from which the effects of the local deformations have been removed. Finally, these transformed parameters are used to improve the registration process.

4.2.1 Conventional Point-Based Registration Method

Image registration is a fundamental problem in image processing. Because the performance of registration directly affects further processing, it is a very important step. In this thesis, I focused on the

well-known point-based registration method which named as Generalized Procrustes Analysis(GPA). GPA is one of the most popular algorithms for aligning shapes with a common reference. The GPA algorithm lists as follows:

1. Choosing a temple as the mean shape.

2. Finding the corresponding transformations that match the remaining shapes with the mean shape.

3. Aligning all vectors to the mean shape. The cost function of point-based registration:

$$\min_{T} |\mathbf{x}_F - T(\mathbf{x}_M)|^2 \tag{4.7}$$

Here $\mathbf{x}_F$ represents the coordinates of surface points for the fixed image, which is not changed during the registration process. $\mathbf{x}_M$ represents the coordinates of surface points for the moving image, which is changed during the registration process.

4. Re-calculating the mean shape from the aligned shapes.

The Procrustes mean shape (also referred the Procrustes mean) is the most frequently used obtain an estimate of the mean shape. The Procrustes mean is given by:

$$\overline{\mathbf{x}} = \frac{1}{N}\sum_{i=1}^{N}\mathbf{x}_i \tag{4.8}$$

Where N is the number of shapes, x_i is the shape vector of each sample.

5. If the estimated mean has changed return to step 2 (Loop until converged).

The third step is the key of GPA. Alignment mainly includes three parts: translation, scaling and rotation. In the following I will briefly introduce the three steps.

Translation

Suppose $X_1 = [(x_1^1, y_1^1, z_1^1), (x_2^1, y_2^1, z_2^1), \ldots, (x_k^1, y_k^1, z_k^1)]$ and $X_2 = [(x_1^2, y_1^2, z_1^2), (x_2^2, y_2^2, z_2^2), \ldots, (x_k^2, y_k^2, z_k^2)]$ represent two different shape information, k is the number of points. Translational components can

be removed from an object by translating the object so that the mean of all the object's points lies at the origin as Eq.4.9.

$$\bar{x}^i = \frac{x_1^i + x_2^i + \cdots + x_k^i}{k}, \bar{y}^i = \frac{y_1^i + y_2^i + \cdots + y_k^i}{k}, \bar{z}^i = \frac{z_1^i + z_2^i + \cdots + z_k^i}{k} \tag{4.9}$$

Here i represents the number of different shapes. Then their mean is translated to the origin as: $[(x_1^i - \bar{x}^i, y_1^i - \bar{y}^i, z_1^i - \bar{z}^i); (x_2^i - \bar{x}^i, y_2^i - \bar{y}^i, z_2^i - \bar{z}^i); \ldots; (x_k^i - \bar{x}^i, y_k^i - \bar{y}^i, z_k^i - \bar{z}^i)]$.

Scaling

Likewise, the scale component can be removed by scaling the object so that the root mean square distance (RMSD) from the points to the translated origin is 1. This RMSD is a statistical measure of the object's scale or size as:

$$s = \sqrt{\frac{(x_1^i - \bar{x}^i)^2 + (y_1^i - \bar{y}^i)^2 + (z_1^i - \bar{z}^i)^2 + \cdots}{k}} \tag{4.10}$$

The scale becomes 1 when the point coordinates are divided by the object's initial scale:

$$[(x_1^i - \bar{x}^i, y_1^i - \bar{y}^i, z_1^i - \bar{z}^i)/s; (x_2^i - \bar{x}^i, y_2^i - \bar{y}^i, z_2^i - \bar{z}^i)/s; \ldots; (x_k^i - \bar{x}^i, y_k^i - \bar{y}^i, z_k^i - \bar{z}^i)/s] \tag{4.11}$$

Rotation

Suppose X_1' and X_2' are two shapes after translation and scaling. Here X_1' is used to provide a reference orientation. Fix the reference object and rotate X_2' around the origin, until finding an optimum angles of rotation. In the 3D space, there are three rotation directions: yaw, pitch, and roll. The angles of the rotation directions are represented by α, β, γ, respectively. In practice, SVD is used to calculated the rotation matrix as:

$$\mathbf{VU^T} = \begin{bmatrix} \cos\alpha\cos\gamma - \cos\beta\sin\alpha\sin\gamma & -\cos\beta\cos\gamma\sin\alpha - \cos\alpha\sin\gamma & \sin\alpha\sin\beta \\ \cos\gamma\sin\alpha + \cos\alpha\cos\beta\sin\gamma & \cos\alpha\cos\beta\cos\gamma - \sin\alpha\sin\gamma & -\cos\alpha\sin\beta \\ \sin\beta\sin\gamma & \cos\gamma\sin\beta & \cos\beta \end{bmatrix} \tag{4.12}$$

U and **V** are unitary orthogonal matrices whose columns give a linear basis of input data's columns and row, respectively. In here, the input data is $\mathrm{X_1}'^{\mathrm{T}}\mathrm{X_2}'$.

However, if the object had some noise or local deformation, the cost function of point-based registration will become as:

$$\min_{T} |\mathbf{x}_F - T(\mathbf{x}_M + \mathbf{e})|^2 \tag{4.13}$$

Here **e** represents local deformation or outlier. It will directly affect the final performance of GPA. Thus in this work, I proposed to use sparse and low rank matrix decomposition to improve the performance of GPA which will be introduced in the next section.

4.2.2 Proposed Method

As mentioned above, traditional GPA can be affected by noise or local deformations. Thus, my goal was to remove these effects. I assumed that if the shape information contained noise or local deformations, it could be decomposed into a low-rank matrix and a sparse matrix, and the low-rank matrix could be used to obtain transformed parameters that could be used to improve the registration.

Figure 4.4 shows a flow chat for the proposed method. In the first step, CT images of a liver are segmented manually. This segmentation is performed under the guidance of a physician in order to obtain accurate data on the shape of the liver. One sample is then chosen at random in order to serve as a reference; a rigid registration of the organ-to-organ volume is performed in order to normalize the data and to remove as much as possible of the positional and rotational variations. Each liver volume is then converted to a triangulated mesh surface by using a marching cube algorithm [9]. Prior

to registration, the iterated closest point (ICP) algorithm (proposed by Besl and McKay [10]) was used to find the point correspondences. Following this, GPA is used to calculate the transformation parameters, and the result of GPA is used as the matrix **D** in SLRMD. Finally, the accuracy of the registration is improved by the transformation parameters obtained from the low-rank matrix **A**, and thus the effects of the local deformations are reduced.

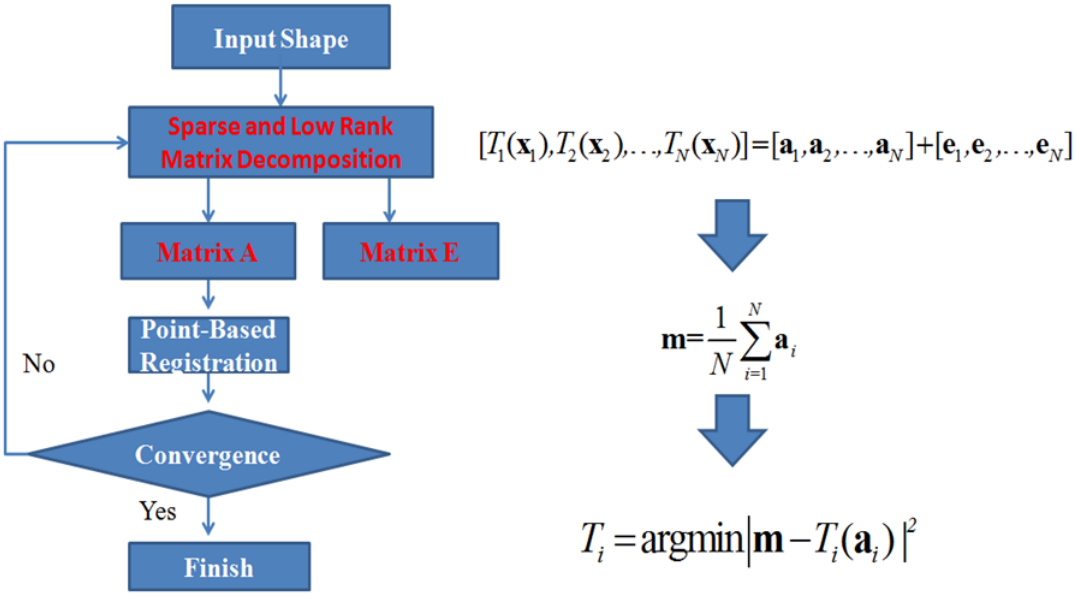

Figure 4.4: The flow chart of my proposed method for registration.

4.2.3 Experimental Results

Because it is difficult to evaluate the performance of a modelwith real data without having established a ground truth, the proposed method was evaluated using 3D simulation data. Different levels of local deformation degree (LDD), which are similar to noise, were added to a liver shape, and the LDD was then evaluated by determining the signal-to-noise ratio (SNR). Figure 4.5 shows the original shape and one artificial shape. The shape was then rotated by using the simulated transformation matrix. Two evaluation criteria were used; these are introduced below.

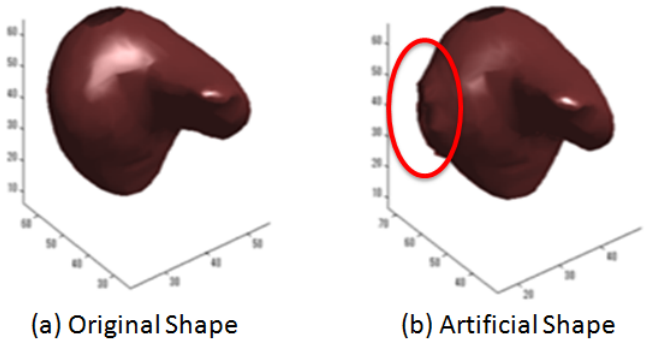

Figure 4.5: The original shape and one artificial shape in the experiment.

For the ensemble of the simulated liver shapes, I used the conventional GPA and my proposed strategy to estimate the rotation transformation matrices. I used Rodrigues' rotation formula [11], which can be used to transform all three basis vectors in order to compute the rotation matrix from an axis-angle representation, and this can then be used to evaluate the registration. With the real and estimated rotation matrices, the Rodrigues' transformation matrix can be obtained using Eq. 4.14:

$$T = R_{real} \times R^{T}_{estimate} \tag{4.14}$$

Where R_{real} is the real rotation matrix, $R_{estimate}$ is the estimated rotation matrix. Given T, a measure metric (an angle θ) between the real and estimated rotation matrixes can achieved as the following:

$$\theta = \arccos(^{(trace(T)-1)}/_{2}) \tag{4.15}$$

When θ is smaller, the result is better. Figure 4.6(a) shows the distribution of Rodrigues' angles used to evaluate the registration with the conventional method and the proposed method when the parameter λ in Eq.4.1 was fixed. Red indicates the conventional method, and blue indicates the

proposed method. The horizontal axis indicates the LDD value, and the vertical axis indicates the value of . It can be seen that the proposed method is more stable for local deformations, and in both methods, a smaller LDD results in better registration results.

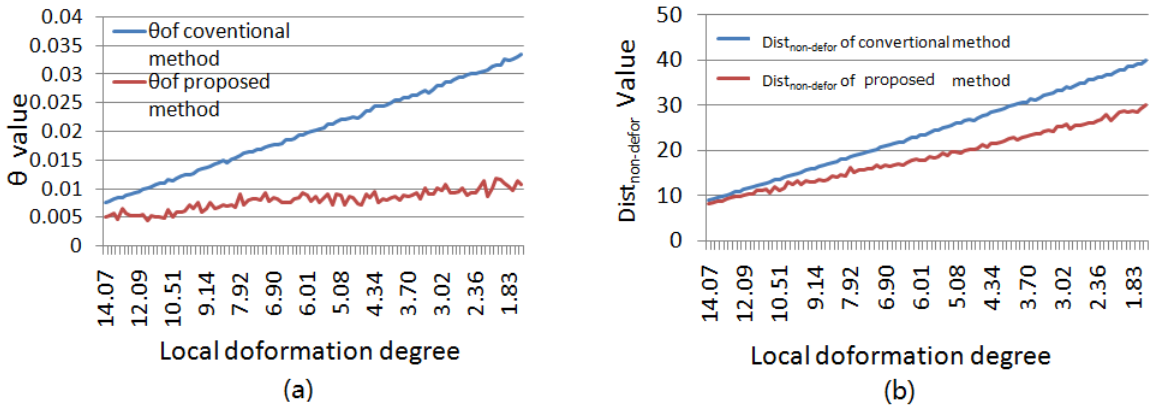

Figure 4.6: The relationship between LDD and value of evaluation criterions when the parameter λ is fixed.

Furthermore, using the available information for the LDD of the simulated liver shapes, I proposed using the coordinates to calculate the distance between the nondeformed landmarks roots (denoted as '$Dist_{non-defor}$') in order to verify the registration performance, as shown in Eq.4.16, where N is the number of nondeformed points, are the coordinates of the ground truth, and (x_i^o, y_i^o, z_i^o) are the coordinates of the estimated shape. When this distance is smaller, the result is better. The (x_i^r, y_i^r, z_i^r) is shown in Figure 4.6(b) for the conventional and the proposed strategies. The definitions used in Figure 4.6(b) are the same as those used in Figure 4.6(a), except that the vertical axis indicates the value of $Dist_{non-defor}$. It is obvious that the registration performance of my proposed method is better than that of the conventional method.

$$\sum_{i=1}^{N} \sqrt{(x_i^o - x_i^r)^2 + (y_i^o - y_i^r)^2 + (z_i^o - z_i^r)^2} \tag{4.16}$$

Figure 4.7 shows the relationship between the parameter λ and the evaluation criteria when the

LDD is fixed; Figure 4.7(a) shows this for θ, and Figure 4.7(b) shows this for $Dist_{non-defor}$. It can be seen that the best results are obtained when the value of λ is near 0.03 or 0.04 and that as LDD decreases, the registration improves.

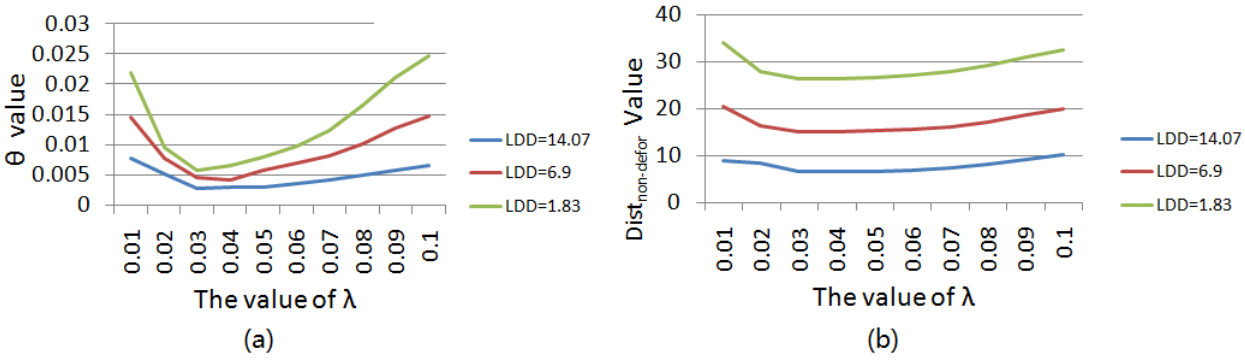

Figure 4.7: The relationship between parameter λ and value of evaluation criterions when LDD is fixed.

4.2.4 Discussion

In this section, I proposed a robust GPA that is obtained by using sparse and low-rank matrix decomposition. The proposed method can remove the effects of noise and local deformations. The low-rank matrix (the matrix of similar global structures) was used to improve the registration results. The proposed method was evaluated with a simulated database and two evaluation criteria. Results of experiments with the simulated data showed that my proposed strategy can achieve registration performances that are better than those of the conventional method.

4.3 Cirrhosis Liver Diagnosis based on SLRMD

Chronic liver disease is a major worldwide health problem, and cirrhosis of the liver is a typical chronic disease that can be generally divided into early, middle, and late stages. The appropriate treatment for cirrhosis depends strongly on the accurate estimation of the stage of the disease. Since late-stage cirrhosis is often associated with the occurrence of hepatocellular carcinoma, early detection is essential

in order to investigate the cause and slow the progression of cirrhosis [12].

Many researchers have tried to find ways to accurately diagnose cirrhosis. Some researchers have used various types of imaging to make the diagnosis. For example, Ogawa et al.[13] proposed combining ultrasonographic images with neural network analysis, and Lee et al.[14] introduced a kernel-based classifier for automatic diagnosis of liver diseases from CT images. There are also feature extraction methods, which can be categorized into two groups: texture-based methods and shape-based methods. One of the most commonly used texture-based methods combines the gray level co-occurrence matrix (GLCM), which is based on features from CT images, with neural network classifiers. The research group of Gifu University [15][16] and Kayaalti et al. [17] used texture features as input and classified normal/cirrhotic livers by using, respectively, an artificial neural network (ANN) and a support vector machine (SVM). Both groups obtained promising results.

However, there are limits on the clinical applications of analysis of texture. Besides tissue fibrosis, cirrhosis has another notable characteristic: shape changes occur in the liver during the clinical course of chronic liver diseases [19]. Typical CT volumes are shown in Figure 4.8. The values for normal livers are shown on the left, and those for cirrhotic livers are shown on the right. It can been seen that cirrhosis will cause hypertrophy of the left lobe and atrophy of the right lobe. Although the morphologic changes in the liver can be detected by computed tomography (CT), visual assessment is subjective and is limited in its ability to detect small changes. In my previous work [19], I proposed a statistical shape model (SSM) that used principal component analysis (PCA) to analyze the morphology of the liver and then selected suitable features to be used to diagnose cirrhosis. Machine learning techniques such as SVM and support vector regression (SVR) are used for classification or for estimation of the stage. However, the PCA-based SSM is a global analysis of shape method, and it is difficult to determine to what extent local deformations are due to cirrhosis. In addition, both

SVM- and SVR-based classification are not easy to use and understand for doctors. Thus a simple measure is more useful for doctors.

In this work, I proposed a method based on sparse and low-rank matrix decomposition, that quantitatively analyzes the local shape changes in order to obtain an accurate and practical diagnosis of cirrhosis. The basic idea behind using this decomposition method for local analysis of shape is that the shape of the liver can also be decomposed into two parts: one is a low-rank shape, which can be considered to be that part of the shape that is similar to a normal liver; the other is a sparse error term, which represents the local deformation. My proposed method can be used for the quantitative analysis of local shape changes, and it improves the accuracy of classification, compared to the previous SSM-based global analysis of shape strategy. Furthermore, due to the large deformations caused by cirrhosis, the norm of $\mathbf{E}$ should be larger for abnormal livers than for normal ones. Thus the norm of $\mathbf{E}$ can be used as a simple measure for the classification of livers as normal or abnormal. The proposed method was evaluated using a database that includes 30 normal livers and 30 abnormal livers. The results with the proposed method were better than those of the state-of-the-art SSM-based methods.

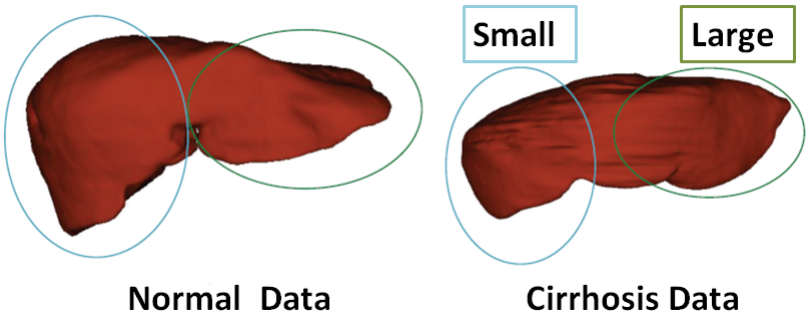

Figure 4.8: Typical shapes of liver from data: (a) normal and (b) cirrhosis.

4.3.1 Related Work

As I mentioned in the previous section, cirrhosis causes significant local shape changes in the liver. In my previous work, I proposed the construction of an SSM for analysis of shape of the liver, based on PCA and using selected suitable modes as features for the diagnosis of cirrhosis. A flowchart for combining SSM with mode selection is shown in Figure 4.9.

The preprocessing parts were similar as those of registration. Figure 4.10 is the schematic diagram of segmentation and normalization. After preprocessing, the matrix of all the samples is $\mathbf{D} = [\mathbf{d}_1,\mathbf{d}_2,\ldots,\mathbf{d}_M]$, and M is the number of samples. Each column vector (shape) is represented as

$$\mathbf{d}_i = (x_{i1}, x_{i2}, \ldots, x_{iN}, y_{i1}, y_{i2}, \ldots, y_{iN}, z_{i1}, z_{i2}, \ldots, z_{iN}) \tag{4.17}$$

where N is the number of surface points. In our previous work [19], SSM which was mentioned in section 2.2 was built for making the diagnosis. In order to obtain features that can be used to discriminate between cirrhosis and healthy livers and thus lead to an accurate diagnosis, in reference[19], the authors proposed to combine two methods for selecting the modes. One of these methods is an eigenvector-based method that returns the shape variation that has the largest contribution. The other is a correlation-based method that finds the most distinctive modes.

However, there are existing several problems here. Firstly, PCA treats the error part as dense and i.i.d. Gaussian. While for cirrhosis, the deformation may be sparse and local. Secondly, it is difficult to clearly explain the constructed models in terms of which one manifests the global variations due to the differences between subjects, and which one expresses the local deformations due to the progression of cirrhosis. Even with the proposed method for model selection, it is unclear if the selected models reflect only the deformations due to cirrhosis. Finally, both SVM- and SVR-based classification are not easy to use and understand for doctors. Thus a simple measure is more useful for doctors.

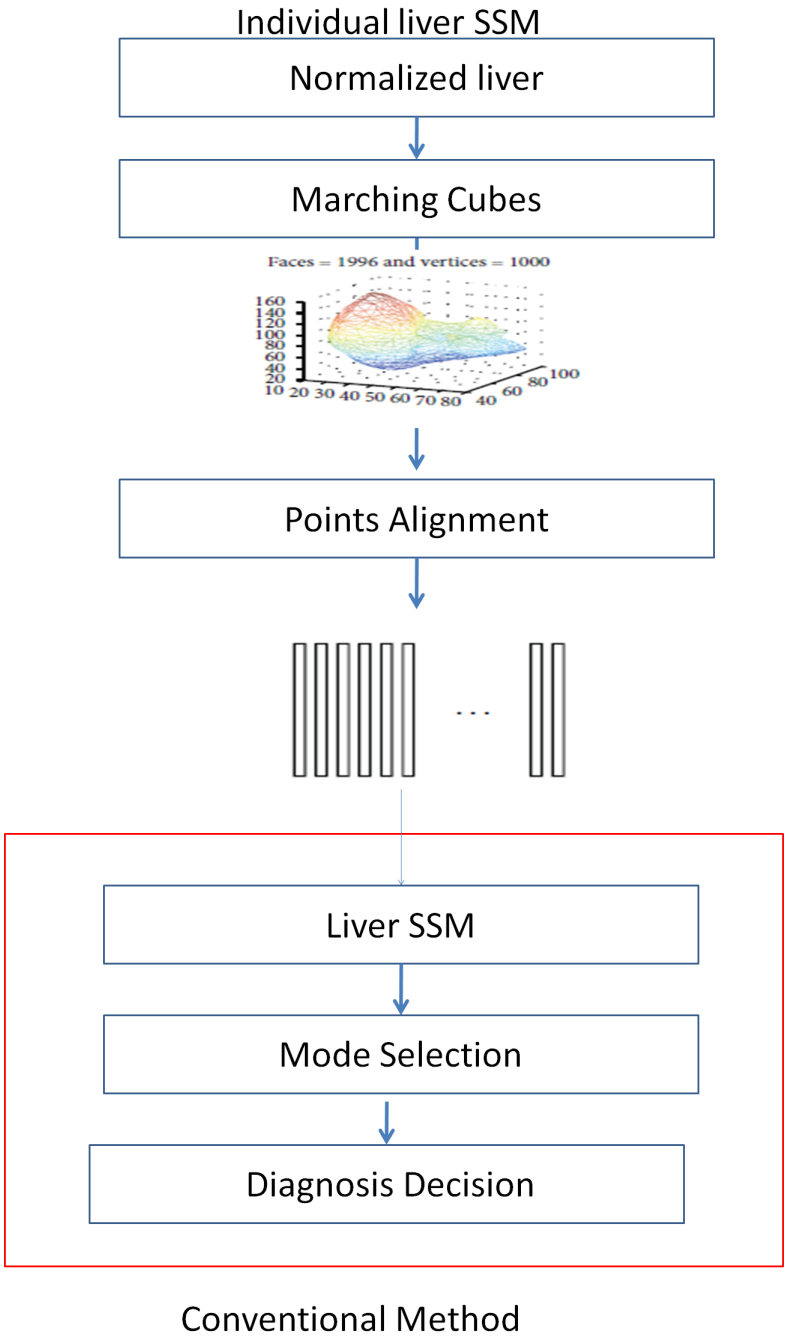

Figure 4.9: Flowchart for combining SSM with mode selection.

4.3.2 Proposed Method

In this section, I will introduce my proposed strategy for the diagnosis of cirrhosis. I assumed that the shape ensemble of the liver has a low-rank global structure with sparse local deformations. The

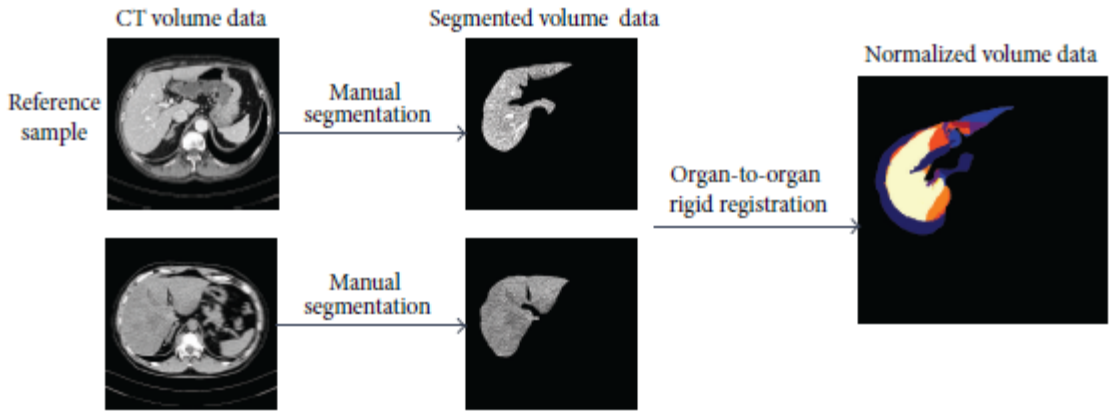

Figure 4.10: Schematic diagram of segmentation and normalization.

schematic for sparse and low-rank matrix decomposition for the analysis of local variations in liver shape is shown in Figure 4.11. In different livers, the local deformations will be distinct, which means that the sparsity will be different for each sample in the sparse matrix **E**. The sparsities of normal livers should be smaller than those of abnormal livers. The deviations of landmarks in the sparse matrix can be considered to be the offsets from the standard model. For instance, if each sample has N landmarks, the offset of one landmark is calculated by Eq.4.18:

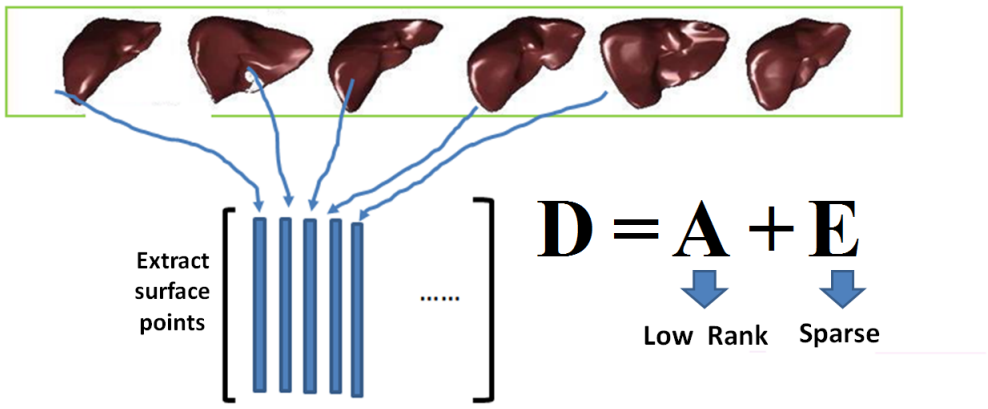

Figure 4.11: Schematic for sparse and low-rank matrix decomposition. **D** is the input data, which, in this paper, are the coordinates of the points on the surface of the shape; **A** and **E** are the low-rank matrix and the sparse matrix, respectively.

$$e_{ij}^{offset} = \sqrt{E_x^{ij^2} + E_y^{ij^2} + E_z^{ij^2}} \tag{4.18}$$

where $E_x^{ij}, E_y^{ij}, E_z^{ij}$ represent the coordinates of the j^{th} landmark of the i^{th} sample in the sparse matrix $\mathbf{E}$. Thus for each sample, I can get an offset vector $\mathbf{e}_i^{offset}$. Each element of the vector is e_{ij}^{offset}. The values of the offsets of abnormal livers should be larger than those for normal ones, and thus I can use the norm to make the diagnosis. Based on the differences between offsets, I can use a threshold value to classify the liver into one of two categories by using the L1-norm or the L2-norm of $\mathbf{E}$. The L1-norm and L2-norm for each sample are calculated by Eq.4.19 and Eq.4.20, respectively:

$$\|\mathbf{e}_i\|_1 = \sum_{j=1}^{N} \left(\left|E_x^{ij}\right| + \left|E_y^{ij}\right| + \left|E_z^{ij}\right|\right) \tag{4.19}$$

and

$$\|\mathbf{e}_i\|_2 = \sqrt{\sum_{j=1}^{N} \left(\left|E_x^{ij}\right|^2 + \left|E_y^{ij}\right|^2 + \left|E_z^{ij}\right|^2\right)} \tag{4.20}$$

where $\mathbf{e}_i$ is a vector that represents the i^{th} sample in the sparse matrix $\mathbf{E}$. Because I respectively use the L0-norm, L1-norm and the L2-norm of $\mathbf{E}$, and $\mathbf{E}$ is obtained from the sparse and low-rank matrix decomposition, I call my proposed method the L0SLRMD (based on the L0-norm), L1SLRMD (based on the L1-norm) and the L2SLRMD (based on the L2-norm). Figure 4.12 shows the flowchart of the proposed method. In the proposed method, for each new test sample, first calculate the new sparse matrix $\mathbf{E}$ with the training samples, and then use a threshold to classify them. If the number of training samples is sufficient, the norm of $\mathbf{E}$ will not change greatly with the addition of more training samples.

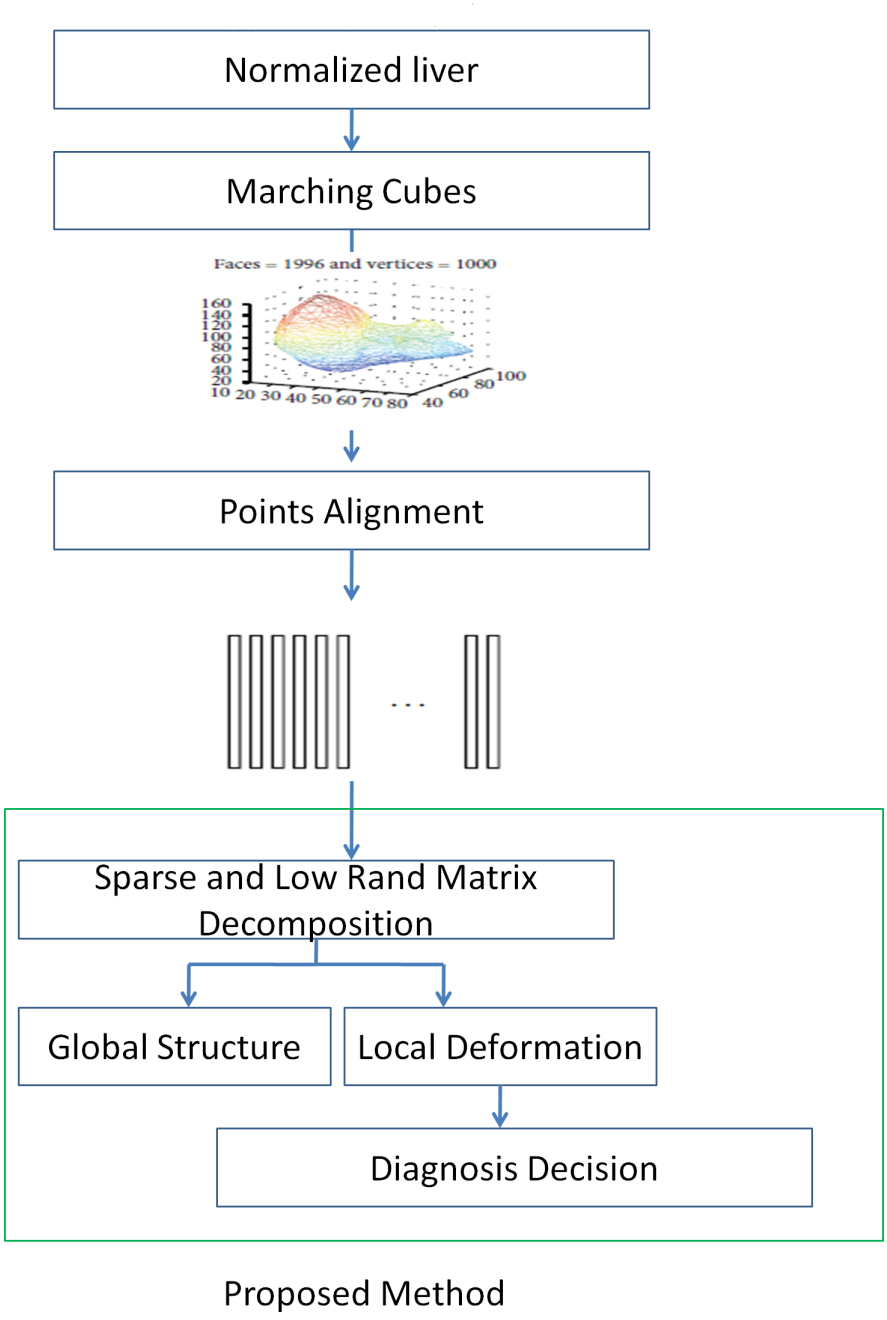

Figure 4.12: Flowchart of the proposed method.

4.3.3 Experimental results

In order to validate that the SLRMD can determine the local deformation, I firstly used simulation data for which random local deformation had been added to the initial liver shape(ground truth)

which were shown in Figure 4.13. 1000 surface points were extracted by marching cube method, and randomly chose 5% positions adding local deformation. The first row of Figure 4.13 is the ground truth shapes which are represented by red. The yellow shapes in the second row are the simulation shapes. The blue ones are the global structures after sparse and low rank matrix decomposition. I can see that after decomposition, the deformations are removed and the ground truth structure is recovered. The last row of Figure 4.13 is the hot map of offsets which were calculated from matrix **E**. In the hot map, the positive values and negative values mean raised parts and concave parts which were calculated by comparing matrix **A** and matrix **D**. It illustrates that the matrix **E** is sparse.

I also used 30 normal livers and 30 livers affected by cirrhosis, for a total of 60 livers. The size of each liver is $256 \times 256 \times 79$, and the spacing of each shape is $0.63 \times 0.63 \times 2.5(mm)$. From each liver, 1000 surface points were extracted. Meanwhile in this paper, I set hyper-parameter $\lambda = 1/\sqrt{N}$, where N is the dimension of sample. In reference[6], Cands et al proved this hyper-parameter is the best one for this problem.. And in my experiment, when I adopted λ as the previous equation, the rank of matrix **A** is 8 which was shown in Figure 4.14.

Meanwhile, Figure 4.15(a) showed the absolute value of matrix **E**. It illustrated that the normal data is more sparse than abnormal data. However, matrix **E** cannot directly reflect the magnitude of deformation, thus an offset matrix was calculated as shown in Figure 4.15(b). Each element of offset matrix was calculated as Eq.4.21:

$$e_{ij}^{offset} = \sqrt{E_x^{ij^2} + E_y^{ij^2} + E_z^{ij^2}} \tag{4.21}$$

where $E_x^{ij}, E_y^{ij}, E_z^{ij}$ represent the values of the j^{th} landmark of the i^{th} sample in the sparse matrix **E**. Figure 4.15 illustrates that the non-sparsity and offset of normal data are both smaller than those of abnormal ones. For quantitative analysis, non-sparsity and average value of offset which was

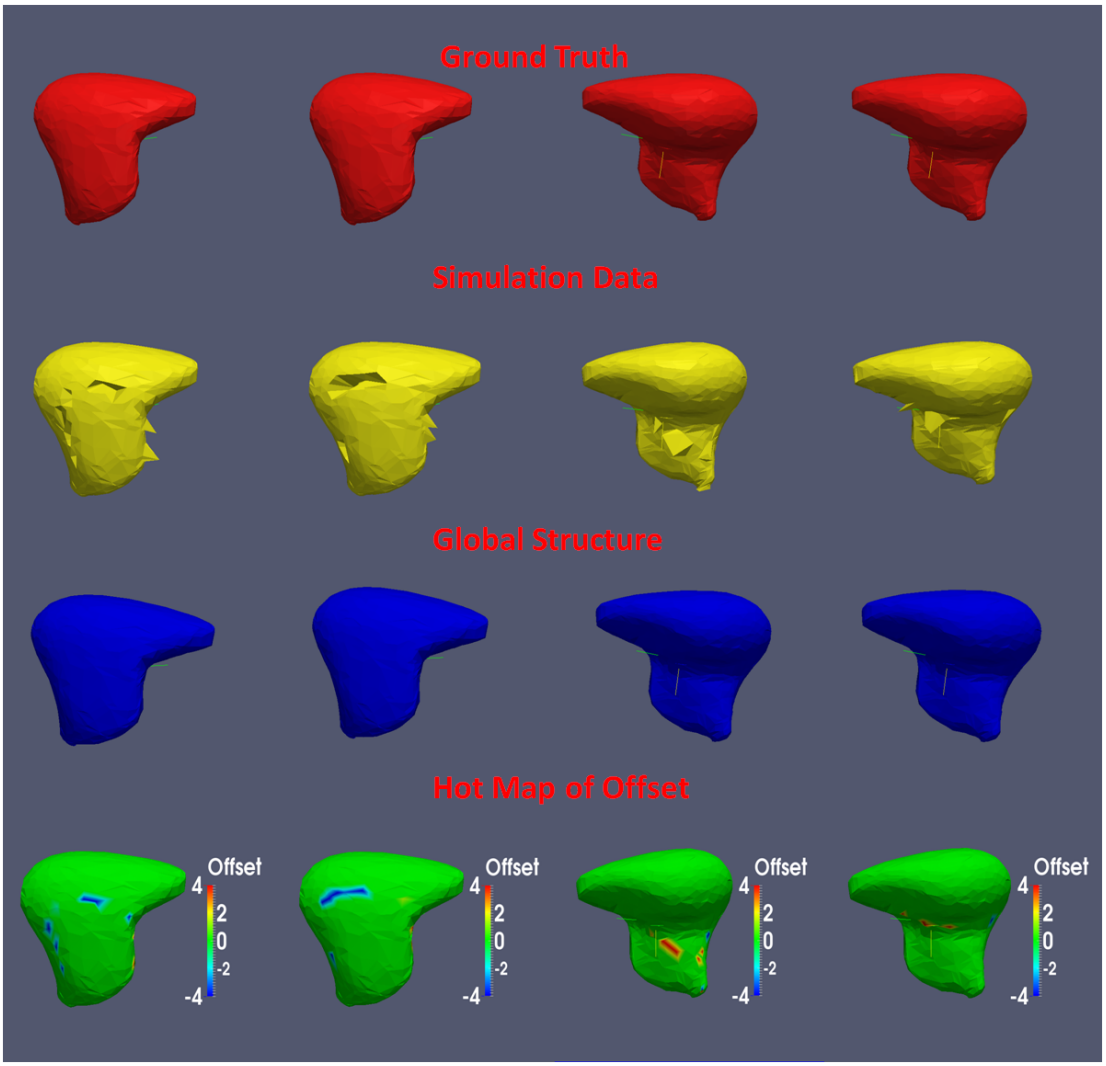

Figure 4.13: Simulation Data. Each column belongs to the same sample. The ground truth shapes are represented by red. The yellow shapes in the second row are the simulation shapes. The blue ones are the global structures after sparse and low rank matrix decomposition. The last row of is the hot map of offsets which were calculated from matrix **E**.

calculated as Eq.4.22 were given in Table 4.1.

$$average\_offset = \frac{1}{N_k \times M} \sum_{i=1}^{N_k} \sum_{j=1}^{M} e_{ij}^{offset} \tag{4.22}$$

where N_k is the number of normal samples($k = 1$) or abnormal samples($k = 2$), M is the the number of surface points, in this paper, $M = 1000$. From Table 4.1, I can see that the non-sparsity of normal data is 14.6%, however that of abnormal data is nearly 30%. Furthermore, average offset

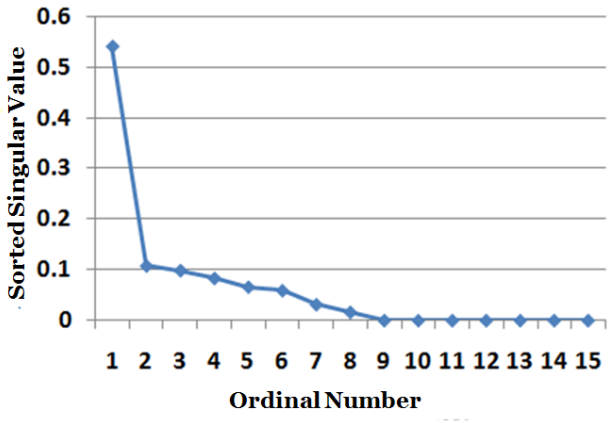

Figure 4.14: The distribution of singular values of matrix **A**.

of abnormal data was more than three times of that of normal data. And Std. is the Abbreviation of standard deviations.

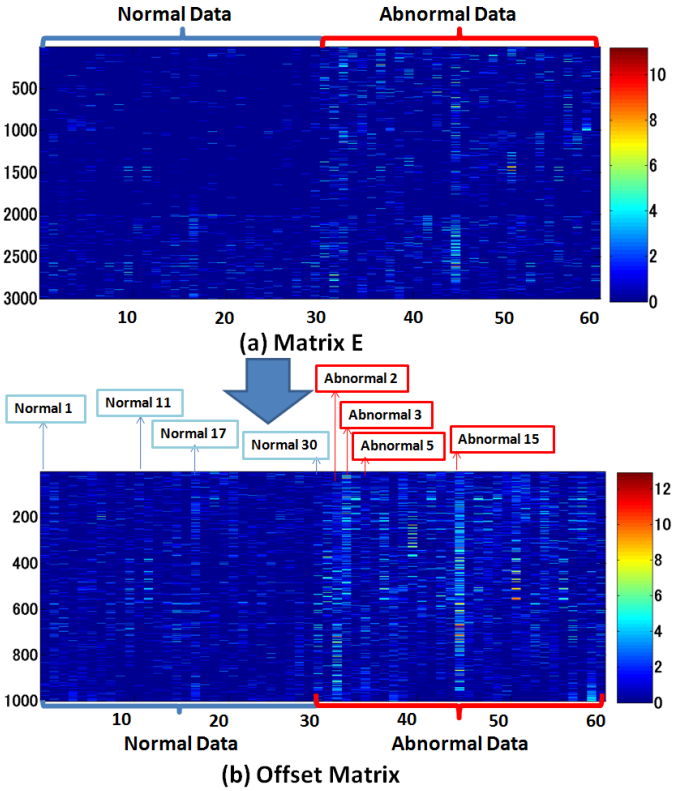

Figure 4.15: (a) is the Matrix **E** and (b) is the offset matrix.

Table 4.1: The non-sparsity which is the percentage of non-zero elements in the vector or matrix and the average offset and standard deviations (Std.) of each category.

	non-sparsity	average offset	Std.
Normal Data	14.6%	0.52	0.53
Abnormal Data	29.5%	1.78	1.4

In Figure 4.15 some samples are different from other samples in the same category, such as normal data 17 and 30, abnormal data 15. Figure 4.16 and Figure 4.17 showed some normal data and abnormal data including the samples mentioned above. The yellow shapes in the top row are the original shapes. The second row is the global structure of each sample represented by red. As shown in Figure 4.16, in spite of data 17 and 30 are normal data, they have larger deformation than other normal data, which can be considered as a shape variation of the normal liver. It should be noted such shape variations is rare (only 2 cases among 30 cases). Though such normal data will be classified as abnormal cases (false positive), I can reduce the number of such false positive data by adding texture information (it will be my future work). Meanwhile, Figure 4.17 gives the visualizations of four abnormal data, where the data 2, 5, 3 from columns 1-3 manifest the local deformations (large magnitude offset in local parts) as the clinic explanations of cirrhosis. However, data 15 is already in the late stage of cirrhosis, and gives very large deformation which leads to high-abnormal measure.

As shown in Table 4.1, the non-sparsity and average offset of normal data are both smaller than those of abnormal ones, thus I can use the norm of matrix $\mathbf{E}$ for classification. Figure 4.158(a) and Figure 4.18(b) show the plots and histograms of different norm for the sparse matrix $\mathbf{E}$, respectively. From Figure 4.18, it illustrated that I can easily classify two categories by using a simple threshold. For instance, when the value of threshold was set as 500 for L1SLRMD, the false positive is nearly 0.07 and true positive is nearly 0.97. With changing the threshold, I can get different false positive and true positive to plot ROC curve shown in Figure 4.19. Because the diagnosis accuracy of abnormal samples is more important in clinical applications, the abnormal data is considered as positive samples

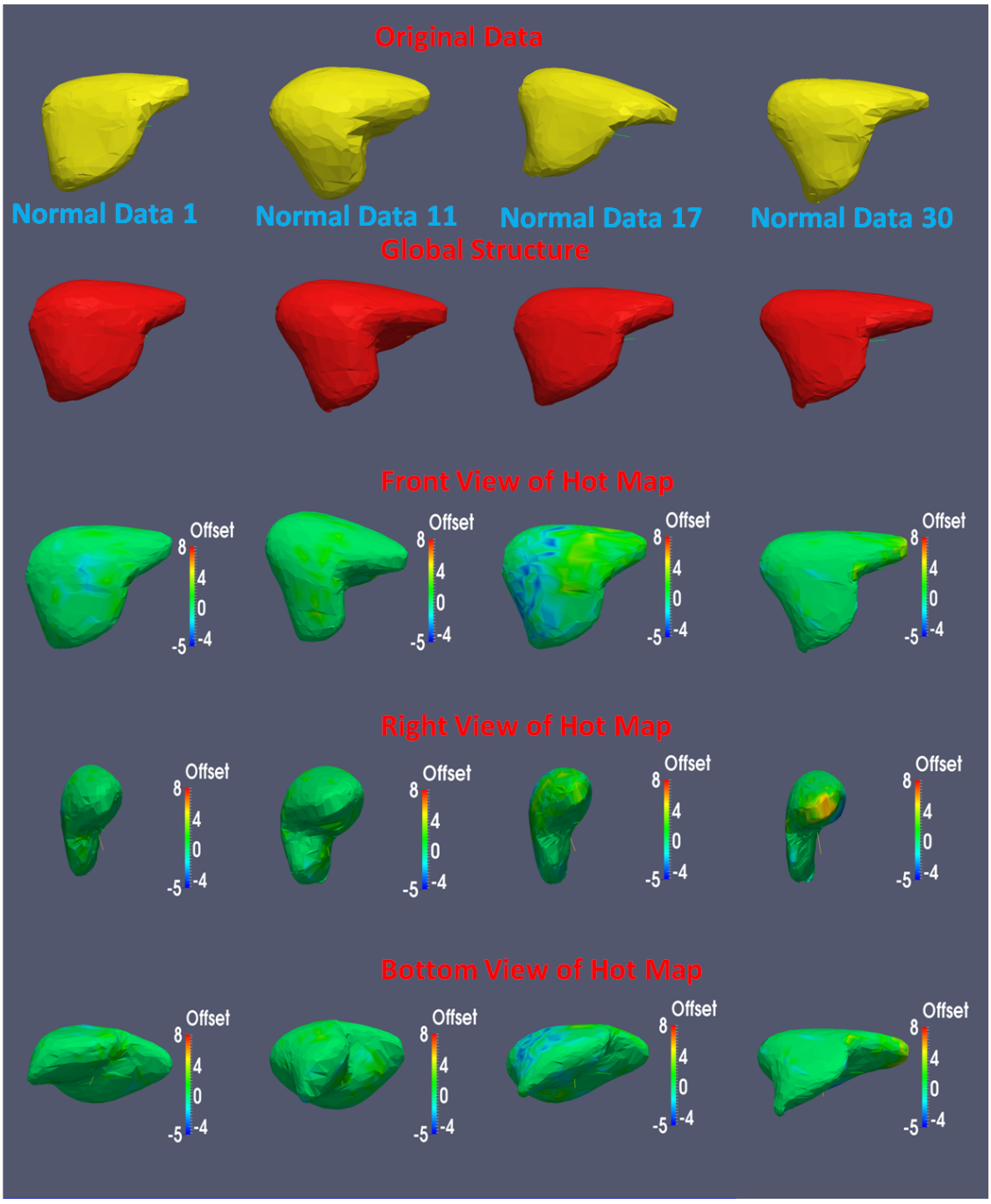

Figure 4.16: Normal Data. Each column belongs to the same sample. The top row is original shapes which are represented by yellow, and the red represents the global structure(matrix $\mathbf{A}$). The last three rows are the hot map of offsets from different view direction: front view, right view and bottom view, respectively.

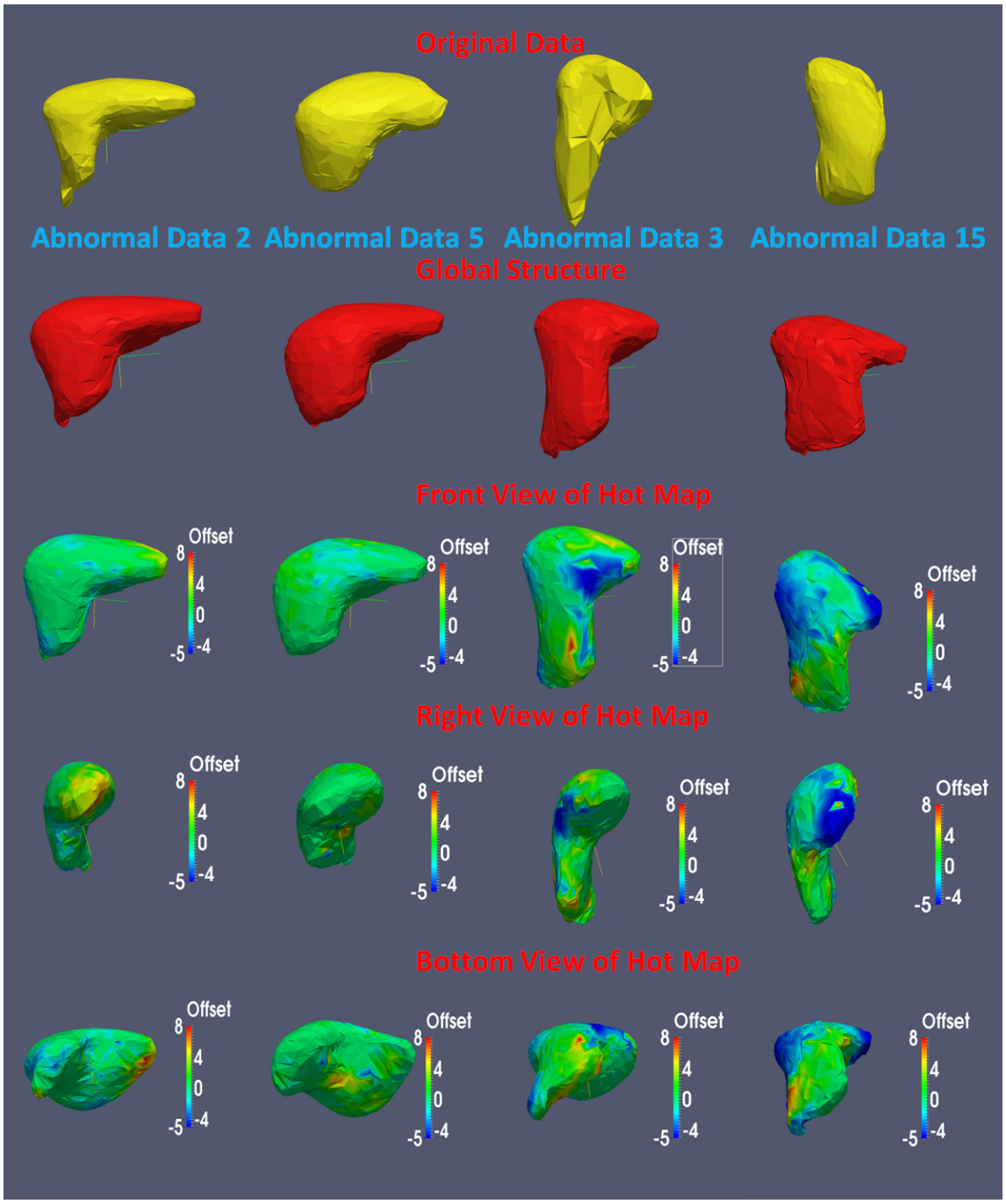

Figure 4.17: Abnormal Data. Each column belongs to the same sample. The top row is original shapes which are represented by yellow, and the red represents the global structure(matrix $\mathbf{A}$). The last three rows are the hot map of offsets from different view direction: front view, right view and bottom view, respectively.

in this paper.

In order to show the advantage of my proposed method, I compare my method with the conventional method which used SVM or Adaboost as a classifier, and tenfold cross validation method was adopted. While for the proposed method, it doesn't need cross-validation, because it needs to decompose the training samples and test samples together. Thus the decomposition results will be same, regardless which data are used for test. I chose the first 13 eigenvectors, linear kernel was adopted for SVM and 4 weak learners were selected for Adaboost. The ROC curve of these two methods were also shown in Figure 4.19. It illustrated that when the true positive got 100%, false positive of proposed method is the smallest. In this paper, the ROC curve was fitted by curve fitting method proposed by C.E.Metz [20].

Meanwhile, I can get the highest recognition rate of overall data from ROC curve. The highest recognition rate of different methods are shown in Table 4.2. I can see that the performance of the proposed method is better than those of the SSM-based methods. The best recognition rate was 0.95, which was attained by using my proposed strategy. Furthermore, I also gave the area under the curve(AUC) of ROC in Table 4.2. The value of AUC is larger, the performance is better. From Table 4.2, it showed that AUC of the proposed method is better than those of SSM-based methods, which means the performance of proposed method is better. The result of L0SLRMD is worse than those of L1SLRMD and L2SLRMD, because L0SLRMD only considers the sparsity of $\mathbf{E}$, while deformation degree is also very important. Meanwhile we repeated tenfold cross validation six times, each method got an AUC vector which was used to do t-test for statistically comparing with each method in Table 4.3. It illustrates that the performances of L1SLRMD and L2SLRMD are same with each other, and they are better than other methods.

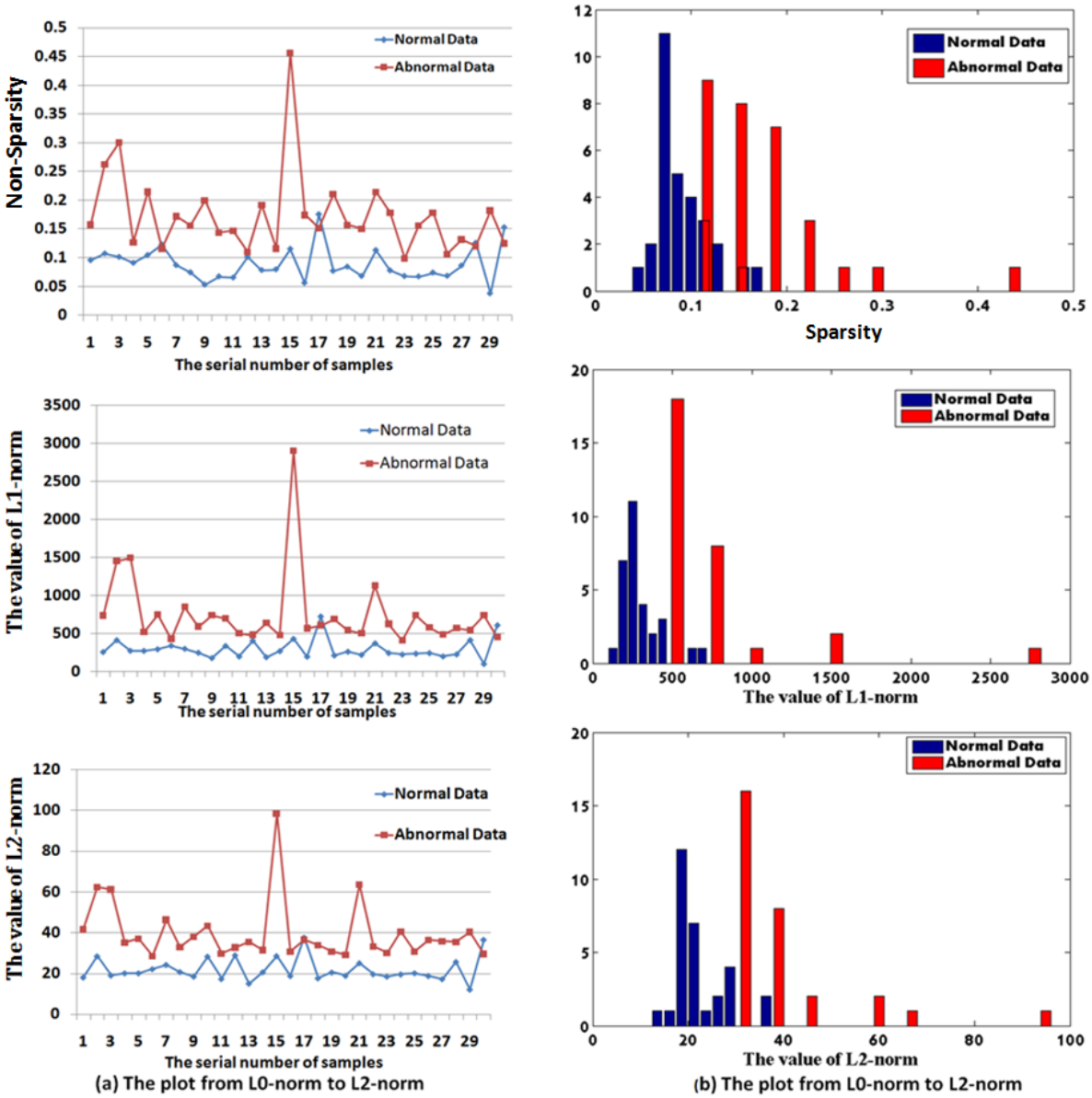

Figure 4.18: The plot and histograms from the L0-norm to L2-norm for the sparse matrix **E**. I used the percentage of non-zero elements(non-sparsity) to replace L0-norm for intuitive display. The left column shows the plots, and the right column shows histograms.

Table 4.2: The highest recognition rate of and area under the curve(AUC) of different methods.

	SSM+SVM	SSM+Adaboost	L0SLRMD	L1SLRMD	L2SLRMD
Recognition Rate	0.87	0.83	0.87	**0.95**	**0.95**
AUC	0.86	0.81	0.88	**0.91**	**0.91**

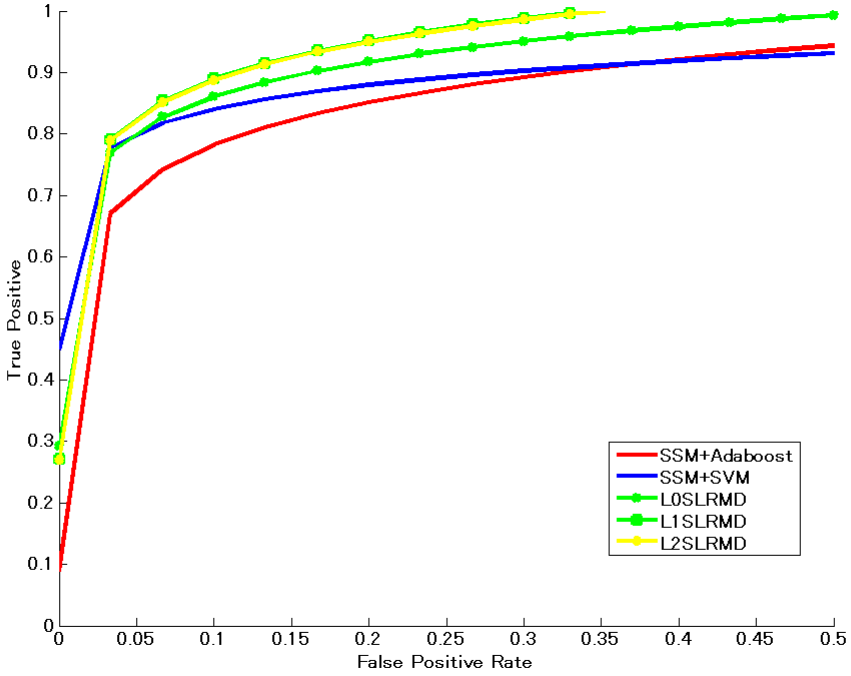

Figure 4.19: The ROC curve of different methods.

Table 4.3: t-test results of different methods.

	L0SLRMD	L1SLRMD	L2SLRMD	SSM+SVM	SSM+Adaboost
L0SLRMD	1	0	0	2.9e-4	0.21
L1SLRMD	0	1	1	2.2e-5	0.028
L2SLRMD	0	1	1	2.2e-5	0.028
SSM+SVM	2.9e-4	2.2e-5	2.2e-5	1	0.37
SSM+Adaboost	0.21	0.028	0.028	0.37	1

4.3.4 Discussion

In this section, I have proposed a robust method for medical diagnosis that uses images and is based on sparse and low-rank matrix decomposition. It is well known that livers from different subjects have a similar overall structure, indicating that the liver shape ensemble should be of low rank. However, cirrhosis can lead to local deformations, and these changes can be considered sparse with respect to the whole liver. Therefore, in this study, I proposed applying sparse and low-rank matrix decomposition in order to separate the local deformation (sparse error matrix $\mathbf{E}$) from the global structure (low-rank

matrix **A**), using a given liver shape as input **D**. **D** is the matrix of landmark coordinates, and it was initialized by using rigid registration. The sparse matrix **E** is then used to make the diagnosis. In general, normal livers have smaller local deformations than do abnormal livers; this means that the sparse matrix **E** of a normal liver has a smaller norm. Therefore, I have proposed a method that is based on a threshold classifier for the norm of **E**, in order to differentiate normal and abnormal livers. The proposed method was evaluated using a database of liver image information and was compared with various SSM-based methods. The experimental results indicated that the performance of the proposed method was better than those of the SSM-based methods.

4.4 Incremental SLRMD

In Section 4.2, SLRMD was introduced. Though many methods have been proposed to solve SLRMD, all of them share the problem of large data and the need to repeat calculations when new samples are added. Thus, none are convenient for real applications. In this section, I will introduce an incremental SLRMD that uses an alternating greedy algorithm for L0-norm regularization. This method can solve the problem of large data, and when new samples are added, it can obtain the new subspace from the old one. Before introducing the proposed method, I will discuss some related work.

4.4.1 Incremental Singular Value Decomposition

Singular value decomposition (SVD) is a factorization of a real or complex matrix, it provides a bilinear factoring of a data matrix **D**:

$$\mathbf{U}_{p\times r} diag(\mathbf{S}_{r\times r})\mathbf{V}^T_{r\times q} \overset{SVD_r}{\leftarrow} \mathbf{D}_{p\times q},\ r \leq \min(p,q) \tag{4.23}$$

where **U** and **V** are unitary orthogonal matrices whose columns give a linear basis for **D**'s columns and rows, respectively. For low-rank phenomena, $r \ll \min(p,q)$, implying a parsimonious explanation

of the data.

Then assumed that an existing rank-r matrix as in Eq.4.23. When given a new matrix whose columns contain additional multivariate measurements. Let $\mathbf{L} \doteq \mathbf{U} \backslash \mathbf{C} = \mathbf{U}^T\mathbf{C}$ be the projection of C onto the orthogonal basis $\mathbf{U}$, also known as its eigen-coding. Let $\mathbf{H} \doteq (\mathbf{I} - \mathbf{U}\mathbf{U}^T)\mathbf{C} = \mathbf{C} - \mathbf{U}\mathrm{L}$ to be the component of $\mathbf{C}$ orthogonal to the subspace spanned by $\mathbf{U}$. ($\mathbf{I}$ is the identity matrix.) The rank of matrix $\mathbf{U}$ is r,$r \ll \min(p, q)$, thus $(\mathbf{I} - \mathbf{U}\mathbf{U}^T)$ does not equal zero. Finally, let $\mathbf{J}$ be an orthogonal basis of $\mathbf{H}$ and let $\mathbf{K} \doteq \mathbf{J} \backslash \mathbf{H} = \mathbf{J}^T\mathbf{H}$ be the projection of $\mathbf{C}$ onto the subspace orthogonal to $\mathbf{U}$. For example, $\mathbf{J}\mathrm{K} \overset{\mathrm{QR}}{\leftarrow} \mathbf{H}$ could be a QR-decomposition of $\mathbf{H}$ [21]. Consider the following identity:

$$\begin{aligned}
[\mathbf{U}\,\mathrm{J}] &= \begin{bmatrix} diag(\mathbf{S}) & \mathbf{L} \\ 0 & \mathbf{K} \end{bmatrix} \begin{bmatrix} \mathbf{V} & 0 \\ 0 & \mathbf{I} \end{bmatrix}^T \\
&= [\mathbf{U}(\mathbf{I} - \mathrm{U}\mathbf{U}^T)\mathbf{C}/\mathbf{K}] \begin{bmatrix} diag(\mathbf{S}) & \mathbf{U}^T\mathbf{C} \\ 0 & \mathbf{K} \end{bmatrix} \begin{bmatrix} \mathbf{V} & 0 \\ 0 & \mathbf{I} \end{bmatrix}^T \\
&= [\mathbf{U} diag(\mathbf{S})\mathbf{V}^T \;\; \mathbf{C}] = [\mathbf{D} \;\; \mathbf{C}]
\end{aligned} \tag{4.24}$$

Like an SVD, the left and right matrices in the product are unitary and orthogonal. The middle matrix, which denote as $\mathbf{Q}$, is diagonal. To update the SVD $\mathbf{Q}$ must be diagonalize. Let

$$\mathbf{U}' diag(\mathbf{S}) {\mathbf{V}'}^T \overset{SVD}{\leftarrow} \mathbf{Q} \tag{4.25}$$

and

$$\mathbf{U} \leftarrow [\mathbf{U}\,\mathbf{J}]\mathbf{U}';\; \mathrm{S} \leftarrow \mathbf{S}';\; \mathbf{V} \leftarrow \begin{bmatrix} \mathbf{V} & 0 \\ 0 & \mathbf{I} \end{bmatrix} \mathrm{V}' \tag{4.26}$$

Especially when $\mathbf{c}$ =$\mathbf{C}$ is a single column vector, vector $\mathbf{k}$ will be $\mathbf{k} = \mathbf{K} = \left\|\mathbf{c} - \mathbf{U}\mathbf{U}^T\mathbf{c}\right\|$ and vector $\mathbf{j}$ will be $\mathbf{j} = \mathbf{J} = (\mathbf{c} - \mathbf{U}\mathbf{U}^T\mathbf{c})/\mathbf{k}$, respectively. In reference [22] mentioned that the SVD

is usually computed by a batch $O(pq^2 + p^2q + q^3)$ time, while the incremental method can decrease the time as $O(pqr^2)$, and the advantage in-memory storage requirements are reduced from $O(pq)$ to $O(r(p+q+r))$.

4.4.2 Alternating Greedy Algorithm for L0-norm Regularization

L0-norm Regularization:

Derived from the original problem shown in Eq.4.2, the optimization over a sparse error matrix $\mathbf{E}$ becomes the following:

$$\min_{\mathbf{E}} \|\mathbf{M} - \mathbf{E}\|_2^2 + \lambda \|\mathbf{E}\|_0 \tag{4.27}$$

where $\mathbf{M} = \mathbf{D} - \mathbf{A}$ is the reconstruction error. In addition, define $vec(\mathbf{E}) \in \mathrm{R}^{mn \times 1}$ as the vector form of the matrix $\mathbf{E}$, and then the L0-norm regularized problem of Eq. 4.27 is equivalent to:

$$\min_{\mathbf{E}} \|vec(\mathbf{M}) - vec(\mathbf{E})\|_2^2 + \lambda \|vec(\mathbf{E})\|_0 \tag{4.28}$$

As mentioned above, this problem can be solved directly by the greedy pursuit algorithm, iterative thresholding, or by relaxing it to the L1-norm as a convex surrogate. To solve this problem, the authors in [23] developed a specifically designed greedy algorithm to solve Eq. 4.28 efficiently; this is equivalent to the following form:

$$\min_{E} \|vec(\mathbf{E})\|_0, \; s.t. \|vec(\mathbf{M}) - vec(\mathbf{E})\|_2 \leq \varepsilon \tag{4.29}$$

Compared to the L1-norm surrogate, the L0-norm regularization tends to be sparser with fast greedy algorithms, although it lacks guarantees of stability [24].

Alternating Greedy Algorithm for L0-norm Regularization:

I note that when the matrix A is known, the cost function of SLRMD, Eq. 4.2, is equivalent to Eq. 4.27. Motivated by the greedy algorithms [24] for sparse representation, the greedy alternating optimization is shown in Figure 4.20.

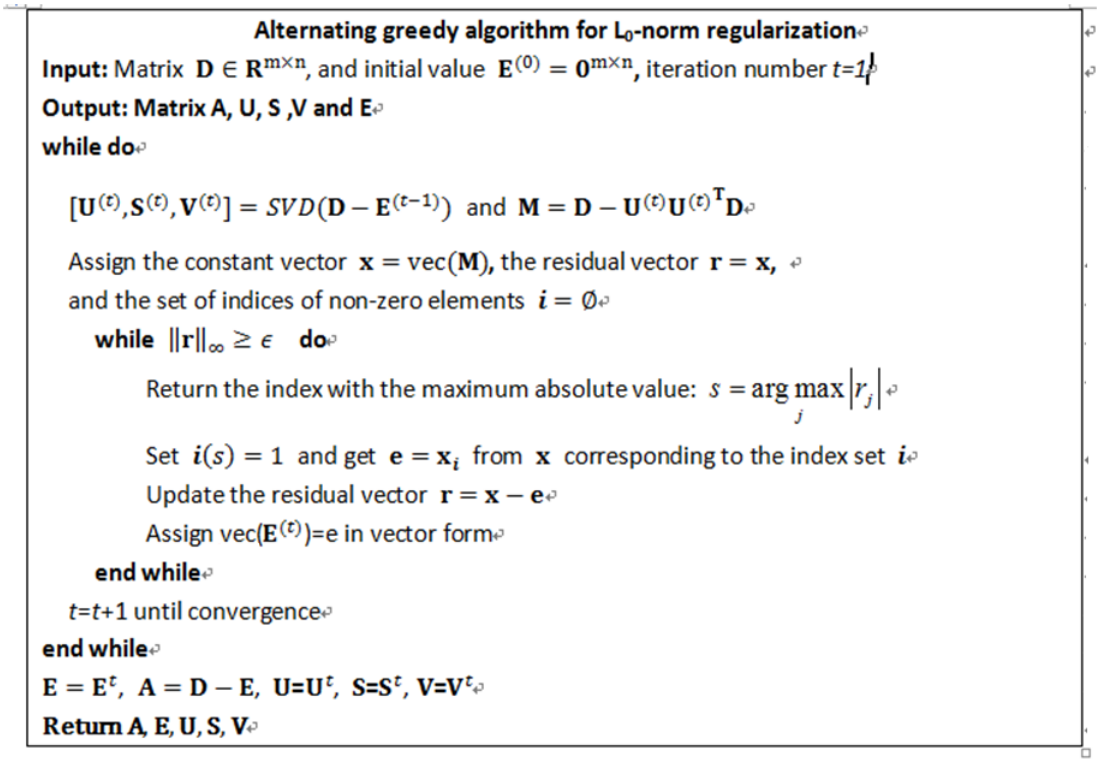

Figure 4.20: Alternating Greedy Algorithm for l0-norm Regularization.

4.4.3 Proposed Method and Experimental Results

In the previous section, I introduced a method to solve the SLRMD: the alternating greedy algorithm for L0-norm regularization. This method is also a batch processing method. If the size of database is large or when new data are added, it will have the same problem that was discussed above for PCA. Thus, I wished to find an incremental method. I noted that the first iteration in the alternating greedy algorithm for L0-norm regularization is an SVD, and the matrix **E** is calculated from the reconstruction error. Thus, I use an incremental SVD to replace the SVD in the iteration. As a result, when new data are received, it can be used to adjust the subspace and to obtain the new reconstruction error,

which can then be used to calculate the new sparse matrix E. Figure 4.21 shows the flowchart of the proposed method.

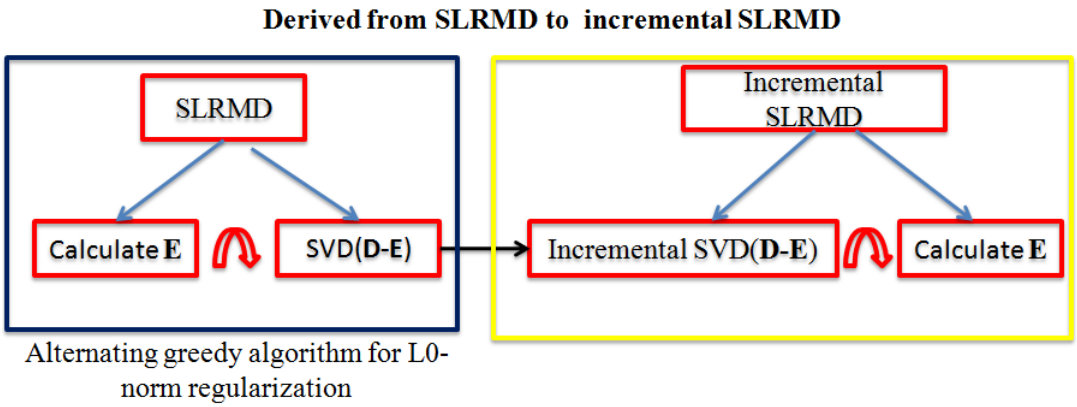

Figure 4.21: Incremental Sparse and Low Rank Matrix Decomposition.

To evaluate the proposed method for diagnosis of liver cirrhosis, I used the database mentioned in Section 4.4.4. I used the alternative greedy algorithm for L0-norm regularization as the batch method to recalculate the sparse matrix **E**. The L2-norm was used for classification. The classification rate was 93%, which is close to the result of the previous experiment. For the proposed method, the leave-one-out method was used: one data point was used as the incremental data point, and the others were used to obtain the original matrices **A** and **E**. I calculated the correlation value between the matrices **E** and **A** calculated using the batch method and those calculated using the proposed method; this is shown in Figures 4.22 and 4.23, respectively.

From these figures, it can be seen that most matrices E have a correlation value of nearly 0.95 and most matrices A have a correlation value of nearly 0.99; this means that the proposed method can recover most of the original matrices E and A. The final classification rate is 0.9. Although the final result of the proposed method is 3% less than that of the original batch method, the size of the database was small; so if missing samples had been classified, this means that the classification rate would decrease to 1%. If the size of dataset were increased, the results of the proposed method

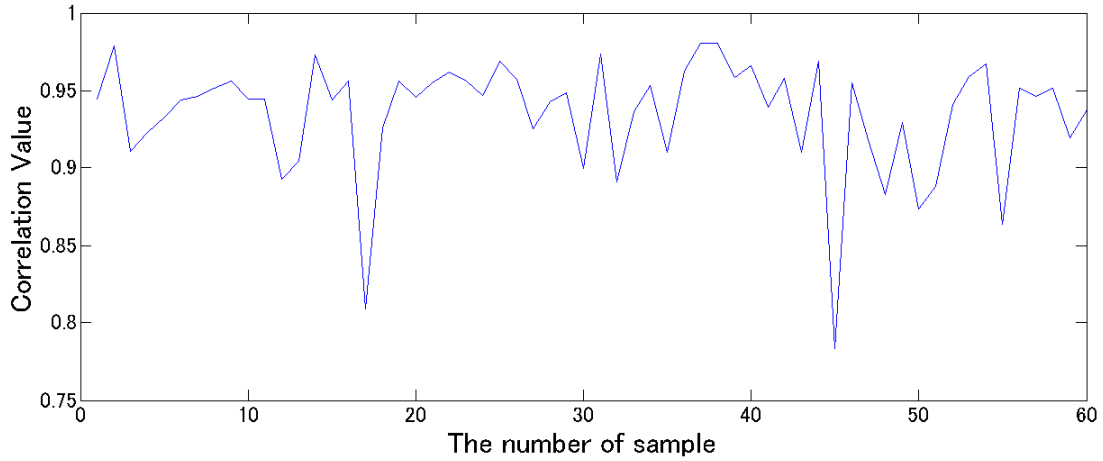

Figure 4.22: The correlation value of matrix E.

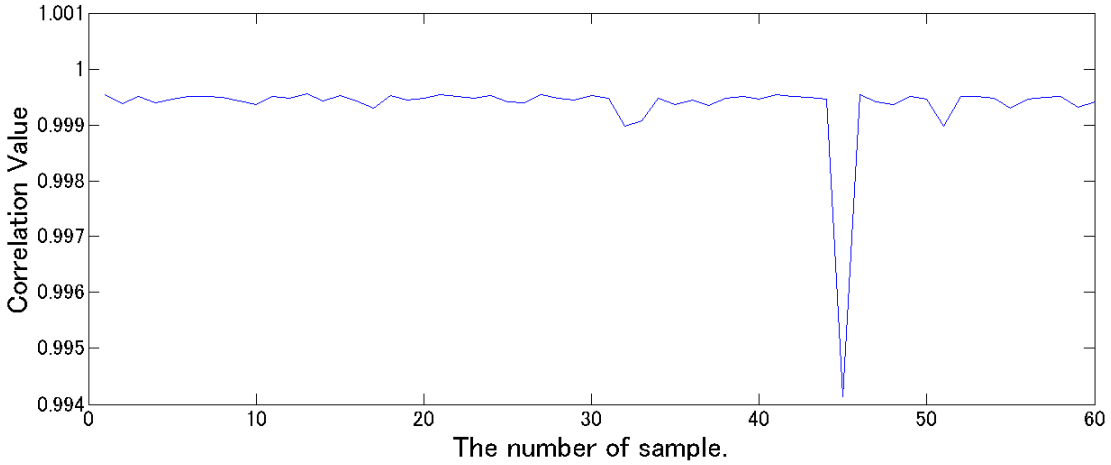

Figure 4.23: The correlation value of matrix A.

would be closer to that of the original method. In Figure 4.24 showed the computation time of batch method and incremental method. Blue represents the batch method and red represents the incremental method. The average computing time of proposed method is 2 second less than that of the batch method which is 40 second. Furthermore, the computing time of batch method will become very large with the size of data increasing, while computing time of proposed method is constant.

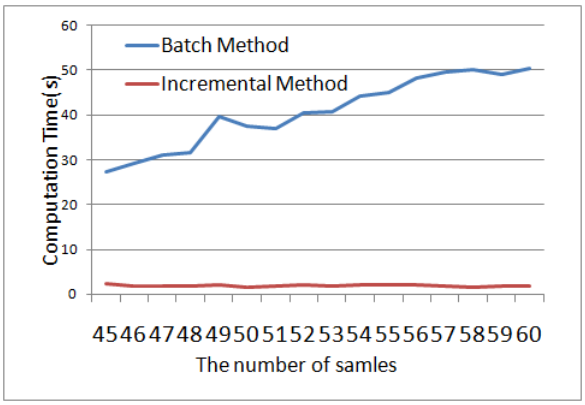

Figure 4.24: Computation time of batch method and incremental method.

4.4.4 Discussion

In this section, I introduced an incremental method based on SVD to avoid the need to recalculate the sparse and low-rank matrix decomposition when adding new samples. It is not practical to recalculate the matrix for cirrhosis liver diagnosis each time a new patient is evaluated, since this would be time consuming and would require a large amount of data to be stored, due to the large amount of data in medical images. In an experiment, I used the same data as were used for the experiment in Section 4.2.4. The proposed incremental method was able to recover the results that were calculated by the batch method (alternative greedy algorithm for L0-norm regularization). The computation time of the proposed method was less than that of the batch method. In this version, all of the parameters were determined manually; as an area of future work, I will explore how they might be set automatically for each dataset.

Bibliography

[1] J. Wright, A. Ganesh, S. Rao et al., Robust principal component analysis: Exact recovery of corrupted low-rank matrices via convex optimization, *Advances in neural information processing systems*, 2080-2088, 2009.

[2] Z. Shen, K.C. Toh, S. Yun, An accelerated proximal gradient algorithm for frame-based image restoration via the balanced approach, *SIAM Journal on Imaging Sciences*, 4(2):573-596, 2011.

[3] Z. Lin, M. Chen, L. Wu, and Y. Ma, The Augmented Lagrange Multiplier Method for Exact Recovery of Corrupted Low-Rank Matrices, *UIUC Technical Report UILU-ENG-09-2215*, 2009.

[4] X. Yuan, J. Yang, Sparse and low-rank matrix decomposition via alternating direction methods, 2009.

[5] Z. Lin, M. Chen, L. Wu, and Y. Ma ,The Augmented Lagrange Multiplier Method for Exact Recovery of Corrupted Low-Rank Matrices,*UIUC Technical Report UILU-ENG-09-2215*,2009.

[6] E. J. Cand¨¨s, X. Li, Y. Ma, et al, Robust principal component analysis?, *Journal of the ACM (JACM)*, 58(3): 11, 2011.

[7] GRUEN, W. Armin, M. Devrim AKCA, Generalized procrustes analysis and its applications in photogrammetry, *Swiss Federal Institute of Technology*, 1, 2003.

[8] J. Cho, M. Lee, C.H. Choi et al., EM-GPA: Generalized Procrustes analysis with hidden variables for 3D shape modeling[J], *Computer Vision and Image Understanding*, 117(11):1549-1559, 2013.

[9] W.E. Lorensen, H.E. Cline, Marching cubes: a high resolution 3D surface construction algorithm, *Computer Graphics*, 21(4):163-169, 1987.

[10] P.J. Besl, N.D. McKay, Method for registration of 3-D shapes, *IEEE Trans. Patt. Anal. Mach. Intell.* 14(2):239-256, 1992.

[11] J.E. Mebius, Derivation of the Euler-Rodrigues formula for three-dimensional rotations from the general formula for four-dimensional rotations, *arXiv preprint math/0701759*, 2007.

[12] N.H. Afdhal, D. Nunes, Evaluation of liver fibrosis: a concise review, *American Journal of Gastroenterology*, 99(6):1160-1174, 2004.

[13] E. Ogawa, M. Fukushiina, K. Kubota, N. Hisa, Computer-aided DiagnosticSystem for Diffuse Liver Diseases with Ultrasonographyby Neural Networks, *IEEE Transactions on NUCLEAR SCIENCE*, 45(6):3069-3074, 1998.

[14] C.C. Lee, S.H. Chen, H.M. Tsai et al., Discrimination of liver diseases from CT images based on Gabor filters, *19th IEEE International Symposium on Computer-Based Medical Systems*, 203-206, 2006.

[15] X. Zhang, H. Fujita, M. Kanematsu et al., Improving the classification of cirrhotic liver by using texture features,*in Proceedings of the 27th Annual International Conference of the Engineering in Medicine and Biology Society (IEEE-EMBS 05)*, 867-870, September, 2005.

[16] H. Kato, M. Kanematsu, X. Zhang et al., Computer-aided diagnosis of hepatic fibrosis: preliminary evaluation of mri texture analysis using the finite difference method and an artificial neural network, *American Journal of Roentgenology*, 189(1):117-122, 2007.

[17] O. Kayaalt, B.H. Aksebzeci, M.H. Asyal, O.I. Karahan et al., Texture analysis of liver cirrhosis, *in Proceedings of the 15th National Biomedical EngineeringMeeting (BIYOMUT 10)*, April, 2010.

[18] P.P. Anthony, K.G. Ishak, N.C. Nayak et al., The morphology of cirrhosis. Recommendations on definition, nomenclature, and classification by a working group sponsored by the World Health Organization[J], *Journal of clinical pathology*, 31(5):395-414, 1978.

[19] Y.W. Chen, J. Luo, C.H. Dong et al., Computer-Aided Diagnosis and Quantification of Cirrhotic Livers Based on Morphological Analysis and Machine Learning, *Computational and mathematical methods in medicine*, 2013.

[20] C.E. Metz, X. Pan, "Proper"binormal ROC curves: theory and maximum-likelihood estimation, *Journal of mathematical psychology*, 43(1):1-33, 1999.

[21] L.N. Trefethen, D. Bau, Numerical Linear Algebra, *SIAM* , 1997.

[22] M. Brand, Incremental singular value decomposition of uncertain data with missing values[M], *Computer Vision¡ªECCV, Springer Berlin Heidelberg*, 707-720, 2002.

[23] Y.P. Sun, X.M. Tao et al., Robust two-dimensional principal component analysis via alternating optimization, *IEEE International Conference on Image Processing (ICIP)*, 2013.

[24] D. Needell, J.A. Tropp, CoSaMP: Iterative signal recovery from incomplete and inaccurate samples[J], *Applied and Computational Harmonic Analysis*, 26(3):301-321, 2009.

Chapter 5

Conclusion

With the development of computer science, Computer-Aided diagnosis (CAD) have been incorporated into our lives. The basic idea of CAD is to extract useful features (shape and texture features) from medical images and then use machine learning methods to give or generate a second opinion for doctors' final diagnosis. In this thesis, I proposed several methods based on statistical analysis of shape and texture for computer aided diagnosis. The contributions of the thesis are summarized as following.

Firstly, I described a statistical texture modeling method for medical volumes which is known as LTC which is an extension of GND-PCA. The medical volume such as the volume of the liver is represented by a linear combination of basis. Each basis are mutual independence and more discriminate than GND-PCA. In my experiments, I compared both reconstructed results and classification results of LTC and GND-PCA. As for reconstruction results, the performance of LTC was superior to that of GND-PCA. Additionally, in the classification part, I firstly chose the distinctive basis through the correlation between category labels and the coefficients of basis of LTC. And then the selected basis were used for classification. The classification accuracy was significantly improved by using selected distinctive basis.

Secondly, I proposed a robust GPA by using sparse and low-rank matrix decomposition. Image

registration was a challenging work due to the noise or local deformation. Thus I used sparse and low-rank matrix decomposition to remove the noise or local deformation which can be formulated as sparse error, and then used low-rank matrix (similar global structures) to achieve more exact registration result. The registration performance was evaluated by simulation data. Experimental results on simulated data showed that my proposed strategy can achieve promising registration performances compared with the conventional method. In the future, I will use my method for real data.

Thirdly, I also proposed a robust method for medical diagnosis based on sparse and low-rank matrix decomposition. It is well known that livers from different subjects have a similar overall structure, indicating that the liver shape ensemble should be of low rank. However, cirrhosis can lead to local deformations, and these changes can be considered sparse with respect to the whole liver. Therefore, in this study, I applied SLRMD to separate the input shape information $\mathbf{D}$ into the noise or local deformation part (sparse matrix $\mathbf{E}$) and the global similar structure (low rank matrix $\mathbf{A}$). Then the sparse matrix $\mathbf{E}$ was used to make the diagnosis. In general, normal livers have smaller local deformations than those of abnormal livers; that means the sparse matrix $\mathbf{E}$ of a normal liver has a smaller norm. Therefore, I proposed a method that was based on a threshold classifier for the norm of $\mathbf{E}$, in order to distinctive normal and abnormal livers. The proposed method was evaluated by using a liver database and was compared with various SSM-based methods. The experimental results indicated that the performance of the proposed method was better than those of the SSM-based methods.

Finally, I introduced an incremental sparse and low rank matrix decomposition based on ISVD. Conventional sparse and low rank matrix decomposition is not practically for cirrhosis liver diagnosis due to recalculating when given a new test sample(patient). Meanwhile it is time-consuming and need to cost large memory to save the data because of the large size of medical image. From the

experimental results, it illustrated that the proposed incremental method can recover the result which was calculated from batch method. Meanwhile the computation time of proposed method is also less than that of batch method. In the future, I will consider the issue about parameters in the algorithm. In this version, all the parameters were given manually, I want to set the parameters automatically based on the database.

Publication Lists

Peer-reviewed Journal Papers

1. **J.P. Deng**, X. Qiao, Y.W. Chen, Statistical Texture Modeling for Medical Volume Using Linear Tensor Coding, *Computational and Mathematical Methods in Medicine*, vol.2013, Article ID 630902, 10 pages, 2013. Doi:10.1155/2013/630902.

2. **J.P. Deng**, X.H. Han, Y. W. Chen et al., Sparse and Low-Rank Matrix Decomposition for Local Morphological Analysis to Diagnose Cirrhosis, *IEICE TRANSACTIONS on Information and Systems*, vol.E97-D, no.12, Dec., 2014 (in press).

Peer-reviewed International Conference Papers

1. G.F. Duan, H.C. Wang, Z.Y. Liu, **J.P. Deng** and Y.W. Chen. K-CPD: Learning of Overcomplete Dictionaries for Tensor Sparse Coding, *International Conference of Pattern Recognition (ICPR)*, pp.493-496, Tsukuba , Japan, November, 2012.

2. **J.P. Deng**, R. Xu, X.H Han, Y.W. Chen, Generalized N-Dimensional PCA for Compact Representation of Medical Volumes and Effective Mode Selection by Adaboost, *The 2013 Pacific-Rim Conference on Multimedia(PCM)*, vol.8294, pp.629-636, Nanjing, China, December, 2013.

3. **J.P. Deng**, Y,W. Chen, X.J. Feng, H.C. Lu, Gender Recognition based on Ultra Pixel-Pattern-Based Texture Feature, *20th Korea-Japan Joint Workshop on Frontiers of Computer Vision*, Okinawa, Japan, February, 2014.

4. **J.P. Deng**, X.H. Han, G. Xu, Y.W. Chen, Sparse and Low-Rank Decomposition for Robust Medical Image Registration, *International Journal Computer Assisted Radiology and Surgery*,

vol.9(Supplement 1), pp.295-296, Fukuoka, Japan, June, 2014.

5. **J.P. Deng**, X.H. Han, Y.W. Chen, Sparse and Low Rank Matrix Decomposition Based Local Morphological Analysis for Diagnosis of Cirrhosis Livers, *22nd International Conference on Pattern Recognition*, pp.3363-3368, Stockholm, Sweden, August, 2014.

Conference Papers without review

1. **J.P. Deng**, X.H. Han, G, Xu, Y.W. Chen, Sparse and Low-Rank Decomposition for Robust Medical Image Registration, *the 9th Joint Workshop on Machine Perception and Robotics*, Kyoto, Japan, October, 2013.

2. G.F. Duan, **J.P. Deng**, Y.W. Chen, An Overcomplete Dictionary Learning Algorithm for Tensor Sparse Representation, *Pattern Recognition and Media Understanding(PRMU)*, pp.1-6, Nagana, Japan, May, 2012.

3. Y.W. Chen, **J.P. Deng**, X. Qiao, et al., Multilinear Subspace Learning Methods for Computational *Anatomical Modeling: Progress Overview FY 2012, Proceedings of the Fourth International Symposium on the Project "Computational Anatomy"* , pp.105-107, Osaka, Japan, February, 2013.

4. **J.P. Deng**, X.H. Han, Y.W. Chen. Sparse and Low Rank Matrix Decomposition for Cirrhosis Diagnosis based Local Morphological Analysis, *IEICE Technical Report, MI*, vol. 114, no. 200, MI2014-41, pp.33-37, Tokyo, Japan, September, 2014.

5. Y.W. Chen, **J.P. Deng**, X.H. Han, T. Tateyama, Multilinear Subspace Learning Methods for Computational Anatomical Modeling: Progress Overview FY 2009-2013, *Proceedings of the Fifth*

International Symposium on the Project "Computational Anatomy" , pp.101-105, Tokyo, Japan, March, 2014.

Award

1. Best Scientific Paper Awards in International Conference on Pattern Recognition (ICPR2012), Nov.11-15, 2012, Japan.

2. Best Poster Award in the 9th Joint Workshop on Machine Perception and Robotics (Kyoto, Japan, 2013.10.31-11.1).

ACKNOWLEDGEMENT

I would like to express my gratitude to Professor Yen-Wei Chen, my supervisor at Ph.D course in Ritsumeikan University, for giving me valuable guidance, suggestions, educations and encouragement throughout my entire Ph.D studying. His constructive advice is essential for the successful and timely completion of this dissertation and has taught me insight on the workings of academic research in general.

I would also like to express my sincere thanks to the dissertation committee: Professor Satoshi Tanaka and Professor Gang Xu, for their constructive criticism and valuable suggestions and comments.

I am particularly grateful to Dr. Xianhua Han, Dr. Xu Rui, Dr. Guifang Duan, Dr. Tomoko Tateyama, Ms. Yuka Sato in Ritsumeikan University and Dr Xu Qiao in Shandong University for providing the helpful suggestions and valuable comments and helping me whenever being asked.

My warm thanks are due to all my colleagues in Intelligent Image Processing Lab in Ritsumeikan University, especially Ms. Chunhua Dong, Ms. Mei Uetani, Ms. Ayako Taniguchi, Mr. Hidetoshi Tanaka, Mr. Chen-lun Lin, Mr. Jian Wang, Mr. Haihang Qiu, Ms. Riko Kusumoto, Mr. Motoki Nakajima, Mr. Yusuke Nojima, Ms. Mayu Hakata, Mr. Yuu Konno, Ms. Misae Nakatsu, Ms. Kanae Hata, Mr. Yuto Kondo for giving me comfortable environment for study and stimulating discussion.

Finally, I thank my girlfriend, Yi Li, for giving me generous support and understanding in every part of my life, and would also like to extend my gratitude to my parents, Xiaobai Deng and Lihua Yin, for all of the long-time support they have given me, visible and invisible.

Junping Deng

September, 2014